SEMMELWEIS EGYETEM

DOKTORI ISKOLA

Ph.D. értekezések

2963.

GYARMATI GEORGINA

A folyadék- és elektrolitháztartás szabályozásának élet- és kórélettana – keringés és vérnyomásszabályozás
című program

Programvezető: Dr. Zsembery Ákos, egyetemi docens

Témavezető: Dr. Peti-Peterdi János, egyetemi tanár

NEW MECHANISMS OF MACULA DENSA CELLS IN RENAL PHYSIOLOGY, DISEASE AND THERAPY

PhD thesis

Georgina Gyarmati MD MPH

Doctoral School of Theoretical and Translational Medicine

Semmelweis University

Supervisor: Janos Peti-Peterdi MD PhD
Laszlo Rosivall MD DSc

Official reviewers: Andrea Fekete MD DSc
Jozsef Balla MD DSc

Complex Examination Committee:

Head: Miklos Kellermayer MD DSc

Members: Laszlo Smeller DSc
Hassan Charaf DSc

Budapest
2023

TABLE OF CONTENTS

LIST OF ABBREVIATIONS

AA	Afferent arteriole
ACEi	Angiotensin-converting enzyme inhibitors
AD	Alzheimer's disease
ADR	Adriamycin
ANOVA	Analysis of variance
AVP	Arginine vasopressin
cc4DP	Comparative-cell 4-dimension physiology
CCN1/Cyr61	Cellular communication network factor 1
Cdh5/VE-cadherin	Vascular endothelial cadherin
CGRP	Calcitonin gene-related peptide
CKD	Chronic kidney disease
Cox2	Cyclooxygenase 2
DMEM-F12	Dulbecco's Modified Eagle Medium F12
DT	Distal tubule
EA	Efferent arteriole
ECM	Extracellular matrix
eGFP	Enhanced green fluorescent protein
EGM	Extraglomerular mesangium
Erk1/2	Extracellular signal-regulated kinase 1/2
ESRD	End stage kidney disease
FDR	False discovery rate
Foxd1	Forkhead box d1
FSGS	Focal segmental glomerulosclerosis
GCaMP	Genetically encoded calcium indicator
GFB	Glomerular filtration barrier
GLP-1	Glucagon-like peptide-1
IA	Interlobular arteriole
IGM	Intraglomerular mesangium
IPA	Ingenuity Pathways Analysis
JG	Juxtaglomerular
JGA	Juxtaglomerular apparatus
LS	Low salt
mc4DP	Multi-cell 4-dimension physiology
MD	Macula densa
MPM	Multiphoton microscopy
mTmG	Membrane targeted tomato membrane targeted GFP
NaCl	Sodium chloride

NG2	Nerve/glial antigen 2
NGFR/p75NTR	Nerve growth factor receptor
NKCC2	Sodium Potassium Chloride Cotransporter 2
NO	Nitric oxide
Nos1/nNOS	Neuronal nitric oxide synthase
PAPPA2	Pregnancy-associated plasma protein 2
PGE2	Prostaglandin E2
PT	Proximal tubule
RAS	Renin-angiotensin system
Ren1d	Renin 1d
ROI	Region of interest
Romk	Renal outer medullary potassium channel
sc4DP	Single-cell 4-dimension physiology
SEM	Standard error of the mean
SGLT2	Sodium-glucose cotransporter-2
sox2	Sex determining region Y-box 2
SYP	Synaptophysin
TAL	Thick ascending limb
TGF	Tubuloglomerular feedback
TH	Tyrosine hydroxylase

1. INTRODUCTION

Chronic kidney disease (CKD) is a condition in which the kidneys are damaged and cannot filter blood as well as healthy kidneys. As a result, excess fluid and waste from the blood remain in the body and may cause other health problems, such as cardiovascular disease and cognitive impairment (1). CKD is a devastating chronic illness and a rapidly growing disease worldwide. More than 10% of the general population worldwide is estimated to have CKD -- that is over 800 million individuals (2-5). The severe loss of normal kidney function (end stage renal disease, ESRD) affects about 100 million people across the world, requires high-cost renal replacement therapies (dialysis, transplantation) and is associated with even higher morbidity and mortality (6). The incidence and cost of CKD is similar in many parts of the world and is expected to grow even further due to increasing prevalence of diabetes, hypertension, and infection-induced acute kidney injury, the main risk factors and drivers of the development of CKD. Since CKD is a progressive disease, most people will ultimately require renal replacement, unless new and highly efficient therapies are developed that can stop or reverse kidney function decline. Presently, only non-specific therapies are available, including the current standard of care, renin-angiotensin system blockers. Even the newest drugs from recent successful clinical trials, SGLT2 inhibitors and GLP-1 agonist can only slow down CKD progression to end stage renal disease (7). Clearly, there continues to be an urgent and unmet medical need for specific, mechanism-based, and highly efficient CKD therapies for the treatment of millions of patients worldwide. The unmet medical need and inadequacy of current treatments have led to great interest in regenerative medicine and in the better understanding of regulatory mechanisms that can re-activate and guide resident stem/progenitor cells including mesenchymal and endothelial precursors that in turn effectively remodel the fibrotic renal parenchyma. Improved understanding of endogenous kidney tissue repair and identification of the key cellular and molecular targets are critically important for the development of specific, mechanism-based regenerative therapies that can achieve disease regression.

Physiological adaptation to maintain functional homeostasis is a known driver of physiological regeneration in multiple organisms and mammalian tissues (8). Physiological signals associated with either loss or gain of organ function, such as fasting for the nervous, endocrine and digestive systems (9, 10) and mechanical force for the

skeletal system (11) can trigger potent regenerative responses. Additional clues regarding endogenous regenerative mechanisms come from adaptive evolution. Conservation of body fluid and salt was a major driver of evolution that brought about the highly efficient and complex mammalian nephron compared to the primitive structure in fish (12). The loss of neo-nephrogenesis capacity in birds and mammals coincided with the appearance of a cell-based regeneration strategy and the differentiation of unique, specialized nephron cell types (12) including the macula densa.

Macula densa (MD) cells are understudied but chief cell type within the kidney and play key sensory and regulatory functions of intrarenal mechanisms that maintain body fluid and electrolyte homeostasis and blood pressure (13). MD is formed by a niche of about 25 individual cells localized in a strategically central position at the vascular pole entrance of the kidney filter (glomerulus) (Fig.1). MD cells are part of the juxtaglomerular (JG) apparatus (JGA), a key anatomical site within the kidney and exhibit distinct polarized morphology: the apical prominent primary cilia (14, 15) and large nucleus and densely packed secretory organelles at the basolateral surface (16). These unique

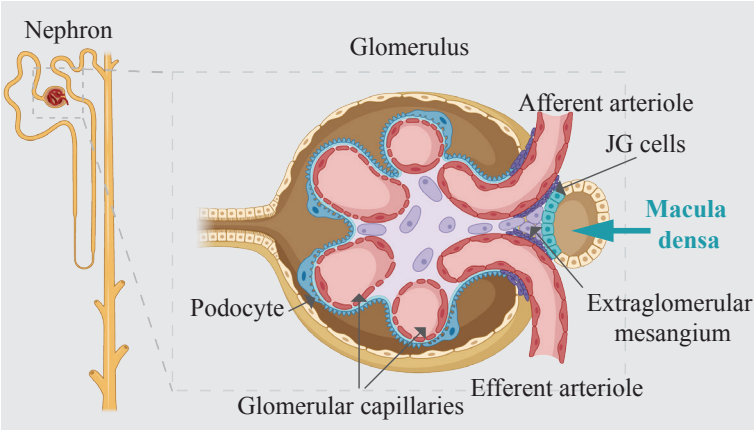

Figure 1: Schematic illustration of the nephron, the glomerulus, and the juxtaglomerular apparatus (JGA).

microanatomical features are critical in the traditional function of MD cells to provide key physiological control of basic kidney functions including glomerular filtration rate, renal blood flow and renin release (13, 17), but the true nature of these cells has been largely unknown due to their inaccessibility. According to the existing paradigm, MD cells can sense alterations in renal tubular fluid variables including NaCl content and metabolic intermediates, that via various intracellular signaling pathways trigger the synthesis and release of chemical mediators (13). The main molecular players of MD tubular salt sensing involve apical sodium chloride transport mechanisms, including the furosemide-sensitive Na^+-K^+-Cl^- cotransporter 2 (NKCC2) (13), and downstream intracellular signaling mechanisms: p38, extracellular regulated kinase ½ (ERK ½), cyclooxygenase 2 (COX2), and neuronal nitric

oxide synthase (NOS1), and the synthesis and release of prostaglandin E2 (PGE2) and nitric oxide (NO) (13, 18-22). These mediators then in turn act in a paracrine fashion on final effector cells, including renin producing cells to secrete renin, or contractile vascular smooth muscle cells of glomerular arterioles to regulate vascular resistance and organ blood flow via tubuloglomerular feedback (TGF) (13, 17). Recent clinical trials reporting the renoprotective effects of SGLT2 treatment in diabetic nephropathy placed the macula densa back into the spotlight. The current understanding is that hyperglycemia in diabetic patients drastically lowers the concentration of sodium in the tubular fluid resulting in the constant blockade of TGF hence hyperfiltration, increased glomerular pressure, and glomerular injury. SGLT2 inhibitors inhibit the sodium-glucose cotransporters in the proximal tubule, which in turn leads to increased glucose and sodium concentrations in the tubular fluid and restored TGF and MD function (23).

The central and peripheral nervous system senses and integrates information about the inner state of the body through the process of interoception, which is essential for maintaining mental and physical health. Interoception involves a variety of neural and non-neural cells and processes in several internal organs by which an organism senses, interprets, integrates, and regulates signals from within itself (24). There are well-established bidirectional interoceptive communications between the brain and peripheral neural networks in several organs throughout the body including the heart, intestine and bladder (25, 26). One excellent example is the gut-brain-gut communication network that includes several messenger systems, e.g., enteric nervous system with the cells of Cajal, afferent and efferent neurons, immune mediators, gut hormones, metabolic factors and microbial metabolites, carrying information from the gut to the brain and from the brain to the gut (27). Within the peripheral neural networks, chief hub or pacemaker cells are known to exist and function as the central command for the organs in which they reside, for example the sinoatrial node (heart), islets of Langerhans (pancreas), and the interstitial cells of Cajal (intestine) (28-30).

Despite playing major roles in maintaining body homeostasis, the kidneys have been largely overlooked in the context of interoception. This is in part due to our incomplete knowledge of the neural control mechanisms of the kidney and the kidney-brain - kidney axis that is currently limited to the anatomy and function of sympathetic efferent (cell bodies in pre and paravertebral ganglia) and sensory afferent nerves (cell

bodies in dorsal root ganglia) and nerve endings in the renal cortex (31). Importantly, no neuronal somata have been described in the renal cortex, although anatomically and functionally far less-complex organs have local neural control and neural networks. However, the MD-specific expression of the neuronal type of nitric oxide synthase (*Nos1*) in the renal cortex has been long established (20) and preliminary transcriptomic analysis of a limited number of single MD cells expressing neuroepithelial features (32) suggest their neuronal differentiation.

Recent discoveries in tissue regenerative mechanisms suggest the key role of local neuronal activity in direct control of somatic stem cells. Peripheral sensory and sympathetic nerves have been demonstrated to drive epidermal stem cells in wound repair (33) and hair follicle stem cells including melanocytes (34, 35), respectively. The emerging key role of local neurons in endogenous tissue repair fits well with the new clues on MD cell neuron-like sensing and responding to the environment and with their potential links to physiological tissue regeneration.

Here we aimed to develop an MD specific comprehensive research toolbox to study these overlooked cells in unprecedented detail. Applications of these new research tools addressed the hypothesis that MD cells via their novel sensory neuron-like function control progenitor cell-mediated endogenous kidney regeneration. Furthermore, we hypothesized that the MD regenerative program can be activated by the loss of body fluid and salt, which is the primary, organ-specific and evolution-driven physiological signal for the kidney. Consistent with physiological activation being the overarching theme of this work, the same low dietary salt intake stimulatory condition was applied throughout all parts of the study including *in vivo* animal models, transcriptomic analysis, and *in vitro* cell culture.

2. OBJECTIVES

The overall objective of my work was to explore the importance and new roles of the macula densa (MD) in renal physiology, disease, and therapy.

My central hypothesis is that sensory neuron-like MD cell calcium and NGFR signaling play novel, primary roles in physiological responses to control renal hemodynamics, renin, and tissue remodeling in order to maintain body homeostasis (interoception). Furthermore, I hypothesize that MD cells via secreted paracrine factors act on local progenitor cells to orchestrate endogenous kidney tissue remodeling. In addition, alterations in the neuron-like functions of MD cells represent a novel, neurodegenerative component in the pathogenesis of chronic kidney disease (CKD) and can be therapeutically targeted.

In the present work I aimed to:

1. Develop a next generation MD specific research toolbox, including *in vivo* animal models, new *in vivo* multiphoton microscopy approaches to study MD cell function, a newly developed immortalized MD cell line, and bulk and single-cell based MD transcriptome profile.
2. Test the hypothesis that MD cells exhibit sensory neuron-like molecular, structural, and functional features.
3. Test the hypothesis that MD cells regulate endogenous tissue remodeling and repair after injury. I further hypothesize that this program is activated via physiological stimuli and can be therapeutically targeted.

3. METHODS

Animals

Male and female, 6-12 weeks old C57BL6/J or BalbC mice (Jackson Laboratory, Bar Harbor, ME) were used in all experiments. Transgenic mouse models with the expression of various fluorescent reporter proteins and gene knock-out strategies were generated by intercrossing Cre or Cre-ER^{T2} mice with floxed mice as indicated in Table 1. Tamoxifen was administered 75 mg/kg by oral gavage for a total of three times (every other day) for full induction, and one time for partial induction (36) resulting in cell specific expression of reporters and gene knock-out mouse models. A tamoxifen washout period of >2 weeks was always used. Some mice received low-salt diet for 10 to 14 days (TD 90228, Harlan Teklad, Madison, WI) with or without ACE inhibitor treatment using enalapril (150 mg/L via drinking water, E6888 purchased from Sigma Aldrich Solutions, MO) with or without selective COX-2 inhibitor (SC58236, 6 mg/L via drinking water, from Pfizer Inc. New York, NY), or selective Nos1 inhibitor 7-NI (20 mg/kg ip daily injections, N778, Sigma Aldrich, St. Louis, MO). In addition, some mice received chronic nerve growth factor (NGF 0.03 mg/kg in 100 µL PBS sc., N8133, Millipore Sigma, Burlington, MA) treatment for 10 to 14 days, or acute intravenous bolus arginine vasopressin (AVP, 5 µg/kg, V9879 Sigma Aldrich, St. Louis, MO), isoproterenol (Iso, 10 mg/kg I6504 Sigma Aldrich, St. Louis, MO), Angiotensin II (AngII, 800 ng/kg, EK-002-12CE, Phoenix Pharmaceuticals, Burlingame, CA), Furosemide (Furo, 1 mg/kg, Sanofi-Aventis, Budapest, HU), gastrin (1 µg/kg, Sigma Aldrich, St. Louis, MO), L-glutamic acid (Glu, 0.75 mg/kg, G1251, Sigma Aldrich, St. Louis, MO), Gamma-aminobutyric acid (GABA, 50 mg/kg, A2129, Sigma Aldrich, St Louis, MO), nerve growth factor (NGF, 1 mg/kg, N8133, Millipore Sigma, Burlington MA), LM11a 31 dihydrochloride (LM11a, 25 mg/kg, Tocris, Minneapolis, MN), or amyloid precursor protein (sAPPα, 0.6 mg/kg, S9564 Sigma Aldrich Solutions, St. Louis, MO) injection. Some mice received low dose streptozotocin treatment (50 ug/g body weight once a day for five consecutive days, S0130, Sigma Aldrich, St Louis, MO) to induce diabetes mellitus. Animals with blood glucose levels over 300 mg/dL were considered diabetic. None of the treatments resulted in significant alterations in blood pressure based on tail-cuff measurements. All animal protocols were approved by the Institutional Animal Care and Use Committee at the University of Southern California.

Table 1: Animal models

Mouse Model	Cre/ Cre-ER^{T2}	Reporter	Knock-out model	Induction
Ng2-tdTomato	Ng2 (*62*)	tdTomato (*63*)	-	tamoxifen via oral gavage once
Foxd1-tdTomato	Foxd1 (*64*)	tdTomato	-	tamoxifen via oral gavage once at E18.5
Cdh5-Confetti	Cdh5(PAC) (*65*)	(Gt(ROSA)26Sortm1(CAG-Brainbow2.1)Cle/J) (*66*)	-	tamoxifen via oral gavage once
Ren1d-Confetti	Ren1d (*67*)	(Gt(ROSA)26Sortm1(CAG-Brainbow2.1)Cle/J)	-	-
MD-GFP	Nos1 (*68*)	Gt(ROSA)26Sortm4(ACTB-tdTomato,-EGFP)Luo (*69*)	-	tamoxifen via oral gavage 3 times
MD-GFP-Wnt^{lof}	Nos1	Gt(ROSA)26Sortm4(ACTB-tdTomato,-EGFP)Luo	Ctnnb $^{lox(ex8-13)}$ (*70*)	tamoxifen via oral gavage 3 times
MD-GFP-Wnt^{gof}	Nos1	Gt(ROSA)26Sortm4(ACTB-tdTomato,-EGFP)Luo	Ctnnb$^{lox(ex3)}$ (*71*)	tamoxifen via oral gavage 3 times
Wnt-GFP	-	-	TCF/Lef:H2B-GFP (*72*)	
MD-Wnt^{lof} - Wnt-GFP	Nos1	-	Ctnnb$^{lox(ex8-13)}$ TCF/Lef:H2B-GFP	tamoxifen via oral gavage 3 times
MD-Wnt^{gof} - Wnt-GFP	Nos1	-	Ctnnb$^{lox(ex3)}$ TCF/Lef:H2B-GFP	tamoxifen via oral gavage 3 times
MD-GT	Nos1	B6;129S6-Polr2aTn(pb-CAG-GCaMP5g,-tdTomato) Tvrd/J (*73*)	-	tamoxifen via oral gavage 1 or 3 times
Sox2-GT	Sox2 (*74*)	B6;129S6-Polr2aTn(pb-CAG-GCaMP5g,-tdTomato) Tvrd/J	-	-
MD-NGFR-KO	Nos1	B6;129S6-Polr2aTn(pb-CAG-GCaMP5g,-tdTomato) Tvrd/J	Ngfrtm1.1Vk/BnapJ (*75*)	tamoxifen via oral gavage 3 times
NGF-eGFP	-	-	NGFpr-EGFP (*76*)	
Pod-GT (37)	Pod	B6;129S6-Polr2aTn(pb-CAG-GCaMP5g,-tdTomato) Tvrd/J (*73*)	-	-

Adriamycin nephropathy

To establish the animal model of Adriamycin (ADR) induced nephropathy, Balb/C mice at 8 weeks of age received a single iv injection of ADR (10.5 mg/kg, Sigma Aldrich, St. Louis, MO) via tail vein injection and were followed for a total of 6 weeks (38). At the 2 weeks peak of disease when glomerulosclerosis pathology and albuminuria were stabilized, 4-weeks treatment of pre-existing pathology was initiated in the following 5 groups by daily ip injections: (i) control PBS, (ii) low-dose CCN1 (angiogenic modulator, 5 ng/day), (iii) high-dose CCN1 (1 mg/kg/day), control DMEM-F12 cell culture medium, and (v) conditioned macula densa (MD) cell culture medium. At the end of 4 weeks treatment, mice were euthanized, and tissues harvested for histological analysis.

Serial intravital imaging using multiphoton microscopy (MPM)

Surgical implantation of a dorsal abdominal imaging window (AIW) above the left kidney was performed on Ng2-tdTomato and Cdh5-Confetti mice using aseptic surgical procedures as described recently (39). This approach allows the non-invasive imaging of the same glomeruli over time for up to 30 days (40). For repeated MPM imaging of the same mice with AIW, animals underwent brief anesthesia sessions every 3–4 days using 1%–2% isoflurane and the SomnoSuite low-flow anesthesia system (Kent Scientific, Torrington, CT). For acute imaging experiments under continuous anesthesia (Isoflurane 1-2% inhalant via nosecone), the left kidney was exteriorized through a flank incision. Mice were placed on the stage of the inverted microscope with the exposed kidney mounted in a coverslip-bottomed chamber bathed in normal saline as described previously (41, 42). Body temperature was maintained with a homeothermic blanket system (Harvard Apparatus). Alexa Fluor 594 or 680-conjugated albumin (Thermo Fisher, Waltham, MA) was administered iv. by retro-orbital injections to label the circulating plasma (30 µL iv. bolus from 10 µg/ml stock solution). The images were acquired using a Leica SP8 DIVE multiphoton confocal fluorescence imaging system with a 63× Leica glycerine-immersion objective (numerical aperture (NA) 1.3) powered by a Chameleon Discovery laser at either 860 nm or 970 nm (Coherent, Santa Clara, CA) and a DMI8 inverted microscope's external Leica 4Tune spectral hybrid detectors (emission at 460-480nm for CFP, 510-530 nm for eGFP and

GCaMP5, 550-570 nm for YFP, 580-600 nm for tdTomato, 600-620 nm for RFP) (Leica Microsystems, Heidelberg, Germany). The potential toxicity of laser excitation and fluorescence to the cells was minimized by using a low laser power and high scan speeds to keep total laser exposure as minimal as possible. Image acquisition (12-bit, 512×512 pixel) consisted of only one z stack or time series per tissue volume (<2-10 min), which resulted in no apparent cell injury. For tissue volume and cell density analysis fluorescence images were collected in volume series (xyz, 1 s per frame) with the Leica LAS X imaging software and using the same instrument settings (laser power, offset, gain of all detector channels). Serial imaging of the same glomerulus in the same animal/kidney was performed once every 3 to 4 days for up 14 days after the first imaging session. Maximal projections from *Z*-stacks were used to count and compare tdTomato and Confetti$^+$ cell number in the same area over time. In the Confetti mouse models clonal or unicolor tracing units were defined as numerous directly adjacent individual cells that featured the same Confetti color combination. All ten possible Confetti color combinations were observed as described before (43). The counting of tdTomato or Confetti$^+$ cells and clones was facilitated by standardized image thresholding using ImageJ (NIH), Leica LAS X (Leica Microsystems Inc.), and cell-counting algorithms of Imaris 9.2 3D image visualization and analysis software (Bitplane USA) for intravital imaging *Z*-stacks. Clone frequency (the percentage of clones formed by 1, 2, 3-6, or >7 individual Confetti cells relative to all clones (100%)) was analyzed using mixed-effect analysis with two-way ANOVA. To study dynamic changes in intracellular calcium signaling in MD and other renal cell types, fluorescence images were collected in time series (xyt, 526 ms per frame) with the Leica LAS X imaging software and using the same instrument settings (laser power, offset, gain of both detector channels). The strong MD cell-specific tdTomato fluorescence signal (44) and high-resolution MPM imaging allowed for easy identification of single MD cell bodies and processes. MPM imaging was always performed at the same time of day.

Quantification of GCaMP5 fluorescence intensity

An optical section including the vascular pole and the MD of a superficial glomerulus was selected, and time (xyt) series with 1 frame per 526 milliseconds were recorded for 3 to 10 minutes to measure MD cell calcium dynamics. The strong, positive

signal (GCaMP5/tdTomato fluorescence) and high-resolution MPM imaging allowed for easy identification of single MD, JG, EGM, IGM, EA and AA smooth muscle cell bodies. For the quantification of changes in mean GCaMP5 fluorescence intensity ROIs were drawn closely over the total cell body of single cells or over the entire MD plaque and the changes in GCaMP5 F/F_0 (green channel; fluorescence intensity expressed as a ratio relative to baseline) were measured after the experiment in the defined ROI using the Quantify package of LAS X software (version 3.6.0.20104; Leica-Microsystems). MD whole plaque data were smoothed using exponential 2^{nd} order smoothing method (50 neighbors, GraphPad Prism). The frequency of MD calcium transients was measured based on the same defined ROIs using 3 to 10 minutes long time series recordings before and after manipulation. Maximum projection images of time series were generated (t=3min) to measure cumulative GCaMP5 fluorescence intensity over time.

Pearson's (*R*-based) connectivity analyses

Correlation analyses between the calcium signal time series for all MD cell pairs were performed with GraphPad Prism 9.0.1. as described (45). The correlation function R between all possible cell-pair combinations was assessed using Pearson's correlation. Data were displayed as heat-map matrices, indicating individual cell-pair connections on each axis (minimum = −1; maximum = 1). $P < 0.001$ was deemed a statistically significant cell–cell connection. The coordinates of the imaged cells were used in the construction of connectivity line maps. Cell pairs ($R > 0.35$ and $P < 0.001$) were connected with a red straight line. MD cells with the most connections were labeled light red, MD cells without any apparent correlation to other MD cells were labeled light blue.

Glomerular filtration rate measurement

GFR measurements were performed using the MediBeacon Transdermal Mini GFR Measurement System (MediBeacon) as described previously (46). Briefly, mice were anesthetized, MediBeacon sensor was placed on the depilated dorsal skin. Mice were injected retro-orbitally with the inulin analog exogenous GFR tracer fluorescein-isothiocyanate conjugated sinistrin (FITC-S 7.5 mg/100 g body weight, MediBeacon, St. Louis, MO). The excretion kinetics of the FITC-S was measured for 90 minutes. GFR

was then calculated based on the decay kinetics (half-life time) of FITC-S using MediBeacon Data Studio software (MediBeacon).

Blood pressure measurement

Systolic blood pressure was measured by tail-cuff plethysmography (Visitech BP-2000, Visitech System Inc.) in trained animals as previously described (47).

Tissue processing, immunofluorescence, and histology

Immunofluorescence detection of proteins was performed as described previously (47). Briefly, cryosections were cut at 25 µm, washed with 1x PBS. Paraffin tissue blocks were sectioned to 8 µm thick. For antigen retrieval, heat-induced epitope retrieval with Sodium Citrate buffer (pH 6.0) or Tris-EDTA (pH 9.0) was applied. To reduce non-specific binding, sections were blocked with normal serum (1:20). Primary and secondary antibodies were applied sequentially overnight at 4º C and 2 hours at room temperature. Primary antibodies and dilutions were as follows, anti-villin antibody (1:100, sc58897, Santa Cruz Biotechnology, Dallas, TX), anti-claudin1 antibody (1:100, SAB4503546, Sigma Aldrich, St. Louis, MO), anti-renin antibody (1:100, AF4277, R&D Systems, Minneapolis, MN), anti-alpha smooth muscle actin antibody (αSMA, 1:100, A2547, Sigma Aldrich, St. Louis, MO), anti- platelet-derived growth factor receptor beta antibody (PDGFRβ, 1:100, 3169S, Cell Signaling Technology, Danvers, MA), anti-podocin antibody (1:100, SC22298, Santa Cruz Biotechnology, Dallas, TX), anti-CCN1 antibody (1:100, SC13100, Santa Cruz Biotechnology, Dallas, TX), anti-growth differentiation factor 15 antibody (GDF15, 1:100, HPA011191, Sigma Aldrich, St. Louis, MO), anti-pappalysin2 antibody (PAPPA2, 1:100, PA5-21046, Invitrogen, Waltham, MA), anti-Wilms tumor protein antibody (WT1, 1:100, AB89901, Abcam, Cambridge, UK), anti-CD34 antibody, (1:100, AB8536, Abcam, Cambridge, UK), anti-Meis2 antibody (1:100, HPA003256, Sigma Aldrich, St. Louis, MO), anti-tyrosine-hydroxylase antibody (TH 1:100, AB152, Millipore Sigma, Burlington, MA), anti-calcitonin gene related peptide antibody (CGRP:100, AB36001, Abcam Cambridge, UK), anti-synaptophysin antibody (SYP 1:100, PA5-27286, Thermo Fisher, Waltham, MA), anti-nerve growth factor receptor antibody (p75NTR 1:100, ab227509, Abcam Cambridge, UK), anti-tropomyosin kinase A/B antibody (TRKA/B 1:100, A7H6R, Cell

Signaling Technology Danvers, MA), anti-cyclooxygenase 2 (COX2) antibody (1:100, 12282S, Cell Signaling Technology, Danvers, MA,), anti-Na-K-2Cl cotransporter antibody (NKCC2 1:100, Developmental Studies Hybridoma Bank, created by the NICHD of the NIH and maintained at The University of Iowa, Department of Biology, Iowa City, IA 52242), anti-renin antibody (1:100, AF4277, R&D Systems, Minneapolis, MN), anti-phospho-Tau antibody ($pTau^{S199}$1:100, 44-734G, Waltham, MA), anti-GFP antibody (GFP 1:200 Thermo Fisher Scientific, Waltham, MA). Alexa Fluor 488, 594, and 647-conjugated secondary antibodies were purchased from Invitrogen. Slides were mounted by using DAPI-containing mounting media (VectaShield, Vector Laboratories Inc., Burlingame, CA). Sections were examined with Leica TCS SP8 (Leica Microsystems, Wetzlar, Germany) confocal/multiphoton laser scanning microscope systems as described previously (36). Imaging software (Image J, National Institutes of Health and the Laboratory for Optical and Computational Instrumentation (LOCI, University of Wisconsin) was used to calculate the percent area of colocalization to determine the changes in the proportion of $NG2^+$ cells in each cell type, as well as the proportional distribution of $NG2^+$cell types.

For the assessment of tubulointerstitial fibrosis, histological analysis of Picrosirius red (PSR) staining was performed on mouse kidney sections using Sirius Red F3B (Sigma-Aldrich, St. Louis, MS). For the evaluation of glomerulosclerosis, histological analysis of periodic acid-Schiff stain was performed on mouse kidney sections using PAS Stain Kit (24200-1, Polysciences, Warrington, PA). Images were visualized at 25× magnification using Leica TCS SP8 (Leica Microsystems, Wetzlar, Germany). Imaging software (Image J) was used to calculate the percent area of red-stained collagen or PAS positive areas as described before (48).

Antibodies that were used in immunostaining and blotting performed in our laboratory were validated using specific blocking peptides if these were available. Some of the human kidney immunohistochemistry images were obtained from the Human Protein Atlas (http://www.proteinatlas.org) that were obtained with antibodies that have not been fully validated in the current studies (49).

Tissue CLARITY

Three-dimensional imaging was performed as previously described (36, 50) by carrying out whole-mount immunofluorescence stains on slices of MD-GFP WT mouse kidneys. Slices were fixed in 4% formaldehyde in 1x phosphate buffer saline (PBS) at room temperature for 45 min, washed in 1XPBS, blocked in 1xPBS with 0.1% TritonX100 and 2% SEA Block (ThermoFisher Scientific) for 1 hour, and sequentially incubated in primary and secondary antibodies over 2 days. Primary antibodies and dilutions were as follows: anti-renin antibody (1:100, AF4277, R&D Systems, Minneapolis, MN), and anti-tyrosine-hydroxylase antibody (AB152, MilliporeSigma, 1:100), GFP (ThermoFisher, 1:200). Primary and secondary antibodies were diluted in the blocking solution. To clear tissue slices, the slices were dehydrated in methanol via increasing concentrations 50%, 75%, 100%, diluted in PBS - each for 1hr - and subsequently submerged in a 50:50 benzyl benzoate/benzyl alcohol (BABB): methanol solution, followed by 100% BABB. High resolution imaging of MD plaques and the adjacent glomeruli was performed on a Leica SP8 multiphoton microscope using a 63X glycerol immersion objective.

MD cell isolation

MD-GFP cells were isolated as described before (36). Briefly, kidney cortex was isolated from freshly harvested mouse kidneys and digested using Hyaluronidase and Liberase TM enzyme combination (concentration: 2 mg/mL and 2.5 mg/mL respectively, Sigma Aldrich, St. Louis, MO). After digestion, MD cells were isolated based on their genetic reporter expression (GFP) by using FACS ARIAII cell sorter, and excitation wavelengths 488 and 633 nm in sterile conditions. The highest tdTomato expressing cells were collected as controls with high representation of distal tubule and collecting duct segments, podocytes, and vascular smooth muscle cells.

RNA sequencing and bioinformatics

Whole-transcriptome RNAseq was performed at the USC Norris Molecular Genomics Core as described before (51). Cells were extracted using Qiagen miRNeasy purification kit following manufacturer's protocol for total RNA purification (Qiagen cat#217004). Libraries were simultaneously prepared using Takara's SMARTer

Stranded Total-RNA Pico v2 library preparation kit following manufacturer's protocol (Takara cat#634412). Prepared libraries were sequenced on Illumina Nextseq500 at 2x75cycles.

RNA-seq data was analyzed using the RNA-seq workflow in Partek Flow software (V10.1.21. Partek Inc., St. Louis, MO, USA). Briefly, the raw sequencing reads were first trimmed based on the quality score (Phred QC>=20, min read length=25 nt) before mapped to mouse genome build mm10 using Star 2.61 (52) with default parameter settings and Gencode M21 mouse transcriptome annotation (53) as guidance. Gencode M21 was then used to quantify the aligned reads to genes using Partek E/M method. Finally, gene level read counts in all samples were normalized using Upper Quartile normalization (54) and subjected to differential expression analysis using Partek Gene Specific Analysis method (genes with fewer than 10 aligned reads in any sample among a data set were excluded). The differentially expressed gene (DEG) lists were generated using the cutoff of FDR<0.05 and fold changes greater than 2.0 either direction. Z-scores based on the normalized gene counts from the top MD cell enriched genes in 5 categories were used to generate the heatmap in GraphPad Prism 9.0.1 (San Diego, California). Pathway analysis, graphical summary, biological and disease functions of IPA were used to analyze transcriptome data.

Single cell RNA sequencing was prepared using 10x Genomics 3' v3.1 (cat# 1000092) following manufacturer's protocol as described before. Samples were parsed into single cells using 10x Genomics Chromium Controller and libraries were simultaneously prepared. Prepared single cell RNA sequencing libraries were sequenced on the Illumina Novaseq6000 platform at a read length of 28x90 and read depth of 100,000 reads/cell for 2000-4000 cells. scRNAseq data was analyzed using the scRNAseq workflow by Partek Flow. Briefly, the raw sequencing reads with adaptors trimmed were mapped mm10 genome using Star 2.6.1 and quantified using Gencode M25 annotation to generate gene level counts. The gene counts were subjected to QA/QC and the low-quality cells were filtered using the following criteria: (1) contained less than 300 or more than 8000 detected genes, (2) mitochondrial counts higher than 15% of total counts. The counts were normalized using the Partek Flow recommended method (divided by 1 million, Add:1 and log2). Dimension reduction was carried out using PCA, followed by Graph-based Clustering with default settings and UMAP visualization (55). Cell

populations were determined by expression of relevant biomarkers. A 5-fold thresholding in *Nos1* and *Pappa2* expression was applied to filter out potential non-MD cell contamination. *Nos1/Pappa2* expression filtered cells went through PCA, Graph-based clustering and UMAP visualization.

Generation of the MD^{geo} cell line

Freshly isolated MD cells were plated at a density of $0.5^{x}10^{5}$ cells/well in a 24-well plate and primary cultured at 37 °C 5% CO_2 in Dulbecco's Modified Eagle Medium: Nutrient Mixture F-12 (DMEM-F12, Gibco, Thermo Fisher Scientific) supplemented with 10% Fetal Bovine Serum (FBS, Thermo Fisher Scientific), 1% Penicillin-Streptomycin (P/S 10,000 U/mL, Thermo Fisher Scientific) and 0.0005% of Dexamethasone. At 80% confluence, cells were infected using Lenti-SV40 (ts58 temperature sensitive mutant, 10^6 IU/mL, LV629, Applied Biological Materials) Lentivirus to achieve temperature sensitive immortalization, proliferation of MD cells at 33 °C and differentiation of MD cells at 37 °C according to manufacturer's instructions. Briefly, cells were infected two times 8 hours apart using MOI:3 to achieve optimal viral density and incubated for 24 hours at 37°C, 5% CO_2 in the presence of Polybrene (5 ug/mL). Lentiviral vector was diluted with complete MD cell culture media to avoid cytotoxicity. After 24 hours incubation cells were cultured in complete MD cell culture media supplemented with IFN-Gamma (0.01 ug/mL) and nerve growth factor (NGF, 0.1 ug/mL; N8133, Millipore Sigma) at 33°C for proliferation. IFN-Gamma concentration was decreased gradually after 1 week. Importantly, NGF supplementation was crucial for MD cell survival. Cells were subcultured after 48 hours. For differentiation, cells were incubated at 37°C, 5% CO2 for 14 days in complete MD cell culture media supplemented with NGF (0.1 ug/mL; N8133, Millipore Sigma). All experiments were completed between 10th and 15th cell passage.

NO assay

To assess nitric oxide (NO) synthesis in MD^{geo} cells NO sensitive Diaminofluorescein-FM diacetate (D1946, DAF-FM DA, Millipore Sigma, Burlington, MA) was used as described before (56). Briefly, fully differentiated MD^{geo} cells were loaded with DAF-FM DA (10 µg/mL for 10 minutes) either in the presence or absence of

the selective inhibitor of neuronal nitric oxide synthase (7-Nitroindazole (7NI) or Nω-propyl-l-arginine (NPA)). NO synthesis was measured based on the increase in the fluorescence intensity of DAF-FM (F/F_0 green channel; fluorescence intensity expressed as a ratio relative to baseline) over time. Fluorescence emission was detected at baseline, and after 30, 60, and 90 minutes at 515 +/- 15 nm emission wavelength in response to 495 nm excitation using Leica SP8 DIVE multiphoton confocal fluorescence imaging system. Changes in DAF-FM DA F/F_0 were measured after the experiment using the Quantify package of LAS X software (3.6.0.20104; Leica-Microsystems).

PGE2 biosensor technique

PGE2 biosensor cells were used as described before (21). In brief, PGE2 biosensor cells were specifically engineered human embryonic kidney cells (HEK 293 cells) to express the calcium-coupled PGE2 receptor EP1, leading to a calcium response upon PGE2 binding. HEK-EP1 cells were loaded with Fluo-4 and Fura Red (1 μM, for 10 min) and positioned next to the fully differentiated MD^{geo} cells in culture. MD^{geo} cell PGE2 production was measured based on the biosensor cell intracellular Ca^{2+} concentration signal, which was detected by increases in Fluo-4/Fura Red (F/F_0) fluorescence intensity ratio over time. Fluorescence emission was detected every 526 ms using a Leica SP8 DIVE multiphoton confocal fluorescence imaging system as described above (emission at 460-520 nm for Fluo-4 and at 580-640 nm for Fura Red) (Leica Microsystems, Heidelberg, Germany).

Generation of conditioned MD^{geo} cell culture media

The newly established immortalized macula densa cell line (MD^{geo}) was cultured and differentiated as described above. After full differentiation, MD^{geo} cells were washed in PBS to remove FBS and NGF and were physiologically activated by temporary exposure to low-salt conditions (DMEM-F12 medium) (22) for 6 hours every other day (3 times). Cell culture media was collected in sterile conditions and stored at -80 C until treatment.

Western Blot

For immunoblotting of mouse cortical homogenates, manually dissected slices of kidney cortex were homogenized in a buffer containing 20 mM Tris·HCl, 1 mM EGTA pH 7.0, and a protease inhibitor cocktail (BD Bioscience, San Jose, CA). Protein (40 μg) was processed for immunoblotting as described previously (47). Primary antibodies and dilutions were as follows: anti-Ccn1 (1:500, SC13100, Santa Cruz Biotechnology, Dallas, TX), anti-Sema3C (1:500, MAB1728, R & D Systems, Minneapolis, MN), anti-Ccn3 (1:1000, ab137677, Abcam, Cambridge, UK), anti-Cxcl14 (1:1000, NBP1-31398, Novus Biologicals, Centennial, CO), anti-p75NTR antibody (1:1000, ab227509, Abcam, Cambridge, UK), anti-COX2 antibody (1:1000 12282S, Cell Signaling Technology, Danvers, MA), anti-NKCC2 cotransporter antibody (1:1000 Developmental Studies Hybridoma Bank, created by the NICHD of the NIH and maintained at The University of Iowa, Department of Biology, Iowa City, IA 52242), anti-neuronal nitric oxide synthase antibody (Nos1, 1:1000, SC648, Santa Cruz Biotechnology, Dallas, TX) anti-phospho and total extracellular signal-regulated kinase antibody (p/total ERK1-2, 1:1000 CST4396, CST4696, Cell Signaling Technology, Danvers, MA), anti-phospho and total protein kinase B antibody (AKT, 1:1000, CST2920, CST4060, Cell Signaling Technology, Danvers, MA), anti-phospho and total IkB kinase antibody (p/total IkB, 1:1000, 1:500, CST9246S, CST924, Cell Signaling Technology, Danvers, MA), anti-phospho and total panTrk (1:1000, 4619S, 92991S, Cell Signaling Technology, Danvers, MA), anti-renal outer medullary potassium channel antibody (ROMK, 1:2000, APC-001, Alomone Labs, Jerusalem, Israel), anti-phospho and total p38 mitogen-activated protein kinase antibody (p/total p38, 1:1000, Cell Signaling Technology, Danvers, MA). After incubation, blots were incubated with secondary antibodies (1:5000; LI-COR Biosciences) and then visualized with Odyssey Infrared Imaging System (LI-COR Biosciences). Protein staining of the gel (Coomassie staining) was performed and analyzed to confirm equal loading as described previously (57).

Mass spectrometry analysis of the composition of MD^{geo} cell culture media

Cell-free MD^{geo} conditioned media were snap frozen and stored at −80°C. Proteins were precipitated using acetone. Proteins were digested and prepared using the SP3 protocol, with modifications, as previously described, using trypsin as a protease

(58). Tryptic peptides were analyzed using a nanoscale liquid chromatography–tandem mass spectrometry hardware setup, consisting of a nanoflow LC (flow, 200 nl/min) coupled to an Orbitrap QExactive Plus tandem mass spectrometer. The peptides were separated using a gradient for reverse-phase separation, consisting of buffer A and buffer B, with ascending concentrations of buffer B (80% acetonitrile, 0.1% formic acid) over buffer A (0.1% formic acid). The peptides were separated using a 1-hour gradient. Protein raw files were searched using MaxQuant and the LFQ algorithm (59, 60) with searches against a UniProt mouse proteome reference database released in January 2018. Search criteria were alkylation on cysteines as a fixed modification, and amino-terminal acetylation and methionine oxidation as variable modifications. Default criteria were used, meaning that PSM, peptide, and protein false discovery rates (FDRs) were set at 0.01. The LFQ algorithm was enabled, and "match between run" was enabled. The data were analyzed using Perseus version 1.5.5.3, with filtering for the embedded annotations as contaminant, reverse, or proteins identified by site only.

CCN1 Assay

Mouse CYR61 (CCN1) ELISA Kit (ab253223, Abcam, Cambridge, UK) was used for the quantitative measurement of CCN1 protein in MD^{geo} cell culture media with or without conditioning according to the manufacturer's instructions.

Statistical methods

Data are expressed as average ± SEM and were analyzed using Student's t-tests (between two groups), or ANOVA (for multiple groups) with post-hoc comparison by Bonferroni test. $P<0.05$ was considered significant. Statistical analyses were performed using GraphPad Prism 9.0c (GraphPad Software, Inc.).

4. RESULTS

4.1 Development and characterization of a next generation MD cell research toolbox

4.1.1 The generation of MD targeting *in vivo* mouse models

Although macula densa (MD) cells are chief regulatory cells in the nephron, they have been difficult to study in full detail due to their inaccessibility and limited research tools available to specifically target them. To overcome these limitations, we first developed several MD cell targeting *in vivo* genetic mouse models using the classic MD cell-specific marker nNOS in a Cre/lox-based genetic strategy (Fig. 2A). MD-GFP or GT mice were generated by intercrossing NOS1/CreERT2 and mTmG/fl mice (36) or GCaMP5-tdTomato/fl mice (61) respectively. As described previously, MD-GFP mice

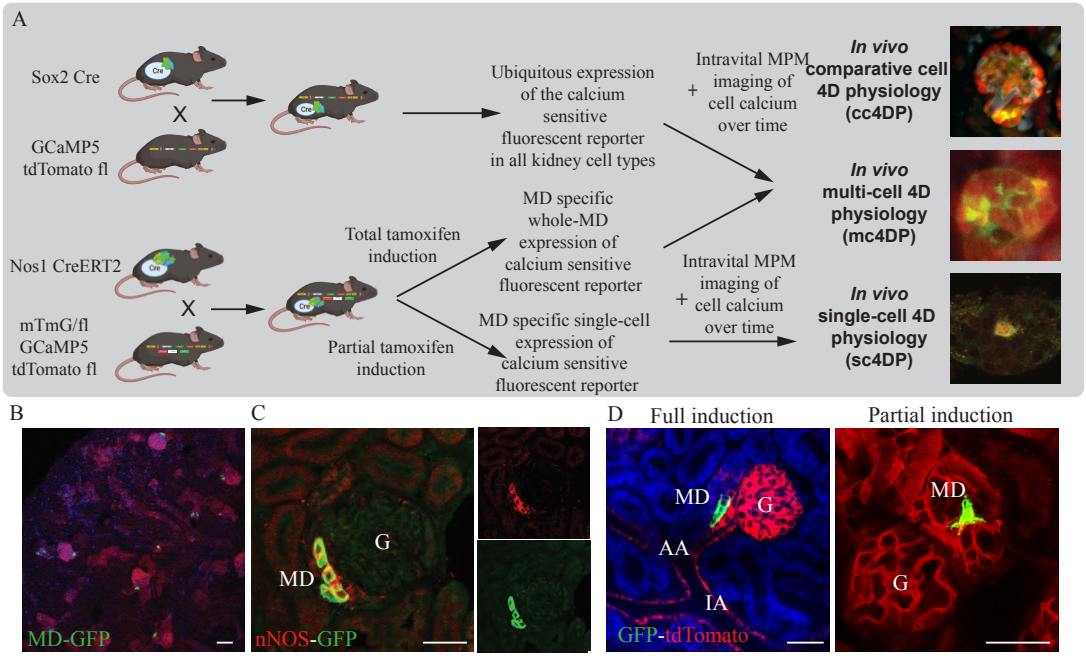

Figure 2. A: Illustration of the experimental workflow using transgenic mouse models, Cre-lox induction strategies, and intravital MPM imaging of cell calcium over time to study 4D physiology in comparative (cc4DP), multi-cell (mc4DP), and single-cell (sc4DP) modes. Representative intravital MPM images are shown for each of the three experimental modes. **B**: Overview of a MD-GFP mouse kidney section with membrane-targeted enhanced GFP (eGFP) expression in MD cells (green), and membrane-targeted tdTomato expression in all other kidney cell types (red). Nuclei were labeled with DAPI (blue). Note that all green cells were localized directly adjacent to intensely red-labeled glomeruli (G). **C**: Immunofluorescence double labeling of the MD cell marker neuronal nitric oxide synthase (nNOS) (red) and the nNOS-driven eGFP reporter (green). The overlay image shows co-localization (yellow) confirming MD-specific expression of eGFP. **D**: Fluorescence images of MD-GFP mouse kidney sections showing longitudinal and cross-sectional views of the MD cell plaque after full (left) or partial (right) induction of eGFP expression by tamoxifen. The left image shows tissue autofluorescence (blue) for additional morphological detail. Scale bar = 50 µm. (Adapted from (36, 61).

feature MD-specific, tamoxifen-inducible membrane-targeted enhanced GFP (eGFP) expression in the renal cortex, whereas other cell types remain red by expressing the membrane-targeted red fluorescent protein tdTomato (Fig. 2B). Similarly, MD-GT mice express the cytosolic calcium sensitive green fluorescent protein GCaMP5, and the calcium insensitive red fluorescent protein tdTomato specifically in MD cells in the renal cortex. MD specific expression of GFP/GCaMP5 was confirmed by performing immunofluorescence double labeling of nNOS and eGFP. Co-labeling of nNOS and eGFP only in MD cells confirmed the validity and specificity of the applied genetic approach (Fig. 2C) (36). Next, tamoxifen dosing was adjusted to alter the level of Cre induction and hence the density of GFP or GCaMP5/tdTomato-labeled MD cells in the renal cortex. Fig. 2D left panel shows labeling of the entire MD plaque after full induction, whereas partial induction led to sporadic MD cell labeling, only 1 to 3 MD cells/plaque on average (Fig. 2D right). The newly developed transgenic MD-GFP and MD-GT mouse models combined with the altered level of Cre induction strategies enabled the visualization and functional assessment of single MD cells, the MD plaque as a functional unit, as well as the isolation of MD cells for *in vitro* cell culture studies and RNA seq and transcriptome analysis. Sox2-GT mice were developed with ubiquitous expression of the same genetically encoded calcium reporter GCaMP5 (G) along with the calcium-insensitive tdTomato (T) in all kidney cell types for comparative analysis of MD cell function to other renal cell types (61). We applied three main strategies to study cell physiology in four dimensions (4DP, in tissue volume over time) in either comparative cell (cc4DP), multi-cell (mc4DP), or single-cell (sc4DP) modes as summarized in Fig. 2A.

4.1.2 The development of new *in vivo* multiphoton microscopy approaches to study MD cell function

To study MD function *in vivo* we developed several unbiased intravital imaging approaches using multiphoton microscopy (MPM). Calcium signaling, changes in renal hemodynamics, and the local kidney tissue microenvironment was studied to search for direct visual clues concerning renal physiology and disease. Intracellular calcium $[Ca^{2+}]_i$ transients and signaling are classic functional readouts of cell function. Intravital MPM imaging enables the visualization of changes $[Ca^{2+}]_i$ in response to physiological or

pathophysiological stimuli with high temporal and spatial resolution (62). In addition, these imaging studies using cell-specific expression of genetically encoded calcium reporters showed detailed micro-anatomical features of different cell types, including podocytes and their primary and secondary cell processes (62). MPM imaging also provides qualitative and quantitative *in vivo* visual clues regarding alterations in renal hemodynamics (63), kidney structure and function and the potential major molecular and cellular mechanistic drivers at play during disease pathogenesis (64). Figure 3 illustrates the novel approaches of *in vivo* MPM imaging to measure changes in $[Ca^{2+}]_i$, and hemodynamics, including single afferent and efferent arteriole blood flow (62, 63).

To better understand the dynamics of cellular remodeling of the local tissue environment in the intact living kidney we next developed several transgenic mouse models to specifically label mesenchymal (Ren1d, NG2, Foxd1) and endothelial (Cdh5) progenitor cells using the multicolor Confetti fluorescent reporter construct: membrane-targeted CFP, nuclear GFP, cytosolic YFP or RFP (Fig. 4A). As a result of the genetic

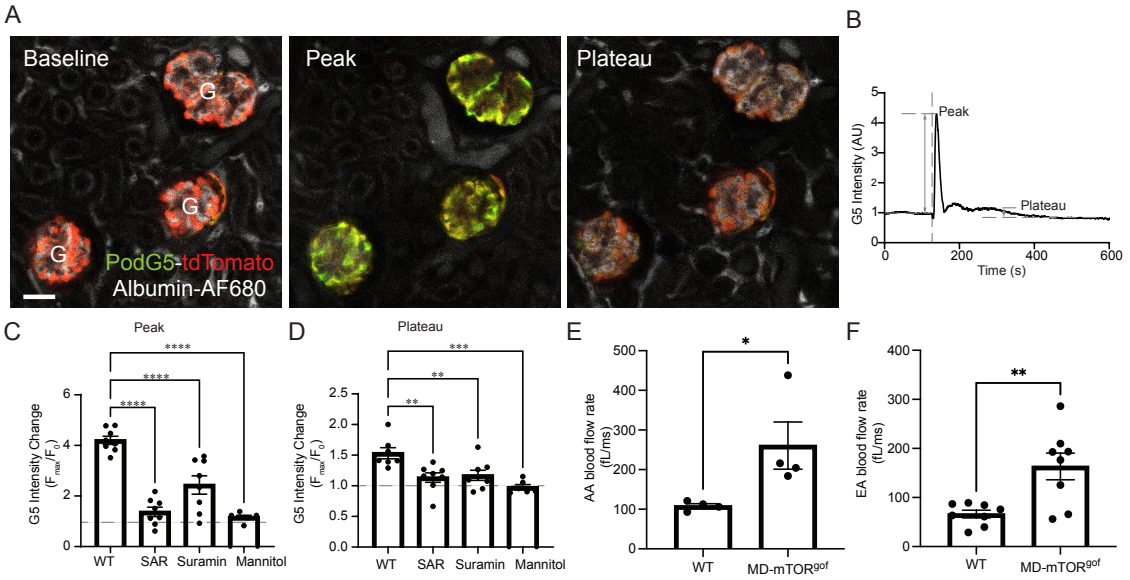

Figure 3. A: Representative intravital MPM images of the same glomeruli from WT Pod-GCaMP5(G5)/tdTomato mice at baseline (left), and at the peak (center) and plateau phase (right) of acute hyperglycemia-induced elevations in podocyte $[Ca^{2+}]_i$. Overlay of calcium-sensitive GCaMP5 (PodG5, green), calcium-insensitive tdTomato (red), and plasma marker (albumin-Alexa Fluor 680) signals (top row), or GCaMP5 (green) signals shown separately (bottom row). Note the robust elevations in GCaMP5 signal at peak compared to plateau or baseline. **B:** Representative recording of podocyte $[Ca^{2+}]_i$ in response to acute hyperglycemia, with peak and plateau phases indicated. **C-D:** Summary of the peak (C) or plateau (D) phase of acute hyperglycemia-induced podocyte $[Ca^{2+}]_i$ elevations (normalized to baseline, dashed line) in untreated WT mice. **E-F**: Statistical summary of AA and EA blood flow. Data represent mean ± SEM, * p,0.05, **: P<0.01, ****: P < 0.0001, 2 glomeruli/mouse from n = 4-8 mice in each group. Scale bar = 50 μm. Adapted from (62-63).

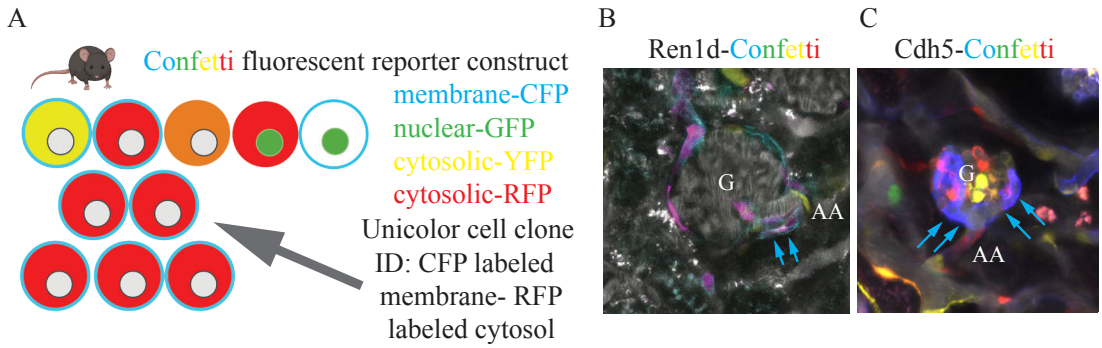

Figure 4. A: Schematic illustration of the Confetti fluorescent reporter construct. Target cells express a unique color combination of 2 fluorescent reporter (homozygous animals – two copies of the transgene) serving as an ID tag of the individual progenitor cells. Progenitor cells when proliferate pass on that unique color combination of expressed fluorescent reporters to daughter cells hence forming unicolor cell clones. **B-C:** Representative *in vivo* MPM image of a glomerulus (G) its afferent arteriole (AA) and the surrounding tubular and vascular structures in a Ren1d-Confetti (B) and Cdh5-Confetti (C) mouse kidney. Note the appearance of unicolor multi-cell clone (blue-red (B) and blue (C)– arrows) at the vascular pole after stimuli.

strategy and the multicolor fluorescent reporter, we were able to identify individual progenitor cells that were randomly labeled with a unique color combination (43).

Next, serial intravital MPM imaging of the same glomerulus in the same mouse and kidney over several days and weeks was performed by surgically implanting a dorsal abdominal imaging window (AIW). This approach enabled the identification and tracking of individual progenitor cells and the detection of the appearance of unicolor multi-cell clones over time (Figure 4B-C). In addition, these studies confirmed the presence of a great number of superficial glomeruli in the mouse renal cortex and their availability for performing qualitative and quantitative imaging measurements (43, 62-64).

4.1.3 The development of the immortalized mouse MD cell line

A new immortalized mouse MD cell line that we named mMD^{geo} was generated for cell biology studies *in vitro* by following a commonly used workflow as illustrated in Fig. 5A and described previously (61). The mMD^{geo} cell line development consisted of primary culturing of freshly isolated and sorted MD cells from MD-GFP kidneys, followed by transfection with LentiSV40 tsA58 for temperature-sensitive proliferation (at 33 °C) or differentiation (at 37 °C for two weeks) in the presence of Ngf. As with the parent MD-GFP mouse model, the cultured mMD^{geo} cell monolayer retained membrane-targeted GFP expression and had a cobblestone pattern typical for epithelial cells (Fig. 5A-B). The MD phenotype of mMD^{geo} cells was validated by the high expression of

classic MD cell markers including Cox2, Nkcc2, and Romk (Fig. 5B-C). Differentiated mMD^{geo} cells had almost 10-fold higher expression of Cox2 and Nkcc2 compared to either undifferentiated mMD^{geo} cells grown at 33°C or the formerly established but now extinct MD cell line MMDD1 (Fig. 5C). As validation of their intact physiological function, mMD^{geo} cells exhibited the classic phenotype of increased pERK1/2, Cox2, and pp38 expression in response to low salt culture conditions (Fig. 5C). Another classic hallmark of MD cells, Nos1-mediated NO release, and Cox2-mediated PGE_2 production was confirmed intact in mMD^{geo} cells (Fig. 5D). Interestingly, the heterogeneity of the MD cell population was preserved in the MD^{geo} cell culture with cells showing variable size and shape (Fig. 5A-B), Cox2 and Nkcc2 expression (Fig. 5B), and NOS activity (Fig. 5D).

4.1.4 Profiling of the MD transcriptome

Next, we aimed to establish the molecular signature of MD cells and their function in control and activated (low salt - LS) condition. The workflow included bulk and single-cell RNA sequencing and transcriptomic analysis (Fig. 6A). A total of 28,000 MD cells (representing a very minor fraction, ~0.2% of the total kidney cortical cell population) and 50,000 control cells from adjacent tubule segments were isolated from the cortex of freshly digested MD-GFP kidneys (n=2 mice for MD and n=4 mice for control cells from each condition) for bulk RNA isolation and transcriptome analysis. For single-cell RNA sequencing and transcriptome analysis, 894 and 1296 MD cells were analyzed from control and LS-induced conditions, respectively, each from a single MD-GFP mouse. Characterization and validation of the bulk RNA sequencing approach, including the high-level expression of known MD cell markers are shown in Fig. 6C. Principal component analysis (PCA) and volcano plot was used to visualize differences in gene expression in MD cells compared to control (Fig. 6B). This approach identified numerous over and under expressed genes in MD cells compared to the control renal tubule cells. Data from bulk RNA-based MD transcriptome analysis is available at the Gene Expression Omnibus (GEO) repository at the National Center for Biotechnology Information (NCBI), with GEO accession number GSE163576. For single-cell RNA-based MD transcriptome analysis, GEO accession number is GSE189954.

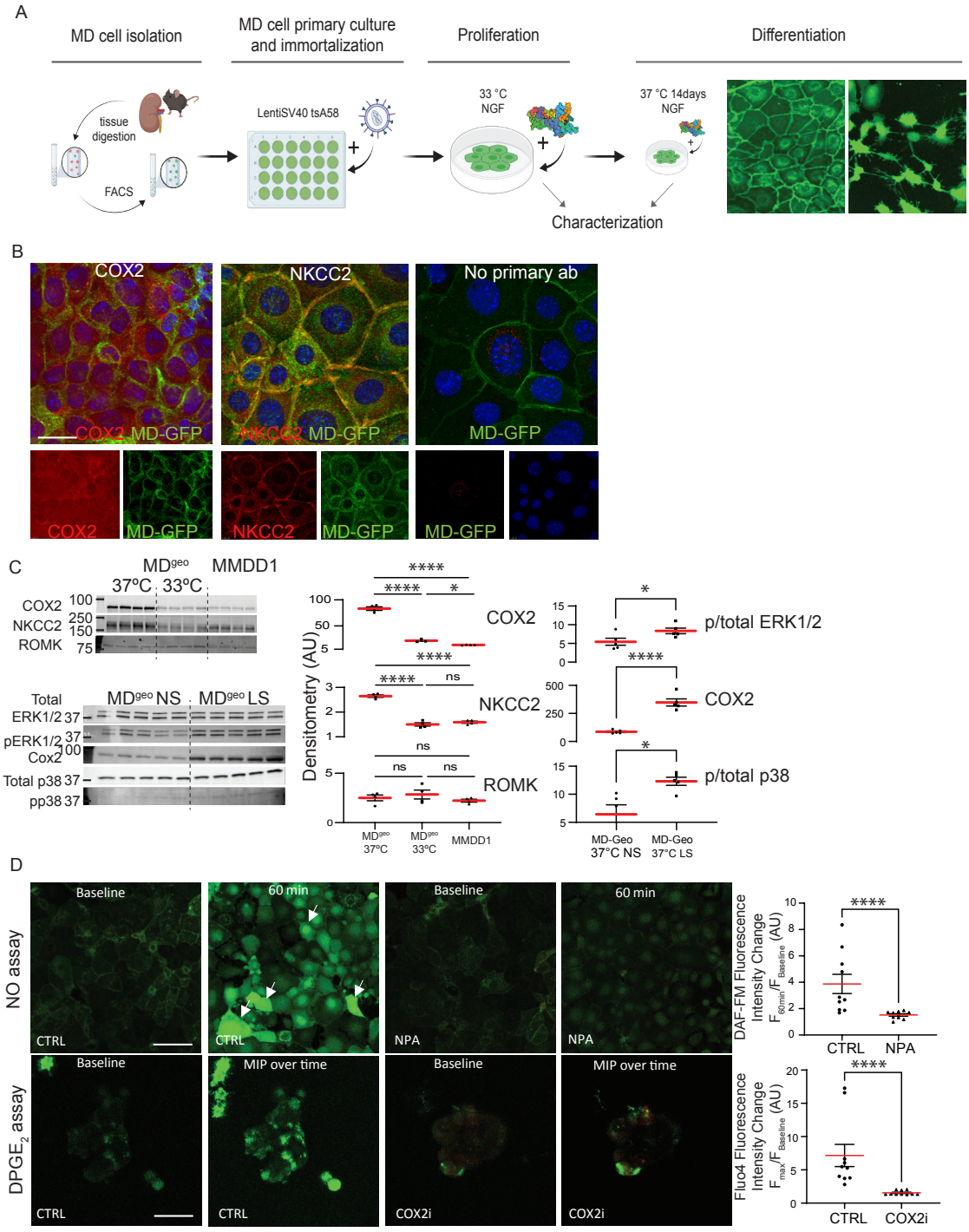
A
MD cell isolation
MD cell primary culture and immortalization
Proliferation
Differentiation
tissue digestion
FACS
LentiSV40 tsA58
33 °C NGF
37 °C 14days NGF
Characterization
B
COX2
NKCC2
No primary ab
COX2 MD-GFP
NKCC2 MD-GFP
MD-GFP
C
MDgeo 37°C 33°C MMDD1
COX2
NKCC2
ROMK
Total ERK1/2
pERK1/2
Cox2
Total p38
pp38
MDgeo NS MDgeo LS
Densitometry (AU)
p/total ERK1/2
p/total p38
MD-Geo 37°C NS
MD-Geo 37°C LS
D
NO assay
DPGE2 assay
Baseline
60 min
MIP over time
CTRL
NPA
COX2i
DAF-FM Fluorescence Intensity Change
Fluo4 Fluorescence Intensity Change

Figure 5. A: Generation of the novel immortalized mouse MD cell line mMD^{geo}. In the workflow, MD-GFP mouse kidneys were freshly harvested and digested into single cell suspension, and cells were analyzed and sorted based on their fluorescence protein expression (MD cells green, all other kidney cell types red). MD primary cultures were immortalized using LentiSV40 tsA58, and either proliferated at 33°C or placed at 37°C for 14 days for differentiation in the presence of NGF followed by characterization. Right: Representative images of fully differentiated mMD^{geo} cells showing epithelial cobblestone-like pattern, with their cell membrane labeled green with endogenous genetic mGFP expression. Semi-confluent MD^{geo} cells feature long, axon-like cell processes. **B:** Representative immunofluorescence images of Cox2 and Nkcc2 labeling in mMD^{geo} cells showing cytosolic or membrane-targeted localization, respectively. Negative control shows endogenous genetic mGFP expression only. Nuclei are labeled blue with DAPI. Note the co-localization of mGFP and Nkcc2 signals (yellow in overlay) in the cell membrane. In addition to the overlay, separate red and green channels are shown at the bottom. **C:** Representative immunoblots and statistical summaries of Cox2, Nkcc2, and Romk expression in mMD^{geo} cells cultured at 37° and 33°C, and in the previously established but now extinct MMDD1 cell line using immunoblotting of whole cell lysates. The effect of low salt (LS) versus normal salt (NS) culture condition on the ratio of phospho/total ERK1/2, COX2, and phospho/total p38 in differentiated (37° C) mMD^{geo} cells. Ns: not significant, *: $p<0.05$, ****: $p<0.0001$, data are mean ± SEM, n=4-5 each. **D:** Measurement of nitric oxide (NO, top row) and PGE2 (bottom row) synthesis and release in MD^{geo} cells in timed control (at baseline and 60 min) and after preincubation with either selective Nos1 inhibitor NO-propyl-L-arginine (NPA, 300 mM) or selective COX-2 inhibitor SC58236 (100 nM) for Nos1-mediated NO and Cox2-mediated PGE2 detection, respectively. For NO measurement, cells were loaded with the fluorescent NO indicator DAF-FM at 37 °C, and changes in DAF-FM fluorescence intensity (green) were monitored using time-lapse confocal microscopy. Maximum change in DAF-FM fluorescence intensity in the cytoplasm of MD cells was evaluated after 60 minutes and compared to baseline. Note the high DAF-FM fluorescence intensity (heterogenous pattern) in control conditions indicating NO synthesis in MD^{geo} cells. Summary of normalized DAF-FM fluorescence intensity in control condition and after NPA treatment (right panel, n=4 wells, 25 measurements each). For the detection of MDgeo cell PGE2 release, representative maximum projection images of the HEK/EP1 PGE2 biosensor cell signal (cell Ca2+ detected by Fluo4) are shown at baseline and over time. Note the high HEK/EP1 PGE2 biosensor cell signal in control conditions indicating PGE2 release from MD^{geo} cells. Summary of HEK/EP1 PGE2 biosensor cell signal (normalized Fluo4 fluorescence) in control and after selective COX-2 inhibition (COX2i). ***: $p<0.001$, ****: $p<0.0001$, data are mean ± SEM, n=4 wells, 18-36 measurements each. Adapted from (61).

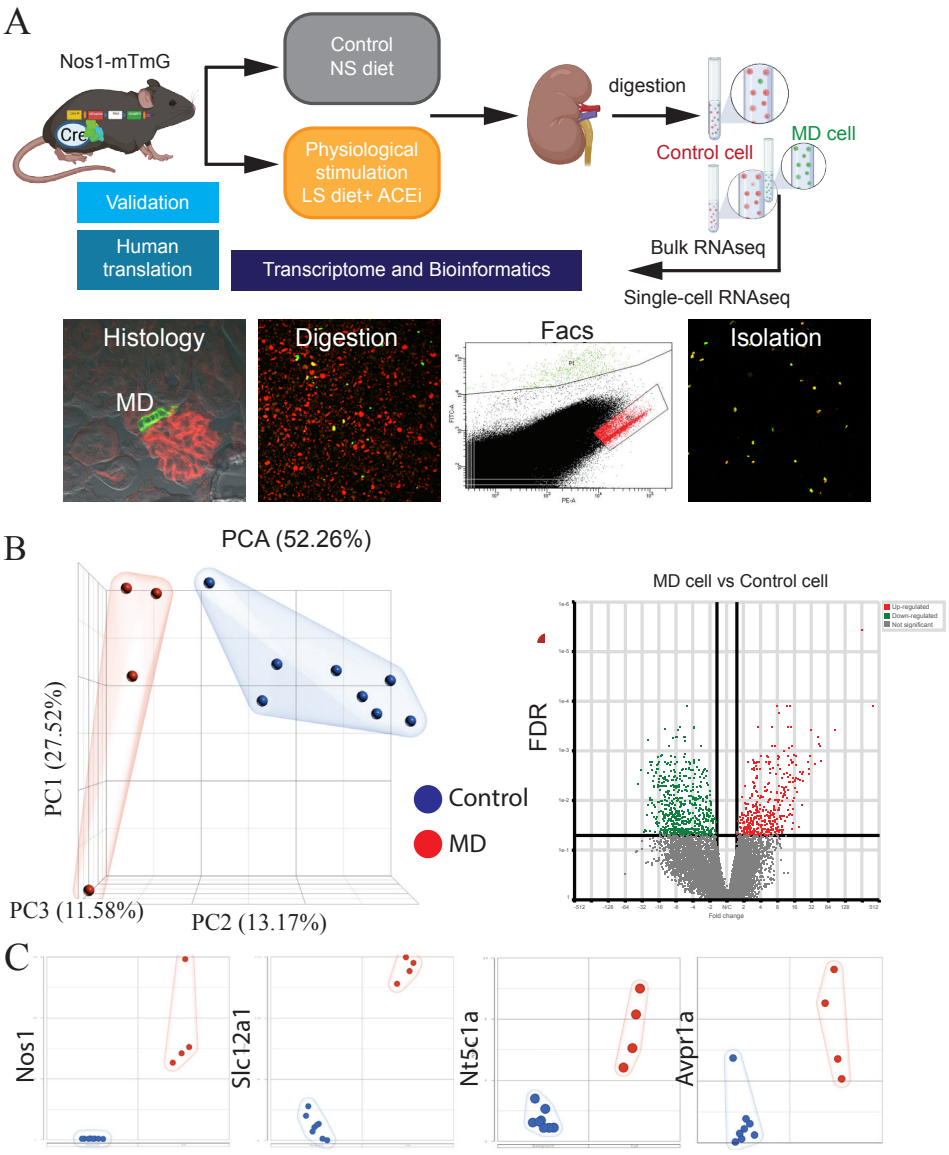

Figure 6. A: Workflow of the MD cell transcriptome analysis. MD (green) and control (red) cells were freshly harvested and digested into single cell suspension from MD-GFP mouse kidneys. Cells were analyzed and sorted based on their fluorescence protein expression (GFP for MD, tdTomato for control cells) followed by bulk or single cell RNA isolation and sequencing. **B:** Main features of the MD cell transcriptome. Left: 3D principal component analysis (PCA) showing clustering of the MD cell versus control cell transcriptome (n=4 MD and n=8 control cell samples). Right: Volcano-plot of up-regulated (red) and down-regulated genes (green) in MD vs control cells based on values of false discovery rate (FDR). Note the higher number of down-regulated compared to up-regulated genes. **C:** Validation of the specificity of MD cell-derived transcriptome showing the high-level expression of classic MD-specific genes in all four MD samples, including Nos1, Slc12a1, Nt5c1a, and Avpr1a. Adapted from (61).

4.2 Neuron-like features of MD cell structure and function

4.2.1 A new view of MD cell microanatomy

The new fluorescence imaging techniques and genetic mouse models described above allowed the visualization of MD cells with high spatial resolution, including MD cell membrane structures, such as the primary cilia at the MD cells' apical membrane. Importantly, the combination of membrane-targeted fluorescence reporter expression with the sporadic labeling of single MD cells enabled the visualization of the microanatomical details of MD cells and depicted an elaborate network of major and minor processes at the cell base, projecting toward the glomerulus and other MD cells (Fig. 7 A-F). We named these structures maculapodia, based on their foot-like projections from the MD cell body at their basal region (36). To characterize the size of the cell processes network at the MD cell basal region, morphological analysis was performed first on fixed kidney sections to measure the length of major processes. Major processes were defined as a few primary (projecting directly from the cell body, 1-3 on average) and thick (>0.5-1.0 μm) cytoplasmic protrusions from the MD cell basal region. Histological analysis confirmed that most MD cells under all conditions have visible major cell protrusions at their base running in parallel with the tubular side of the basement membrane, or crossing through the fragmented basement membrane towards other MD cells, the extraglomerular mesangium, the AA and EA. In control, the length of major processes was 4.63±0.21 μm on average (n=8 mice) but were occasionally seen to extend up to 14 μm (Figs. 7A-G). Interestingly, we found that female mice had significantly longer major processes (5.68±0.32 μm) as compared to male littermates (3.76±0.22 μm, p=0.001, n=4 each), as shown in Fig. 7A, D, G. Although only superficial cortical nephrons were included in all morphometric analysis, MD cells in inner cortical (juxtamedullary) nephrons appeared to have similar features (Fig. 7H).

Since tubular salt sensing and paracrine signaling to the JGA are well-known traditional functions of MD cells, we next applied various dietary salt intake manipulations to address the physiological regulation of MD cell microanatomy at the basal region. As shown in representative images and morphological analysis in Fig. 7A-F and G, the stimulation of MD cell salt sensing activity by combined low-salt diet and ACE inhibition resulted in the development of a more elaborate maculapodia network in male mice, with a significant increase in the length of major processes (5.01±0.34 μm,

p=0.002; n=4) (Fig. 7 B, G). In contrast, high dietary sodium intake led to significant decrease in the length of these structures in both male and female mice (1.94±0.22 µm in male, and 3.88±0.36 µm in female mice, p=0.01; n=4-5) (Fig. 7C, G). Furthermore, we found that the gender difference in the length of major processes was preserved in the condition of high dietary salt intake, while the gender difference disappeared under combined low-salt diet and ACE inhibition conditions due to significant changes in male but not in female mice (Fig. 7G).

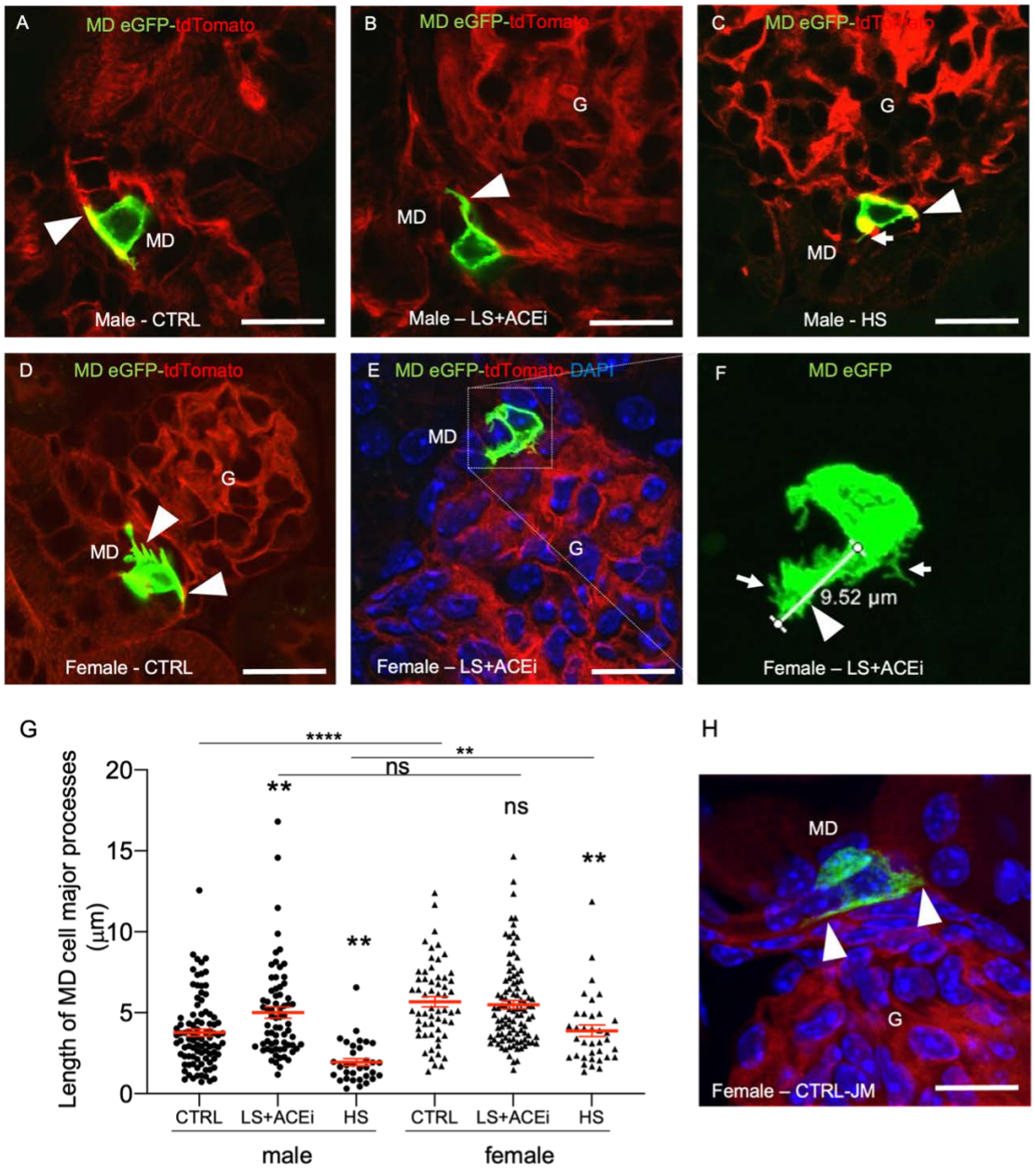

Figure 7. A-E: Native fluorescence images of MD plaques from MD-GFP kidney frozen sections with single, eGFP-labeled MD cells and the adjacent glomerulus. Note the increased length of major cell processes (arrowheads) compared to control (A) in conditions of low-salt diet with ACE inhibition (B), but the much shorter length of these structures in high-salt diet (C). Occasionally, the primary cilium of MD cells was visible at the apical membrane (C, arrow). Compared to kidney tissue from male mice (A-C), MD cell major processes were more elaborate in female mice (D-F). **F**: High magnification maximum projection image of a z-stack series of optical sections showing a maculapodia network consisting of major (arrowhead) and minor processes (arrows) in a single MD cell (same area magnified as shown in panel E). **G**: Statistical summary showing the alterations in the length of MD cell major processes based on gender and in response to various dietary salt intake conditions (33-100 total data points in each group, n=4 in all groups except n=5 in female low-salt diet with ACE inhibition). **: P<0.01, ns=not significant compared to control in same gender group. Comparisons between male and female genders of same salt diet groups are shown by bars. ****: P<0.0001. G: glomerulus, MD: macula densa, CTRL: control, LS+ACEi: low-salt diet with ACE inhibition, HS: high-salt diet. H: Representative image of eGFP-labeled MD cells from a deep juxtamedullary (JM) nephron. Note the presence of major cell processes (arrowheads) similarly to MD cells from superficial cortical nephrons (A-F). Bars are 20 μm. Adapted from (36).

To confirm the presence of MD cell major and minor processes in the intact living kidney tissue, low-salt diet and ACE inhibitor treated MD-GFP mice were used due to the presence of a more elaborate maculapodia network in this condition. We first performed multiphoton microscopy (MPM) of intact MD-GFP kidneys *in vivo*. Although motion artifacts due to vital functions made the visualization of minor processes difficult, several major MD cell processes were clearly observed projecting from the MD base into the extraglomerular mesangium and towards glomerular arterioles (Fig. 8A). In another approach of imaging intact living tissue, we next used the freshly dissected and *in vitro* microperfused JGA preparation from MD-GFP mice after partial tamoxifen induction. In contrast to the *in vivo* model, this was a perfectly steady preparation. Accordingly, both major (0.5-1.0 μm thick and up to 34 μm long) and much thinner, hair-like minor MD cell basal processes were clearly observed forming a dense maculapodia network between individual MD cells and between MD and other JGA cells (Fig. 8B). Minor processes were seen originating from either the cell body or major processes (Fig. 8B).

Quantitative visualization of structural and dynamic features of MD cell minor processes were performed using freshly isolated ex vivo single MD cells. Minor processes were defined as long, very thin (<0.5 μm) hairlike cell processes projecting from either the cell body or major processes. High resolution MPM imaging of single living MD cells depicted a dense network of long, thin, hairlike minor processes (36). Furthermore, the number of minor processes / cells showed similar gender and physiological status-based regulation, female mice and MD cells stimulated using low salt condition exhibiting significantly higher number of minor processes / MD cell compared to male mice or

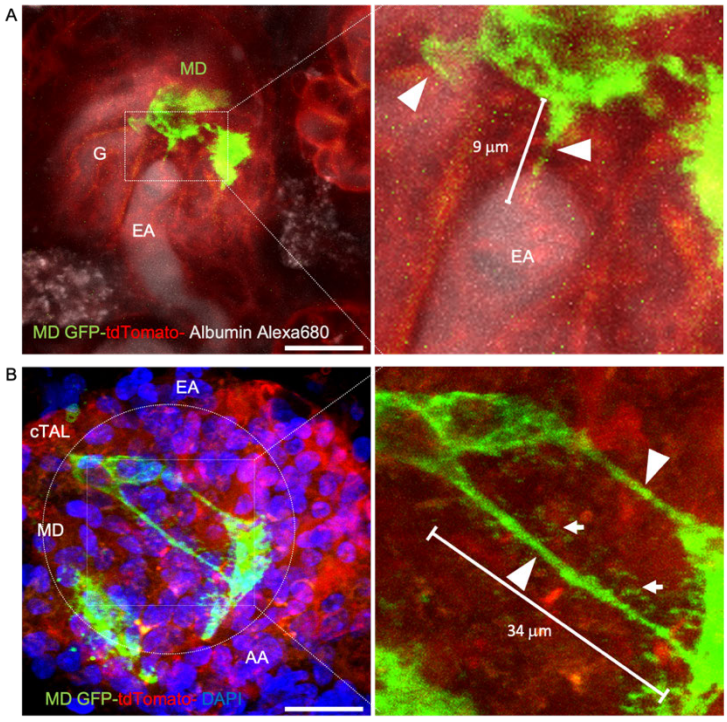

Figure 8. A-B: Representative MPM z-stack projection images of a low-salt diet and ACE inhibitor treated MD-GFP mouse kidney *in vivo* (A) and in the freshly isolated and *in vitro* microperfused JGA preparation (B). Note the MD cell-specific eGFP expression (green) and tdTomato expression in all other kidney cell types (red). Plasma was labeled by Albumin-Alexa Fluor 680 (grey) in panel A. Nuclei are labeled with DAPI (blue) in panel B. The MD areas are magnified in both panels as indicated with labeling of MD cell major (arrowheads) and minor processes (arrows). Dashed circle represents the border of MD plaque. G: glomerulus, MD: macula densa, cTAL: cortical thick ascending limb, EA: efferent arteriole, AA: afferent arteriole. Bars are 20 µm. Adapted from (36).

control condition respectively (36). The expression of membrane-targeted eGFP in MD-GFP mice, and the MPM imaging approach enabled the high temporal and spatial resolution imaging of both plasma and intracellular membranes. Time-lapse imaging of single MD cells and their minor processes revealed the highly dynamic features of these long cell processes, such as their outgrowth or shortening in a few seconds. In addition, multiple cytoplasmic vesicles were visible within minor processes and appeared rapidly moving in both directions between the cell body and their tip, suggesting their role in MD cell endocytosis and secretory functions. Immunostaining of Pregnancy-Associated Plasma Protein A2 (PAPPA2), a known secreted protease that has been used recently as a specific MD-distal tubule marker (65, 66), confirmed the high level of expression of PAPPA2 in MD cells in a vesicular pattern within the cell body as well as at basal cell regions in the human kidney and within the cell processes of mouse MD cells (36).

To visualize the three-dimensional structural features of mouse MD cells' basal region, MPM optical slicing was performed on immunofluorescence labeled whole kidney tissues of MD-GFP mice that were optically cleared using BABB CLARITY. Specifically, our focus was the features of the basal cell region and orientation, relative to the adjacent glomerulus, extraglomerular mesangium, the AA and EA. High-resolution optical slices clearly depicted the intercellular network of MD cell basal major and minor

processes as shown in Fig. 9A-C. The reconstruction of MD cell basal cell membrane features in 3D confirmed the presence of cell-to-cell contacts between individual MD cells via major and minor processes within the same MD plaque (Fig. 9A, C). In addition, MD cell major and minor processes were detected projecting into the extraglomerular mesangium at the glomerular vascular pole, and closely wrapping around individual cells of the AA and EA (Fig. 9 A, C). To study the 3D spatial relation of MD cell processes and renin cells in the JGA, double labeling of MD cells and JG renin cells was performed on thick frozen sections of MD-GFP mouse kidney tissue. High spatial resolution Z-stack projection images were generated by using 3D surface rendering model. The results shown in Fig. 8 C further confirmed the presence of a dense network of MD cell minor processes extending up to 30 µm long towards the individual cells of the AA, EA, and the surrounding EGM. Target cells that MD cells were contacting via the major and minor processes included, but were not limited to, JG renin cells of the AA and EA (Fig. 9C).

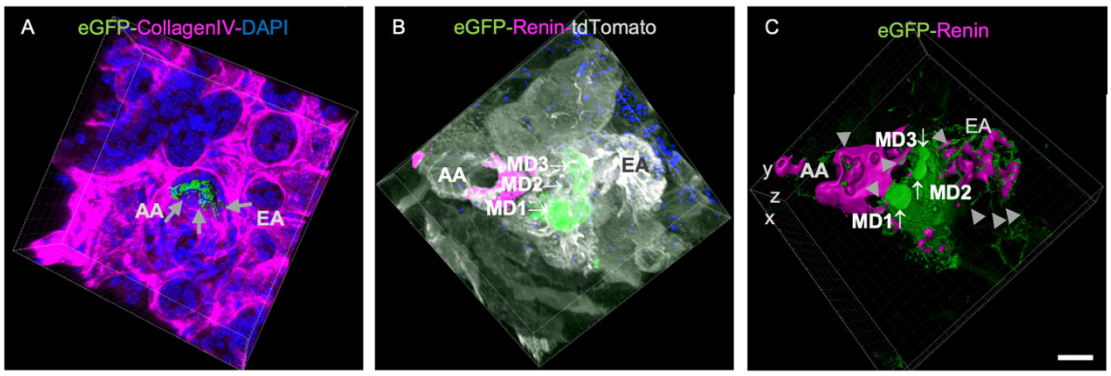

Figure 9. Reconstruction of a MD plaque and the adjacent glomerulus, afferent (AA), and efferent (EA) arterioles in 3D from a female MD-GFP mouse receiving low salt diet and ACE inhibition. **A:** Whole-mount immunofluorescence labeling of optically cleared mouse kidney tissue using CLARITY. MD cells were identified with GFP labeling (green), and the basement membrane was labeled with collagen IV immunostaining (magenta). Cell nuclei were labeled with DAPI (blue). 3D surface rendering revealed the network of MD cell basal major and minor processes running towards the EGM, the AA and the EA (arrows). **B-C:** Immunofluorescence labeling and optical sectioning of 20µm thick frozen sections of MD-GFP mouse kidney. Three MD cells (MD1-3) were labeled by the endogenous, membrane targeted eGFP (green), and juxtaglomerular renin cells were visualized by renin immunolabeling (magenta). Z-stack maximum intensity projection image of the vascular pole of a glomerulus including the AA and EA, and in-between the MD (B). **C:** 3D reconstruction with surface rendering analysis of the same xyz image as shown in panel B. The smooth eGFP+ areas are the 3 MD cells' apical surfaces (arrows). Surface rendering model enabled the visualization of the fine details of the dense MD cell basal processes network and the anatomical orientation of the basal cell major and minor processes of MD cells (arrowheads) relative to the EGM, AA and EA. Note the dense network of MD cell minor processes and their long extensions (up to 30µm) projecting towards renin-labeled (magenta) individual cells of the AA and EA, as well as towards renin-negative cells of the EGM. Bar is 10 µm for all panels. Adapted from (36).

4.2.2 Interoceptive neuron-like functions of MD cells *in vivo*

The expression of neuronal type nitric oxide synthase (nNOS/NOS1) specifically in MD cells has long been established (20). Recent preliminary transcriptomic analysis of a limited number of single MD cells (32) and the microanatomical discovery of long, axon-like MD cell processes (36) suggested MD cell neuronal differentiation. We next asked whether high signaling activity based on calcium signaling can be used as a clue to identify neuron-like chief cell type(s). First, Sox2-GT mice combined with *in vivo* MPM imaging were used to study calcium signaling in all renal cell types. Time-lapse intravital MPM imaging of Sox2-GT mice found robust, spontaneous Ca^{2+} transients in MD cells (Fig. 10A). Among all cells at the glomerular vascular pole including the highly contractile vascular smooth muscle cells of the glomerular arterioles, MD cells showed by far the highest cumulative elevations in Ca^{2+} (Fig. 10A). MD cell Ca^{2+} signals did not conduct to adjacent contractile vascular cells as evident from the significantly different frequency of calcium transients between different cell types (61). In addition, the robust MD cell Ca^{2+} transients were autonomous (preserved in freshly isolated single MD cells) (61) and unique to MD cells in the renal cortex (based on comparison to other renal tubule epithelial cells including proximal and distal tubule epithelial cells (Fig. 10A). Intravital MPM imaging of the entire MD plaque (formed by ~25 individual MD cells) in horizontal optical sections (in mc4DP mode) revealed considerable cellular heterogeneity, with individual MD cells featuring either low, medium, or high Ca^{2+} activity (Fig. 10B, (61)). Several, but not all MD cells in multiple plaque regions showed rapidly and laterally propagating Ca^{2+} responses, further suggesting the heterogeneity of cell-to-cell communication and coordination between individual MD cells. Interestingly, the whole-MD Ca^{2+} readout showed clustering of the single-cell Ca^{2+} transients and their regular oscillations over time (Fig. 10B). Importantly, the whole-MD Ca^{2+} oscillations were simultaneous with the rhythmic changes in the diameter of the adjacent glomerular afferent arteriole (AA), with the peak MD Ca^{2+} phase-matching the peak AA diameter (vasodilatations) (Fig. 10B). Cumulative single-cell Ca^{2+} elevations and firing frequency showed normal distribution (61). To study the spatial and dynamic details of MD cell Ca^{2+} responses with truly single-cell resolution (in sc4DP mode), MD-GT mice were used. Consistent with the microanatomical findings in the MD-GFP mouse model, MD-

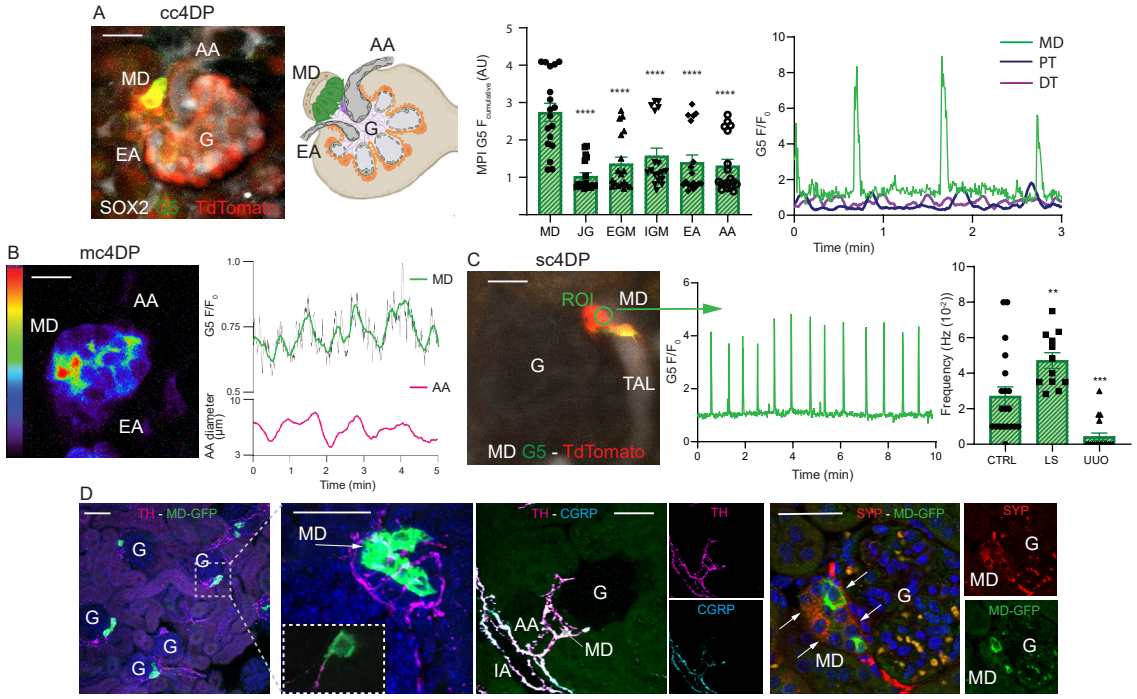

Figure 10. A: Intravital imaging of macula densa (MD) cell calcium in the intact renal cortex. Comparative cell 4D physiology (cc4DP) mode using Sox2-GT mice. Left: Representative maximum projection image (MPI) of a 2-min time-lapse recording of the Ca^{2+} activity of MD and other renal cell types. Note the highest cumulative Ca^{2+} elevations in MD cells (green cells in the attached anatomical drawing of the same glomerulus). Center: Comparison of GCaMP5 fluorescence intensities ($F_{cumulative}$) in single MD, juxtaglomerular (JG) renin, extra (EGM) and intra-glomerular (IGM) mesangial cells, and afferent (AA) and efferent arteriole (EA) vascular smooth muscle cells. Right: Representative recordings of GCaMP5 fluorescence intensity normalized to baseline (F/F_0) in MD (green), proximal tubule (PT, blue), and distal tubule (DT, purple) cells in Sox2-GT mice. ****p<0.0001 vs MD, data are mean ± SEM, n=15-20 cells from n=4 mice. **B:** Multi-cell 4D physiology (mc4DP) mode using Sox2-GT mice. Left: Representative intensity-based pseudocolor MPI image of a horizontal optical section of a whole-MD. Note the heterogeneity of GCaMP5 fluorescence between individual MD cells. Right: Representative simultaneous recording of changes in whole-MD GCaMP5 signal (green) and the adjacent AA diameter (magenta) over time. **C:** Single-cell 4D physiology (sc4DP) mode using MD-GT mice. Left: High-power view of a single glomerulus and MD at the end of the thick ascending limb (TAL) tubule segment (tubule fluid in greyscale). Note the long, axon-like basal cell processes of MD cells. Center: Representative recording of regular Ca^{2+} firing in a single MD cell. Note the 4-fold elevations in cell Ca^{2+} compared to baseline during Ca^{2+} transients. Bar is 20 µm. Right: MD cell Ca^{2+} firing frequency in control and in response to low-salt diet (LS) and unilateral ureter obstruction (UUO). **: p<0.01, ***p<0.001, data are mean ± SEM, n=1-4 cells from n=5 mice. **D:** Tissue 3D volume projection images from optically cleared whole-mount MD-GFP kidneys immunolabeled for endogenous MD-specific GFP expression (green). Left: Tyrosin-hydroxylase (TH) co-labeling (magenta) identifies sympathetic nerve terminals. Magnified area as shown illustrates the close anatomical contact between sympathetic nerve endings and the tip of MD cell basal processes. Center: Co-labeling for TH (magenta) and calcitonin gene-related peptide (CGRP, cyan) that illuminates renal sensory nerves. Overlay and individual TH and CGRP channels are shown separately. Right: Co-labeling for synaptophysin (SYP, red) illuminates the MD (arrows) and the adjacent renal nerve endings (intense red areas). Overlay and individual SYP and MD-GFP channels are shown separately. Bars are 50 µm. Adapted from (61).

GT expression illuminated the long, axon-like (Fig. 10C), or multiple shorter basal cell processes of MD cells (61). Importantly, truly single-cell Ca^{2+} imaging revealed the

presence of subcellular, micro-domain Ca^{2+} transients in both the MD cell somata and processes preceding the global Ca^{2+} spike. A few MD cells showed pacemaker-like regular Ca^{2+} oscillations with the plateau showing ~4-fold elevations in baseline Ca^{2+} and an average frequency of 0.03/s (Fig. 10C). The average duration of single Ca^{2+}spikes (full width at half maximum) was ~2s. Acute iv administration of several classic neurotransmitters in MD-GT mice, including the ß-agonist isoproterenol, the neuroexcitatory glutamate and neuroinhibitory GABA caused immediate, significant alterations in MD cell Ca^{2+} signaling (61). In addition, MD cells responded to several diverse stimuli with altered steady-state Ca^{2+} and/or firing frequency, including most importantly altered tubular fluid composition (low salt diet) and mechanical strain (tubule flow) (Fig. 10C), but also local autacoids (angiotensin II), systemic neurohormone administration (arginine-vasopressin (AVP), gastrin), and metabolic states (diabetic hyperglycemia) (61). Tissue volume rendering in 3D was performed from z-sections of optically cleared whole-mount MD-GFP kidneys immunolabeled for endogenous MD-specific GFP expression, and tyrosin-hydroxylase (TH) or calcitonin gene-related peptide (CGRP), markers of sympathetic or sensory nerves, respectively (Fig. 10D). There was close anatomical association between MD cell basal processes and the sympathetic and sensory nerve endings (Fig. 10D). In addition, the local expression of synaptophysin, a major synaptic vesicle protein specifically in MD cells and in nearby nerve endings (Fig. 10D) suggest that MD cells synapse with each other and with the sympathetic and sensory nerves forming a peripheral renal nervous system.

4.2.3 Neuron-specific molecular signature of MD cells

To understand the characteristics of MD cell molecular signature we performed an unbiased tissue specificity analysis of the MD cell gene profile applying TissueEnrich, a recently developed online available tissue-specific gene enrichment analytic tool (61, 67). Using the top 50 highest enriched MD-specific genes as an input gene set, TissueEnrich assigned a highly significant brain tissue identity to MD cells (Fig. 11A). The enrichment of MD-specific genes was highest in the cortex, cerebellum, developing brain, and the olfactory bulb, while kidney-specificity was ranked at only 4 among all organs studied (Fig. 11A). As an alternative method, analysis by the GTEx Multi Gene Query platform of same MD gene set confirmed brain tissue specificity of the MD gene

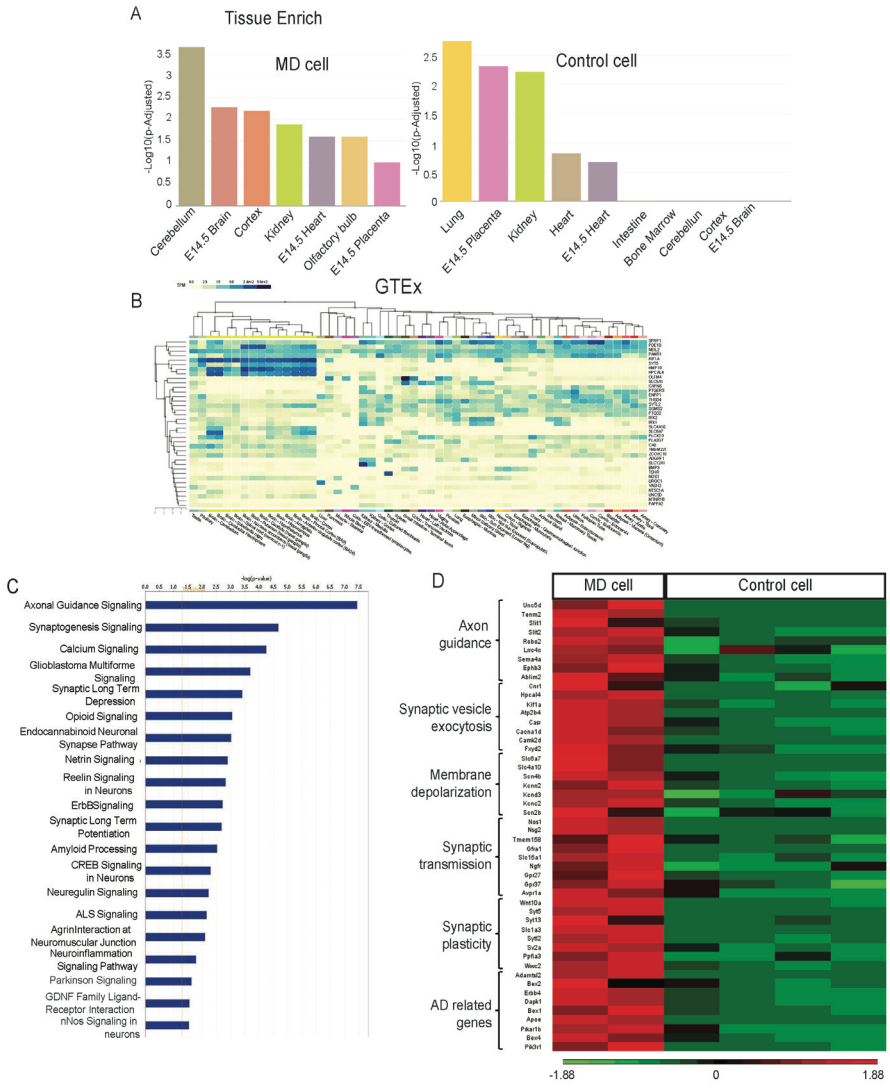

Figure 11. A: Tissue specificity analysis of the MD (left) and control cell (right) transcriptome. Bar chart showing the enrichment (-Log10(P-Adjusted)) of the top 50 highest expressed MD cell-specific genes in various tissues using TissueEnrich and the Mouse ENCODE dataset for comparison. **B**: Heat map of the expression of the same top MD cell gene set in various tissues using GTEx Multi Gene Query. **C:** Transcriptome analysis showing the most significant MD-specific canonical pathways as listed based on IPA analysis. **D:** The expression of neuronal genes in MD cells. Heat map of the MD (red) vs. control renal cell (green) expression of the top 50 neuron-specific MD cell enriched genes in 6 GO term categories as indicated based on Partek Flow analysis (n=2 MD and n=4 control). Adapted from (61).

profile (Fig. 11B). In contrast, TissueEnrich analysis of the transcriptome of control kidney cells showed high ranking of kidney specificity and no expression in brain (Fig. 11A) (61).

To gain detailed molecular insights of the neuron-like MD gene profile, we first performed canonical pathway analysis using IPA (Fig. 11C). Axon guidance was the most

significant pathway, with the high ranking of several other neuron-specific mechanisms. Using Gene Ontology (GO) terms that best describe biological processes in neurons as suggested by MD Gene Set Enrichment analysis (Partek Flow), we then selected 7-9 from the top 300 MD-enriched genes into each of the following categories: axon guidance (GO: 0008040), induction of synaptic vesicle exocytosis by positive regulation of presynaptic cytosolic calcium ion concentration (GO: 0099703), membrane depolarization (GO: 0051899), positive regulation of synaptic transmission (GO: 0050806), regulation of neuronal synaptic plasticity (GO: 0048168), and several genes related to neurodegenerative diseases including Alzheimer's disease (AD). A heat map of these top 50 neuron-specific enriched genes was generated to illustrate their higher and MD-specific expression in MD vs control renal cells (Fig. 11 B). The top up-regulated neuron-specific MD genes included previously established MD cell markers (*Nos1, CaSR, Atp2b4, Fxyd2*) as well as new ones (*Unc5d, Tenm2, Hpcal4, Slc6a7, Nsg2, Ngfr, Syt5, Bex1, Dapk1, Apoe*). The highly MD-specific expression of a selection of these genes was validated and translated to the human kidney on the protein level (61).

We next performed single-cell RNA sequencing and transcriptome analysis of individual MD cells harvested from a single MD-GFP mouse to gain additional molecular-level knowledge of the heterogeneity of MD cell biology (GEO accession number GSE189954 for transcriptome data from n=4 different mice). After performing quality control of the initial database, 17,000 genes were detected across 894 MD cells. Unsupervised graph-based clustering and UMAP visualization using Partek Flow revealed five subtypes of MD cells (MD1-5, Fig. 12A). These MD clusters were annotated using a hybrid approach that combined the top enriched genes for each cluster (Fig. 12B-D), classic MD markers (e.g. *Nos1*), cluster-specific canonical pathways based on IPA analysis of the differentially expressed genes (Fig. 12C), and their relevance to the functional sc4DP-based Ca^{2+} signaling results (Fig. 10). The MD1 (high *Itpr1* and *Nfatc2*) and MD3 (high *Pvalb*, *Calb1* and *Grin2c*, glutamatergic signaling) clusters (Fig. 12A-D) likely represent the high Ca^{2+} signaling activity hub and leader (pacemaker) cells that were identified in the *in vivo* sc4DP functional approach (Fig. 10A). The MD2 cluster (high *Gabrr2* and *Begain*) features high GABAergic signaling and synaptic activity and transmission (Fig. 12A-D) that matches the *in vivo* functional activity of non-connected "lone" cells (61). The MD4 cluster (high *Apoe*) features the highest expression of genes

(*Dscam*, *Axdnd1*) that participate in neuronal cell processes formation, arborization and neurite outgrowth that is consistent with a subset of MD cells having axon-like long basal cell processes (maculapodia) (36). The MD5 cluster (high *Nos1*) has the highest expression of the classic MD cell marker *Nos1* and may participate in cell motility, phenotypic transformation and inflammation (Fig. 12A-D). All MD cells showed high expression of classic MD cell markers (*Nos1*, *Pappa2*, *Slc12a1*, *Kcnj1*, *Casr,* Figs. 12B-E), the newly identified glucagon receptor (*Gcgr*), and a neuron-like gene profile including some of the major AD risk genes (*App*, *Mapt*, *Bace1, Apoe,* Fig. 12D-E). The heterogenous, highly MD-specific expression of a selection of these genes was validated and translated to the human kidney on the protein level (Fig. 12F). The high *NOS1*$^{+}$ cells are consistent with cluster MD5, *BDNF*$^{+}$ cells with MD1-2, *PVALB*$^{+}$ and *ATP2A3*$^{+}$ cells with MD3, *SEMA3F*$^{+}$ with MD4 (Fig. 12F). *CPS1*$^{+}$ and *SAT1*$^{+}$ cells that may synthesize GABA from putrescine via an alternative enzymatic pathway (68) may be consistent with MD2 (Fig. 12F). The high level and MD specificity of *FOS* expression is consistent with neuron-like activity, because it is often expressed when neurons fire action potentials (69). The high MD expression of neurohormone and metabolic receptors such as the AVP (Avpr1a), gastrin and cholecystokinin (Cckbr) and glucagon receptor (Gcgr) further highlight the systemic sensory function of MD cells to maintain whole body homeostasis and their role in inter-organ crosstalk.

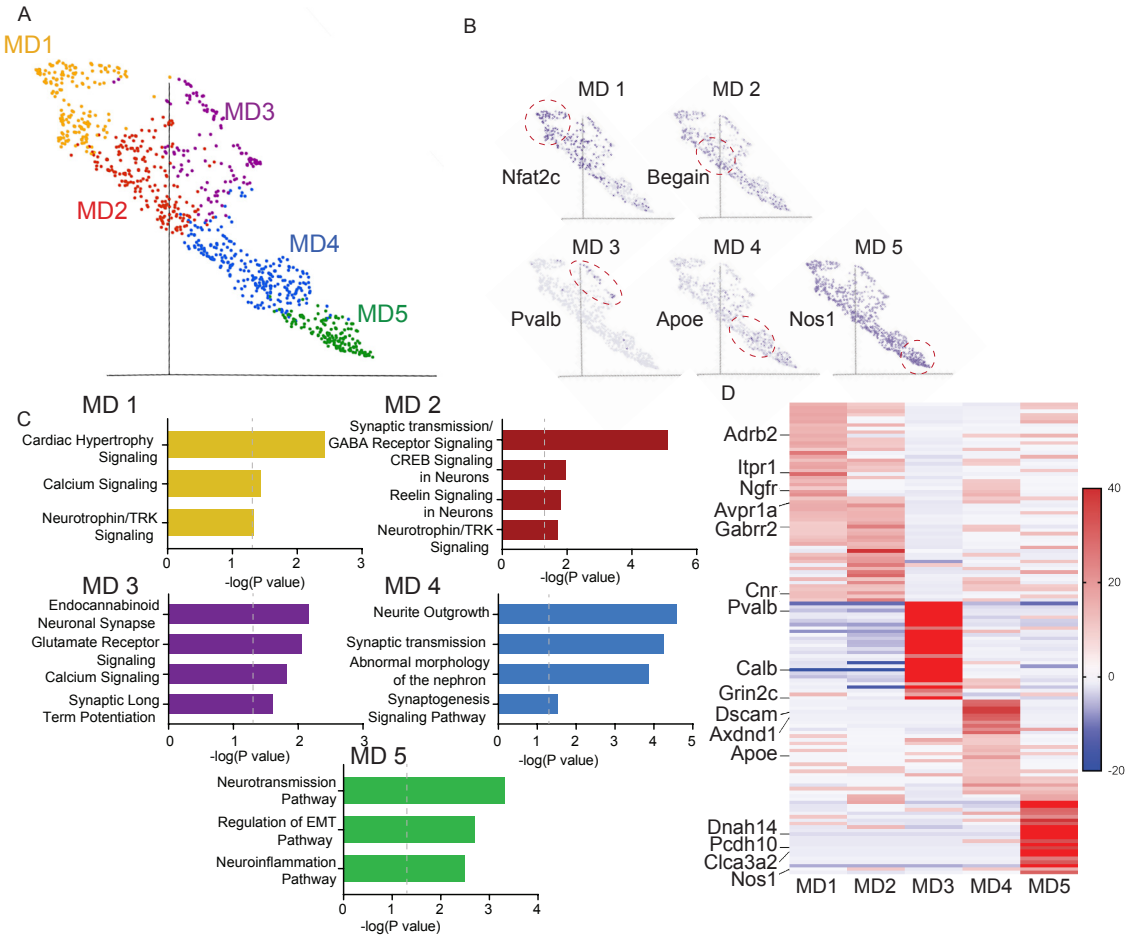

Figure 12. A: UMAP visualization of integrated single-cell transcriptomic analysis of MD cells (n = 2500). Five cell clusters (MD1-5) were identified based on graph-based analysis in Partek Flow. **B:** Cluster-specific expression of top enriched identifier genes. These include Nuclear Factor of Activated T Cells 2 (Nfatc2), Brain Enriched Guanylate Kinase Associated (Begain), Parvalbumin (Pvalb), Apolipoprotein E (Apoe), Nitric Oxide Synthase 1 (Nos1). **C:** Canonical pathway analysis (based on IPA) showing enriched biological processes specific for clusters MD1-5. **D:** Heat map of the top 25 enriched genes in each MD cluster (MD1-5). Cluster-specific genes include Adrenoceptor Beta 2 (Adrb2), Inositol 1,4,5-Trisphosphate Receptor Type 1 (Itpr1), Nerve Growth Factor Receptor (Ngfr), Arginine Vasopressin Receptor 1A (Avpr1a), Gamma-Aminobutyric Acid Type A Receptor Subunit Rho2 (Gabrr2), Cannabinoid Receptor 1 (Cnr), Parvalbumin (Pvalb), Calbindin 1 (Calb), Glutamate Ionotropic Receptor NMDA Type Subunit 2C (Grin2c), DS Cell Adhesion Molecule (Dscam), Axonemal Dynein Light Chain Domain Containing 1 (Axdnd1), Apolipoprotein E (Apoe), Dynein Axonemal Heavy Chain 14 (Dnah14), Protocadherin 10 (Pcdh10), Chloride Channel Accessory 3A2 (Clca3a2), Nitric Oxide Synthase 1 (Nos1). Adapted from (61).

4.3 The role of MD cells in endogenous tissue remodeling and regeneration after injury

4.3.1 The molecular profile of the MD cell program for tissue regeneration

To further understand the true function of MD cells we applied loss of body fluid and salt as the strongest physiological stimuli of MD cells to enhance their physiological function. Interestingly, single-cell transcriptome analysis of activated MD cells identified angiogenesis, cell movement, quantity and migration of cells and migration of vascular endothelial cells as the major biological activities of MD cells (Fig. 13A). Similar to control condition, unsupervised graph-based clustering and UMAP visualization using Partek Flow revealed the same five subtypes of MD cells under physiological activation (LS) condition (MD1-5, Fig. 13B). Certain MD cell clusters showed high expression of specific growth and transcription factors and chemokines (Fabp3, Egf, Ccn1, Foxq1, Cxcl12 for MD3) and angiogenic factors (Vash2, Pamr1, Vegfa, Ccn3 for MD5) in response to MD cell activation, suggesting MD cell heterogeneity regarding their tissue remodeling regulatory functions. In contrast, all MD clusters were similarly enriched in other secreted cytokines, growth and extracellular matrix (ECM) and Wnt signaling factors (Bmp3, Fgf9, Spp1, Wnt10a, Sfrp1, Tcf4) that have well-known roles in controlling progenitor cells and tissue remodeling (Fig. 13C). Bulk RNA-based MD transcriptome analysis further confirmed the MD-specific expression of several angiogenic, cell migration and patterning, growth, ECM remodeling and transcription factors. The expression of these factors was upregulated in physiological activation (LS) condition compared to control (70). The newly identified factors include the Ccn family of matricellular proteins, Ccn1 (Fig. 13B) and Ccn3 (Fig. 13B, ranked #38 highest enriched MD gene). The high-level expression of known MD cell markers including Pappa2, Nos1, Ptges2, Slc12a1 validated the our approach (70). Mass spectrometry analysis of the low-salt conditioned newly established immortalized MD^{geo} cell secretome (MD identified the angiogenic matricellular protein CCN1 as one of the top enriched MD-secreted proteins (Fig. 13E) confirming the transcriptome data (Fig. 13B). MD conditioning by LS resulted in a 6-fold increase in MD cell CCN1 secretion compared to control (Fig. 13E). The highly MD-specific expression of a selection of the newly identified tissue remodeling genes (or their closely related homologs) was validated and translated to the human kidney on the protein level (Fig. 13F).

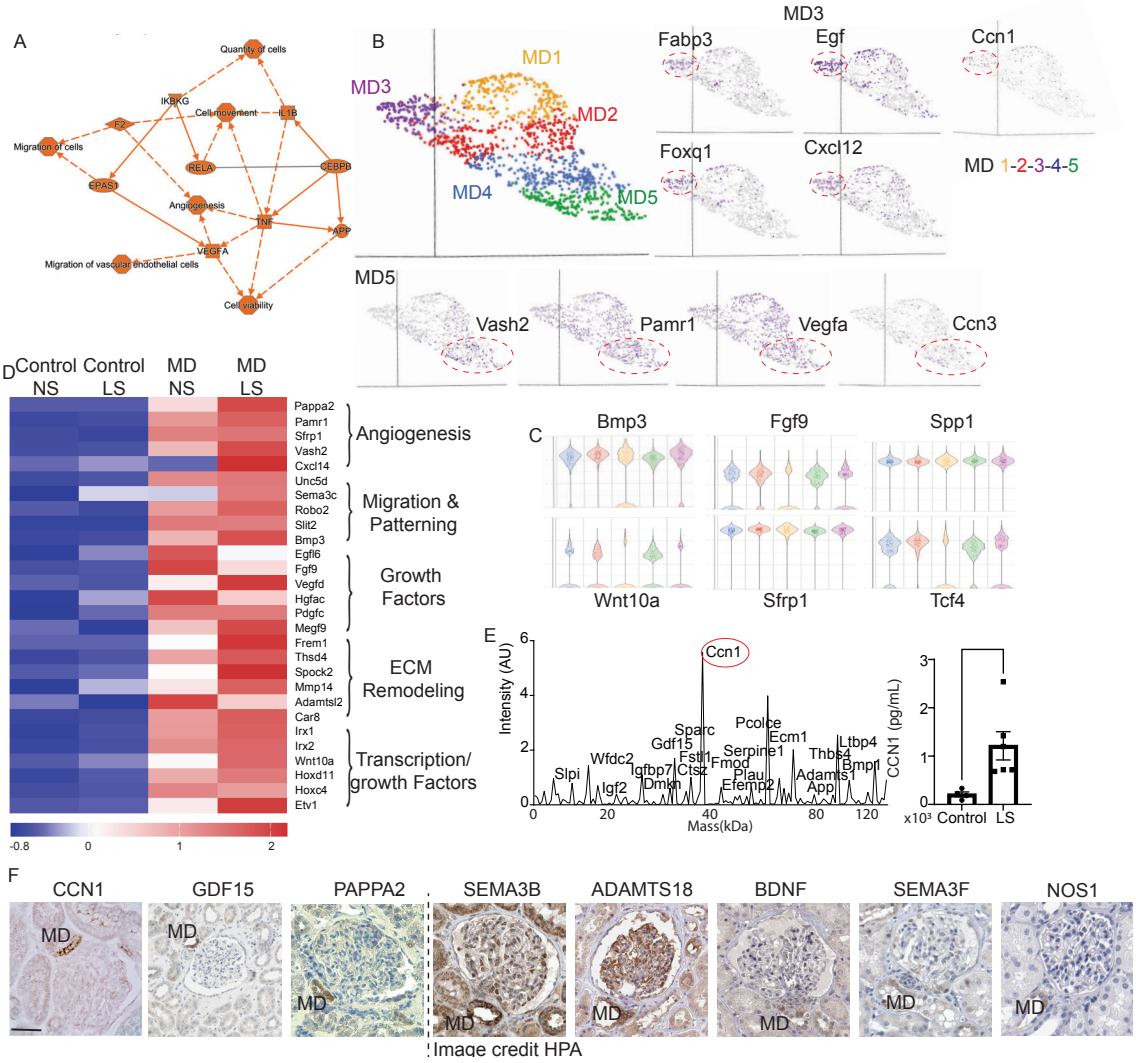

Figure 13. A: Graphical summary of MD single-cell transcriptome analysis. The top activated (indicated by orange, positive z-score) biological activities, pathways and genes are listed based on unbiased IPA analysis. IPA system node shapes and colors are used (octagon: function, square: cytokine, triangle: kinase, ellipse: transcription regulator). **B:** UMAP visualization of integrated single-cell transcriptomic analysis of MD cells (n = 1296 MD cells from single MD-GFP mouse in LS condition). Five cell clusters (MD1-5) were identified based on graph-based analysis in Partek Flow. Cluster-specific expression of top enriched genes in MD3 (Fabp3, Egf, Ccn1, Foxq1, Cxcl12) and MD5 clusters (Vash2, Pamr1, Vegfa, Nov). **C:** Violin plot (bottom) of the expression of highly enriched MD genes in all five clusters (MD1-5). **D**: Heat map of the mean expression of top enriched MD-specific genes in MD vs. control cells and in control (normal salt, NS) and physiological stimulation (LS: low salt+ACEi) conditions based on bulk RNA analysis (n=2 mice for MD and n=4 mice for control cells from each condition). Genes were grouped into five categories as indicated according to their biological function. Scale indicates z-score values. **E:** Mass spectrometry (left) and CCN1 ELISA (right) analysis of the composition of the low salt conditioned MDgeo cell culture medium. The mass spectrum plot is representing the detected MD-derived secreted proteins in the MDgeo cell culture medium as indicated. LS: low-salt diet. *: $p<0.05$, data are mean ± SEM, n=5 each. **F:** Immunohistochemistry validation of the expression of top enriched mouse MD-specific genes or their homologous isoforms in the human kidney. Data are from the Human Protein Atlas if indicated. Scale bar is 50 µm for all panels. Adapted from (70).

4.3.2 Live tracking and MD-centric pattern of endogenous tissue remodeling

To establish the dynamics and pattern of endogenous kidney tissue remodeling with single-cell resolution in the intact living mouse kidney, unbiased tracking of the same tissue volume of kidney cortex over several days and weeks was performed using a combination of serial intravital MPM (41, 71) and genetic cell fate tracking. The applied experimental strategy, conditions, and inducible fluorescent reporter mouse models to genetically label and track various mesenchymal and endothelial cell lineages are summarized in Fig. 14A. In contrast to the lack of effect of pathological injury (ischemia-reperfusion) or time-control (70), the loss of body fluid and salt as a MD-activating physiological stimulus using treatment with low-salt (LS) diet+angiotensin converting enzyme inhibitor enalapril (ACEi) for up to two weeks caused substantial recruitment of mesenchymal and endothelial precursor cells in Ng2-tdTomato and Cdh5-Confetti mice, respectively (Fig. 14B). Importantly, the geometrical epicenter (highest cell density) of both mesenchymal and endothelial cell recruitment was the base of MD cells at the glomerular vascular pole in each nephron (Fig. 14B). Other physiology-based stimuli that are known to trigger MD cell sensing of low salt (the diuretic furosemide, low salt diet or ACEi alone) caused similar, but less robust responses (70). Newly recruited $Ng2^+$ cells differentiated to multiple cell fates including vascular smooth muscle, renin, mesangial, parietal epithelial and proximal tubule cells and podocytes (70). Alternative genetic strategies to track mesenchymal cell lineages (Ren1d-Confetti and Foxd1-tdTomato mice) produced similar results (Fig. 14C). Both $Cdh5^+$ and Ren^+ cells produced clonal remodeling of the vasculature, interstitium and glomerulus closest to the MD (Figs. 14C), further suggesting the presence of mesenchymal and endothelial progenitor cells at the glomerular vascular pole. LS+ACEi-induced $Ng2^+$ and $Cdh5^+$ cell recruitment to the glomerular vascular pole was blocked by pharmacological inhibition of the known MD-specific markers cyclooxygenase-2 (Cox-2) or neuronal nitric oxide synthase (Nos1), suggesting the key role of MD cells in this tissue remodeling process (70). Fate tracking of MD cells for extended periods of time (>6 months) in either control or LS+ACEi stimulation conditions using inducible MD-GFP mice found no GFP-labeled cells outside of the MD area (data not shown), suggesting that MD cells themselves do not migrate out of their classic anatomical location.

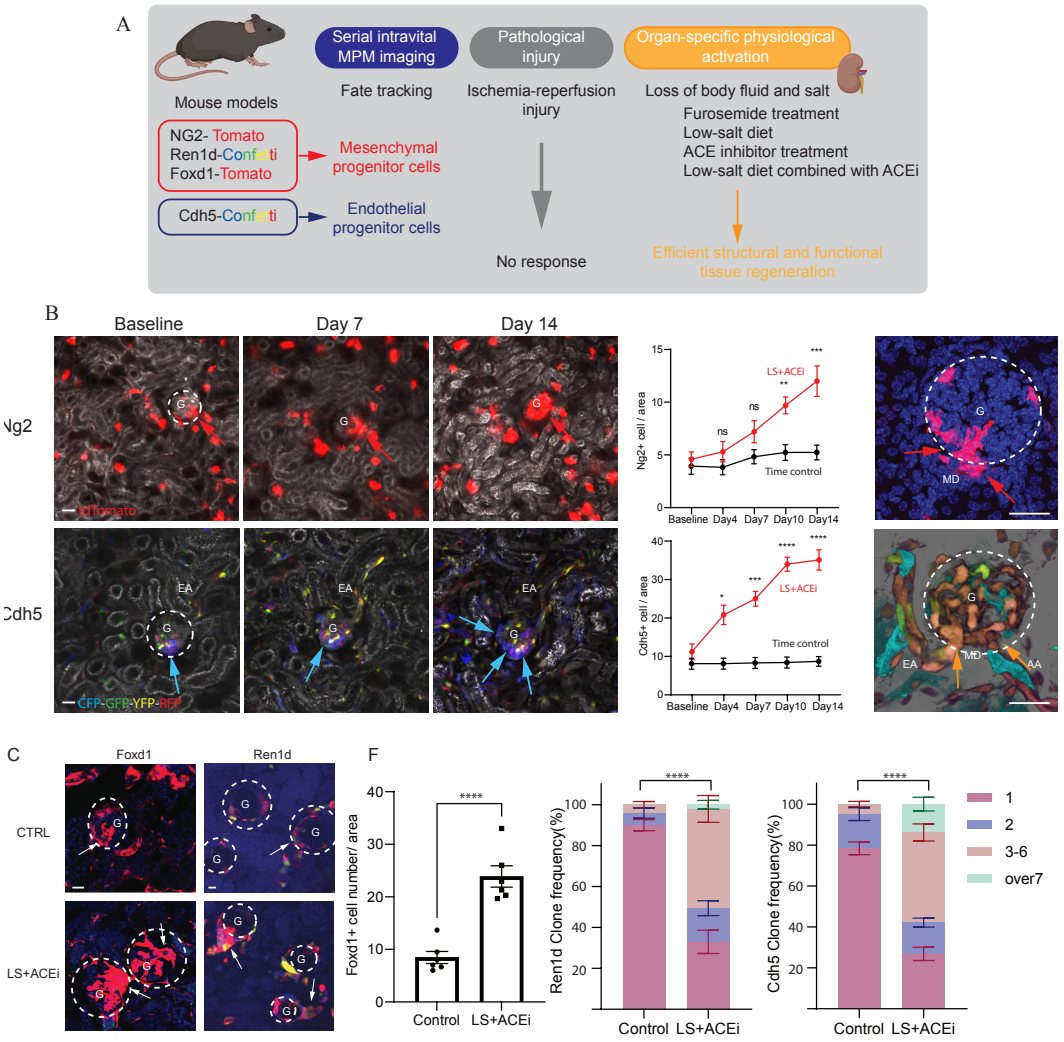

Figure 14. A: Experimental design of studying physiological and pathological activation of endogenous tissue remodeling using serial multiphoton microscopy (MPM) combined with multiple genetic reporter mouse models. **B:** Representative *in vivo* MPM maximum projection images (left) and the number of Ng2+ or Cdh5+ cells per glomerular area (center) of the same kidney cortex area/volume visualized through an abdominal imaging window at the indicated time points or in a magnified single glomerulus (right, on Day14). Responses to low-salt (LS) diet+ACEi (all panels) or timed control (center) are shown. Note the low cell number and random distribution at baseline, but high cell number specifically at the glomerular vascular pole (red and blue arrows) and the Cdh5+ clones (CFP/blue (left) and YFP/RFP orange (right)) among all 10 different CFP/GFP/YFP/RFP Confetti color combinations. Plasma was labeled with Alexa594-Albumin (greyscale). G: glomerulus (dashed white circles), AA/EA: afferent/efferent arteriole, MD: macula densa. **C:** Representative fluorescence images of native tdTomato (red) in Foxd1+ cells (left) or Confetti (CFP/GFP/YFP/RFP multicolor) in Ren1d+ cells (right) in timed control or after LS+ACEi treatment in Foxd1-tdTomato or Ren1d-Confetti mouse kidney sections. Glomerular vascular pole areas under the MD cell base are indicated by arrows in multiple nephrons. Nuclei are labeled blue with DAPI. G: glomerulus. Adapted from (70).

4.3.3 Ngfr signaling is key in MD neuron-like and tissue remodeling functions

The nerve growth factor receptor (*Ngfr*) was the highest expressed growth factor receptor in MD cells (ranked #64 most enriched MD gene, (61)) suggesting the primary role of Ngf signaling via Ngfr in the function of MD cells. Therefore, we next aimed to establish Ngfr signaling as a key molecular mechanism in the neuron-like and tissue remodeling functions of MD cells. Immunofluorescence analysis validated the transcriptome data and confirmed the MD cell-specific expression of the p75NTR Ngfr in the mouse kidney and in MD^{geo} cells, including in the cell membrane (61). Ngfr expression was significantly increased by low salt culturing condition in MD^{geo} cells and supplementation of the MD^{geo} culture media with NGF significantly increased cell proliferation and was absolutely essential for the long-term survival of MD^{geo} cells in culture (61). In addition NGF treatment significantly increased the expression of the classic and functionally key MD cell markers Cox2, Nkcc2, and Nos1 and induced phosphorylation of ERK1/2 MAP kinases, IKB and TrkA-B, but not Akt in a variable time-dependent manner (61).

We next developed mice with MD-specific knockout of Ngfr (MD-NGFR KO) to examine the functional role of MD cell Ngfr signaling *in vivo*. Both immunofluorescence localization and renal cortical tissue immunoblotting validated the successful MD-specific deletion of the p75NTR Ngfr in MD-NGFR KO mice (61). *In vivo* MPM imaging of the newly developed MD-GT-NGFRKO mice revealed that compared to WT mice, the frequency of MD cell Ca^{2+} transients showed a 4-fold increase in MD-NGFR KO mice (Fig. 15A). Importantly, instead of the regular periodic oscillations that were observed in WT mice (Fig. 10B), MD-NGFR KO mice featured irregular chaotic-like oscillations in whole-MD Ca^{2+} (Fig. 15B). A cell-to-cell functional connectivity map (MD connectome) with preserved MD architecture and a heat map were generated based on Pearson's correlation analysis of time-lapse Ca^{2+} recordings between all MD cell pairs in WT and MD-NGFR KO mice (Fig. 15B). Cell-to-cell connectivity of MD cells was greatly reduced in MD-NGFR KO mice compared to WT (Fig. 15B). The connectivity map of WT MD plaque identified three "hub" cells within the whole MD that had the highest number of connections, and one "lone" cell that had zero connections (Fig. 15B). In the MD of MD-NGFR KO kidney, there were only two small "hub" cells within the whole MD, while a great number of "lone" cells were identified which had no connections to

other MD cells (Fig. 15B). The injection of the p75NTR receptor modulator LM11A-31 or recombinant soluble b-amyloid precursor protein alpha (sAPPa) induced significant elevations in MD cell Ca^{2+} (but not in any other renal cell types, not shown) in the WT but not in MD-NGFR KO mice (Fig. 15C). In contrast, NGF produced strong MD cell Ca^{2+} responses not only in WT, but also in MD-NGFR KO mice (Fig. 15C). In addition, MD cells in MD-NGFR KO mice generated significantly reduced Ca^{2+} responses to iv injected gastrin (Fig. 15C). Short-term treatment with NGF (10 µg/kg sc daily for one week) caused significant increases in the number of renin-producing juxtaglomerular (JG) cells and in GFR in WT mice, while renin cell number and GFR were significantly lower in MD-NGFR KO mice (Fig. 15D). In addition, MD-NGFR KO mice featured kidney tissue fibrosis and showed increased levels of the classic neurodegeneration marker p-tau (S199) in MD cells (Fig. 15E). Importantly, the expression of the MD-specific angiogenic and tissue remodeling factors Ccn1, Ccn3 and Cxcl14 was significantly reduced in MD-NGFR KO mice compared to WT (Fig. 15F).

4.3.4 Therapeutic targeting of the MD program for kidney repair

Human translational studies using transcriptomic data from the European Renal cDNA Biobank (ERCB) as well as protein expression data of CKD and control kidney biopsies uncovered that CCN1 is among the top 1% under expressed genes in CKD patients independent of the etiology of the disease (70). To study whether targeting of the presently identified MD cell program for kidney tissue regeneration provides therapeutic benefit, the effects of treatment with MD-derived biologicals were tested in the robust CKD model of Adriamycin (ADR)-induced focal segmental glomerulosclerosis (FSGS) in BalbC mice (Fig. 16A). A single ADR injection induced severe GS pathology after two weeks indicated by reduced GFR and high-level albuminuria (Fig. 16B-C). At this point, treatment of the pre-existing GS was initiated using one of the following five biologicals: saline (PBS), recombinant CCN1 in low or high-dose, control DMEMF12 culture medium or low salt conditioned cell culture medium of the MD^{geo} MD cell line (Fig. 16E). Animals were followed-up for 4 weeks of treatment. Mass spectrometry analysis and CCN1 ELISA of the conditioned MD^{geo} cell culture medium confirmed the secretion of MD cell factors and informed the therapeutic dose of low CCN1 (Fig. 13E), while the high-dose CCN1 was chosen based on previous work in liver (72).

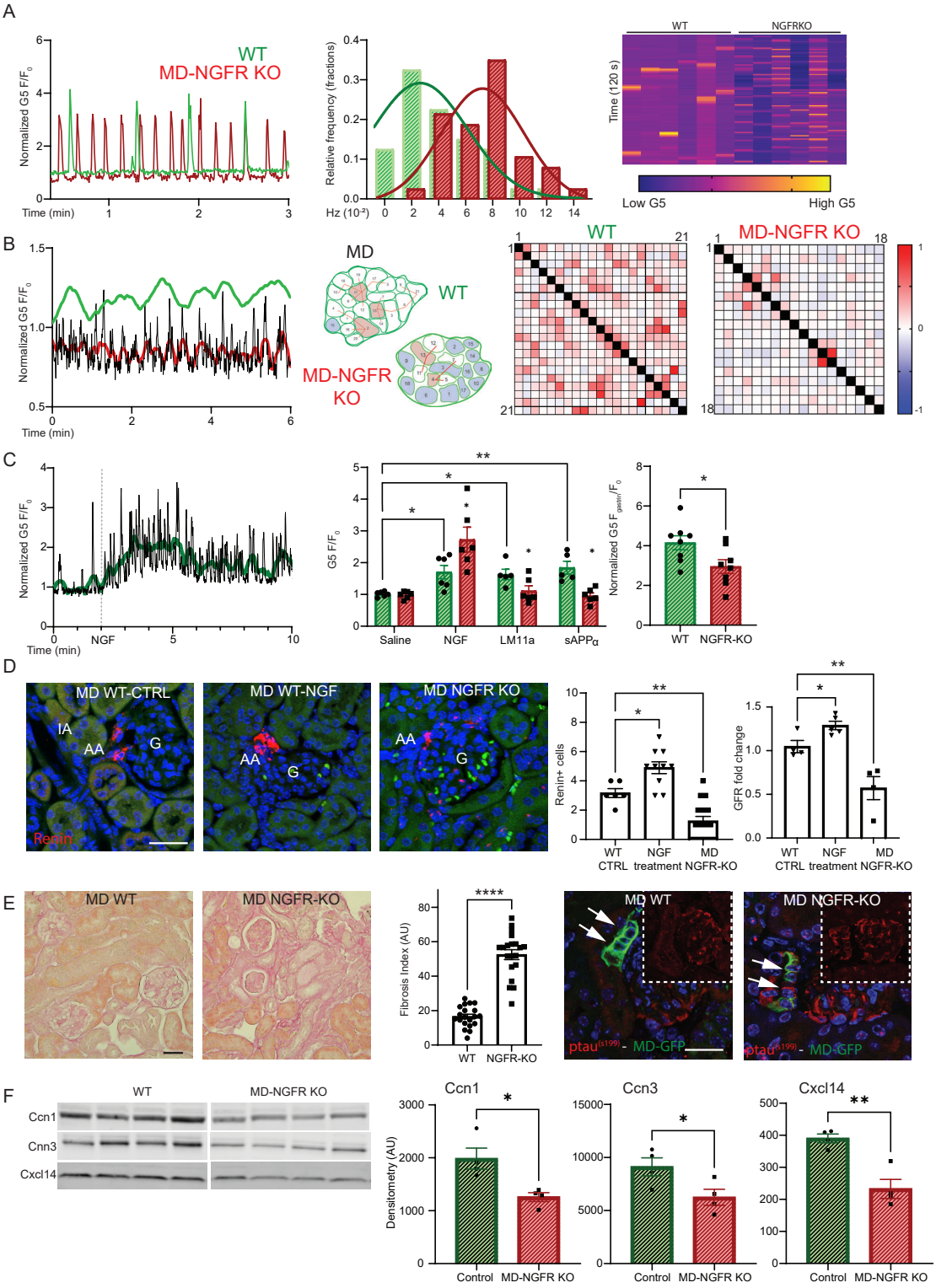
A
WT
MD-NGFR KO
Normalized G5 F/F0
Time (min)
Relative frequency (fractions)
Hz (10-2)
NGFRKO
Time (120 s)
Low G5
High G5
B
MD
WT
MD-NGFR KO
C
NGF
Saline
LM11a
sAPPα
NGFR-KO
D
MD WT-CTRL
MD WT-NGF
MD NGFR KO
IA
AA
G
Renin
Renin+ cells
GFR fold change
WT CTRL
NGF treatment
MD NGFR-KO
E
MD WT
MD NGFR-KO
Fibrosis Index (AU)
ptau(s199) - MD-GFP
F
Ccn1
Cnn3
Cxcl14
Densitometry (AU)
Control
MD-NGFR KO

Figure15. A: Increased frequency of MD Ca^{2+} transients in MD-NGFR KO vs. WT mice. Left: Representative recordings of the regularly oscillating Ca^{2+} transients in a single MD cell from WT (green) and MD-NGFR KO mouse (red). Center: Distribution of single MD cells (shown as fraction of total number of cells with curve fittings) based on their Ca^{2+} firing frequency during 2-min time lapse recordings. Right: Heat map of the changes in GCaMP5 fluorescence intensity (F/F_0) of six individual MD cells from both WT and MD-NGFR KO mice during a 120 s time-lapse. Note the 4-fold increase in Ca^{2+} firing frequency in MD-NGFR KO vs WT. **B:** Reduced connectivity and sensitivity of MD cells in MD-NGFR KO vs WT mice. Left: Representative recordings of changes in whole-MD GCaMP5 signal over time in a WT (green) and a MD-NGFR KO mouse (red). Center: Functional cell-to-cell connectivity map of MD plaques in WT and MD-NGFR KO mice shown in horizontal plane and with all 21 (WT) and 18 (MD-NGFR KO) individually numbered MD cell positions. Red line connecting individual cell pairs indicates that the strength of the cell pair correlation (Pearson's R value) was >0.35. Red/blue cell color indicates hub/lone cells, respectively. Right: Heat-map shows Pearson's coefficient of each cell pair in a two-color gradient (low correlation blue, high correlation red as indicated in scale). **C:** The effects of iv injected exogenous Ngfr ligands on MD cell Ca^{2+} in WT (green) and MD-NGFR KO mice (red). Left: Representative time-lapse recording of the effect of NGF (0.25 ug/g) on the whole-MD calcium (G5 F/F_0) in a WT mouse. Center: Summary of the effects of iv injected NGF (0.25 ug/g), or LM11A-31 (75 ug/g), or sAPPa (0.6 ug/g) on fold-changes in MD cell Ca^{2+} (G5 F_{max}/F_0) in WT (green) vs. MD-NGFR KO mice (red). Right: The effect of iv injected gastrin (5 ug/g) on MD cell Ca^{2+} (G5 F/F_0) in WT (green) vs. MD-NGFR KO mice (red). *: $p<0.05$, **:$p<0.01$ compared to saline control in WT, #: $p<0.05$ WT vs. MD-NGFR KO in the same treatment groups, data are mean ± SEM, n=5 mice each. **D:** Reduced renin expression and GFR in MD-NGFR KO vs WT mice. Left: Representative immunofluorescence images and summary of the effects of NGF treatment for one week (0.25 ug/g/day) on renin (red)-producing JG cell number in WT untreated, WT NGF treated, and MD-NGFR KO mice. Cell nuclei are labeled blue with DAPI, tissue autofluorescence (green) is shown for tissue morphology. Right: Summary of the changes in GFR in untreated WT, WT treated with NGF, and MD-NFGR KO mice. *: $p<0.05$, **: $p<0.01$, data are mean ± SEM, one average shown from n=6-10 mice each. **E:** Tissue fibrotic and MD neurodegenerative features of MD-NGFR KO mice. Left: Representative images of PAS-stained kidney tissue sections and the summary of tissue fibrosis index in WT and MD-NGFR KO mice. ****: $p<0.0001$, data are mean ± SEM, four data points are shown from n=5 mice each. Right: Immunofluorescence images of p-tau expression (red) in MD cells (arrows) of WT and MD-NGFR KO mice. Overlay with endogenous MD-GFP signal (green), red channel shown separately in insets. Cell nuclei are labeled blue with DAPI. **F:** Representative immunoblots (left) and summary (right) of altered expression of MD-specific proteins in renal cortical homogenates including Ccn1, Ccn3 and Cxcl14 in MD-NGFR KO versus WT mice. *: $p<0.05$, **$p<0.01$, data are mean ± SEM, n=4 mice each. Adapted from (61).

In contrast to control PBS or DMEMF12 medium which had no effect, treatment with CCN1 (either with low or high dose) or low salt conditioned MD medium caused strong improvements in albuminuria (Fig. 16C). In contrast to all other groups, treatment with low salt conditioned MD medium dramatically improved GFR, which returned to normal baseline levels indicating functional regression of FSGS pathology (Fig. 16B). Subsequent kidney histological analysis showed severe GS and tissue fibrosis in control PBS and DMEMF12-treated groups, while CCN1 or low salt conditioned MD medium treatments greatly improved FSGS histopathology, $p57^+$ podocyte number (Fig. 16D-F) and tubulointerstitial fibrosis suggesting structural regression of FSGS (70).

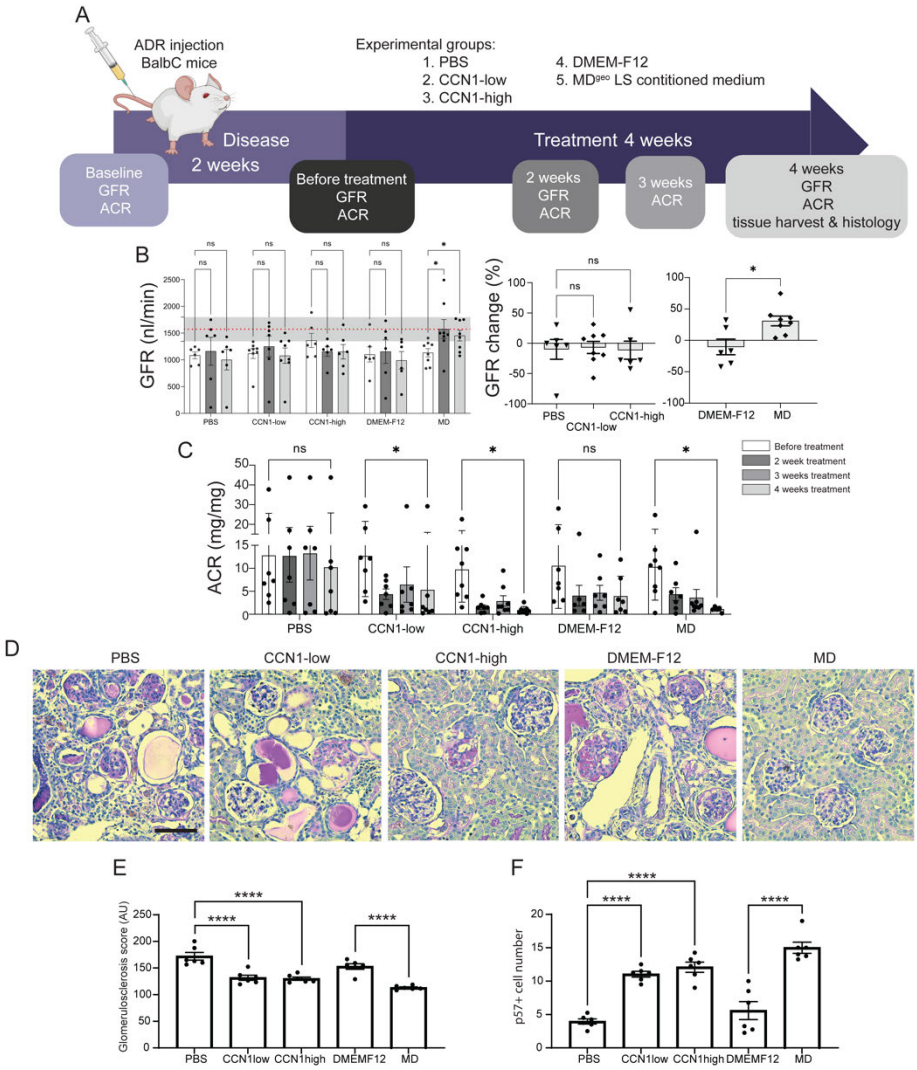

Figure 16. A: Illustration of therapeutic study design for testing the effects of MD biologicals (human recombinant CCN1 and LS-conditioned MD^{geo} cell culture media) using the Adriamycin (ADR) model of glomerulosclerosis in BalbC mice. **B:** Time-course of the absolute (left panel) and relative (normalized to baseline before treatment, right panels) changes in GFR followed in the same mice measured by the MediBeacon non-invasive transcutaneous method. Note the significant improvement of GFR returning to normal baseline levels (red dotted line representing mean ± SEM (grey shaded area), measured at baseline) in the MD treatment group indicating functional regression of FSGS pathology. **C:** Time-course of albuminuria (Albumin/Creatinine Ratio, ACR) changes followed in the same mice measured by ELISA. Note the significant improvement in albuminuria in the CCN1 and MD treatment groups in contrast to the PBS and DMEM-F12 controls. **D:** Representative images of PAS-stained histological sections of kidney tissues harvested at the end of treatment in all treatment groups. **E:** Quantification of glomerulosclerosis evaluated blindly by measuring the density of PAS staining on histological sections using Image J. **F:** Podocyte preservation calculated in tissue volumes based on the number of p57^{+} cells. Ns=not significant, *P<0.05, **P<0.01, ***P<0.001, ****P<0.0001, n=6-8 mice each, histological data points represent the average of n=20 glomeruli per animal, n=6 mice each. Adapted from (70).

5. DISCUSSION

The present study provided an unprecedentedly detailed view and comprehensive molecular, structural, and functional analysis of the unique specialized renal epithelium of the MD, by taking advantage of the newly developed next generation MD research toolbox. Several major research technology innovations developed in this work made it possible to (i) directly visualize the unique Ca^{2+}signaling and pacemaker activities of single MD cells *in vivo* (using sc4DP) that are altered by sensing the systemic and local tissue environment via multi-organ crosstalk, (ii) establish the neuron-like gene profile of MD cells (using bulk and scRNA sequencing) providing molecular detail of their heterogenous biological and physiological functions, (iii) identify NGF signaling as the principal regulatory mechanism of MD cells and their control of key kidney functions and role in disease development (using the new MD cell line mMD^{geo} and MD-NGFR KO mice), (iv) directly visualize kidney tissue remodeling via deploying serial *in vivo* multiphoton microscopy to track single progenitor cells in the exact same mouse and kidney tissue volume over time, and (v) uncover the molecular details of the MD regenerative program activated by physiological stimuli and its potential to be therapeutically targeted. As a result, our work painted a paradigm shifting new view of macula densa function as the nephron central command. Due to the molecular-level new knowledge of multi-organ relevant functions of MD cells established here, our new MD cell research toolbox will be useful for future cell biology studies in the kidney, heart, intestine, pancreas and brain and directly relevant to modeling kidney and neurodegenerative diseases.

The newly discovered role of MD cells in endogenous kidney tissue remodeling and repair is a significant advance in the renal and cardiovascular field and promises the development of new regenerative therapeutic approaches for kidney and potentially other organ diseases. The concept that organ-specific physiological activation of chief, neuron-like cells orchestrate resident progenitor cell-mediated endogenous tissue repair has strong foundations in evolutionary biology, physiology, clinical nephrology, and recent developments in regenerative biology. The loss and conservation of body fluid and salt is known as a major driver of the evolution of the mammalian nephron (12), plays major role in physiological adaptations to maintain body fluid homeostasis and blood pressure (13), and in the protective effect of low dietary salt intake (and ACEi) to slow down CKD

progression (73, 74). Some of the presently identified MD mechanisms (e.g. Wnt signaling and CCN1) have well-known roles in the remodeling and repair of many tissues and organs (75, 76), while others (Aard, Pamr1) are yet to be explored in the kidney and beyond.

MD cells are chief salt sensors and regulators of kidney function, but our knowledge of these unique cells has been limited to their role in maintaining renal hemodynamics and activity of the renin-angiotensin system (13). The distinctively high MD cell MAPK (47), mTOR (63), and now calcium (Fig. 10), Wnt (Fig. 13) (70) and Ngfr (Fig. 15) signaling activity among all renal cell types, their newly identified neuron-like microanatomical (Figs. 7-8) ((36) and now detailed molecular (Figs. 11-13) and functional features (Figs. 10, 14-15) altogether firmly establish that the MD functions as a neuron-like chief cell of the nephron. The newly identified key function of MD cells as drivers of local progenitor cells and tissue remodeling is in line with the recently identified role of peripheral neurons in local tissue regeneration of the skin (33-35). However, this study is the first describing such local neuroregulatory mechanism driving the physiological activation-based regeneration of a major internal organ. It is interesting to speculate why the presently identified fundamental MD functions have been previously overlooked. The reasons likely include technology limitations and the nature of the inaccessible, minority cell type of MD cells that were difficult to study in the past. In addition, the elements in the western diet (e.g. high dietary salt intake) may blunt this endogenous regenerative mechanism.

Our group recently established serial intravital MPM imaging to track the fate of individual, genetically labeled renal cell types over several days in the intact kidney (41, 43, 71, 77), which technique was applied in the present work for different mesenchymal and endothelial precursor cell types and in renal injury (70) and physiological activation conditions (Fig. 14B). This technological advance and approach provided critically valuable visual clues regarding the dynamic (within two weeks) and the MD-centric pattern of the recruitment and clonal propagation of vascular pole progenitor cells (Figs. 14B-C). Complemented with histological analysis and the glomerular vascular pole accumulation of $Renin^+$, $WT1^+$ and $CD34^+$ cells (70) that are known mesenchymal /podocyte and endothelial progenitor cell markers (40, 77-79) under MD stimulation conditions, these results strongly suggested the MD secretion and paracrine actions of

local tissue remodeling factors that control the activation, recruitment and differentiation of resident progenitor cells. It needs to be emphasized that in this regenerative multicellular unit, each cell type shares equal importance in tissue remodeling including the chief and sensory MD cells and the various local progenitor cell effectors including cells of the renin lineage. Vascular pole endothelial progenitors and cells of the renin lineage have been recently identified as local progenitor cells for glomerular cell types (40, 43). The appearance and clonal expansion of a $WT1^+/Renin^+$ mesenchymal cell population under the MD base in response to LS+ACEi or genetic manipulations (Fig. 14C (70) are consistent with the important role of MD cells and with the recently established role of WT1 in the proliferation, migration, and differentiation of the cells of the renin lineage toward podocyte fate (77). The MD point-source origin of tissue remodeling factors may provide for a 3D structured tissue remodeling program in each nephron that likely involves a complex balancing act between inflammatory/pro-fibrotic and regenerative/anti-fibrotic mechanisms. The known biological activities of the presently identified multiple secreted MD tissue remodeling factors (Fig. 13) is supportive of this view. The MD-centric progenitor cell recruitment and tissue remodeling pattern suggests the involvement of MD-derived mechanism in the previously described progenitor/podocyte cell marker gradient (80) and podocyte precursor cell accumulation in the vascular pole region of Bowman's capsule including at young age (81, 82) and in response to ACEi treatment (83). Cox-2 and Nos1 dependence of mesenchymal and endothelial progenitor cell recruitment (70) is consistent with the role of MD cell factors, including PGE_2 that was shown to activate the recruitment and differentiation of $CD44^+$ mesenchymal progenitors to the renin cell fate (84). In addition, our results suggest that targeting the presently identified MD-driven tissue remodeling mechanism may be involved in the protective effects of selective Cox-2 inhibition in diabetic kidney injury, which is associated with MD gain-of-function (85, 86).

Additional applications of *in vivo* single-cell 4D physiology (sc4DP) studies using MPM imaging of MD cell calcium signaling (Fig. 10A-B), complemented with structural (Fig. 10C-D) and transcriptomic analysis (Figs. 11-12) uncovered the neuron-like differentiation and chief function of MD cells among all renal cell types. In fact, the presently uncovered new cell physiology features introduce a paradigm-shifting new view of MD cells, including the autonomous, rhythmic Ca^{2+} firing (pacemaker function,

oscillator of the nephron), the coordination and clustering of single MD cell Ca^{2+} transients into a cumulative whole-MD signal that translates to the oscillatory regulation of key whole-organ functions (e.g. blood flow and tubular flow) and ultimately the function of all renal cells. MD cells are currently known as the sensor of the TGF component of the regular physiological oscillations in renal blood flow and glomerular filtration rate that has an established frequency of 0.03 Hz and cycle time of 30-50 s (87). The oscillation frequency of whole-MD Ca^{2+} signal found in the present study (0.03 Hz) is a perfect match with that of TGF established earlier (87), and the peak MD Ca^{2+} is phase-matched with the most dilated state of the AA (Fig. 10B). These results suggest that the MD is the primary oscillator and driver, rather than simply the sensor in TGF, and that one of the many potential functions of MD Ca^{2+} signals is the periodic generation of vasodilator effectors (likely NO and PGE_2) that cause paracrine AA dilatations, increased blood flow and glomerular filtration. In fact, the Nos1 and Cox2 enzymes that generate these vasodilators are known classic MD-specific markers in the renal cortex (13, 19, 20) and known to be Ca^{2+} sensitive (88, 89). Importantly, MD Ca^{2+} activity increased in response to stimuli that cause low salt in the tubular fluid microenvironment including low salt diet and the diuretic furosemide that inhibit MD NaCl entry via Nkcc2 (Slc12a1) (Fig. 10B) (61). This is consistent with the classic function of MD cells in tubular fluid salt sensing that is known to involve Nkcc2 and MD cell depolarization in response to altered luminal [NaCl] (90). In addition to tubular salt, MD cells were able to directly sense numerous diverse signals from the local tissue and systemic environment and to process them and modulate their Ca^{2+} activity accordingly, suggesting their major function in interoception. Functional (61), structural (Fig. 10D) and molecular genetic evidence (Figs. 11-12) of both pre and postsynaptic markers suggested the presence of synapses between individual MD cells and sympathetic and sensory nerve endings. Their potential roles include local cell-to-cell communication and coordination within the whole-MD (formation of the MD neural network), direct regulation of MD cell function by sympathetic efferent nerves and providing sensory input to the central nervous system via afferent renal nerves. The physical shape of the MD plaque, a niche of ~20-25 cells appears to match its function as it resembles a peripheral ganglion (Fig. 10). In fact, the MD neural networks in each nephron that were identified in the present study may represent a new “renal nervous system” controlling kidney function and sensing the

internal milieu of the entire body in a novel peripheral interoceptive neural pathway. Functional interconnections of MD neural networks in each nephron and between the local peripheral MD "ganglia" and the central nervous system via sensory nerves are exciting possibilities for exploration in future work. Importantly, our results on the neuron-like MD cells controlling resident progenitor cells are consistent with the role of peripheral neuronal activity in local tissue regeneration in the skin (33-35).

The other technology advance that provided critically important new information on MD cell function in the present work is their detailed high-resolution transcriptome analysis using both bulk and single-cell RNA sequencing of MD enriched cell populations (Figs. 11-13). Until now, only a few studies reported limited MD transcriptome data using a low number of cells (32, 91-93). The high MD expression of secreted angiogenic, cell migration and patterning, growth, and ECM remodeling factors (Fig. 13) at a molecular-level and the intravital progenitor cell-tracking results (Fig. 14) together provide strong support for the newly identified tissue regenerative role of MD cells. Consistent with the activation of the MD tissue remodeling program by physiological stimuli (LS+ACEi treatment), the same stimulation increased the expression of key MD-specific factors underlying this function (Fig. 13). The top MD-enriched angiogenic (*Pappa2, Pamr1, Sfrp1, Vash2, Vegfa, Ccn1*), cell migration and patterning (*Unc5d, Sema3c, Robo2, Slit2*), growth (*Bmp3, Egf, Fgf9*) and ECM signaling and remodeling (*Frem1, Thsd4, Mmp14, Adamtsl2*) factors and gene networks, cytokines and chemokines have well-defined roles in angiogenesis, progenitor cell recruitment and differentiation, extracellular matrix and tissue remodeling, and regeneration of several organs (76, 94, 95). The MD secretion of several of these factors including the anti-fibrotic angiogenesis modulator Ccn1 was confirmed in the present study (Fig. 13). While the secretion of these tissue remodeling factors by MD cells is in general consistent with the observed MD-centric pattern of mesenchymal and endothelial progenitor cell recruitment (Fig. 14), identification of their specific function and contribution to the MD tissue remodeling and repair program requires future work. The presence of a dense network of long, basal MD cell processes that make contact with various target cells at the glomerular vascular pole and contain secretory cargo including Pappa2 (Figs. 7-9) (36) is consistent with the presently identified new MD cell function. In addition, our recent study demonstrated that among all renal cell types, MD cells have the highest rate of protein synthesis that is further

stimulated by low salt diet (63), suggesting that MD cells synthesize and secrete the above factors under both control and stimulated conditions. The altered synthesis of at least some of these new MD proteins in MD-Wnt^{gof} mice (70) and MD-NGFR KO mice (Fig. 15F) and the resulting tissue structural alterations further support this MD function.

Both pharmacological (Cox-2 and Nos1 inhibitors, (70)) and genetic approaches (MD-Wnt$^{gof/lof}$ mice (70) and MD-NGFR KO mice (Fig. 15)) validated the MD-specificity of the newly discovered endogenous tissue remodeling pathway. While the role of Wnt in this new MD mechanism was much expected due to the high expression of several Wnt target genes (Fig. 13) and its well-known function in tissue regeneration (75), additional major signaling pathways are likely involved. Several molecular players of Notch, Shh, FGF, Hippo signaling are represented in the top enriched genes in the MD transcriptome (Fig. 13C-D). Future work is needed to dissect their roles in MD cells. NGF signaling via the p75NTR is another key MD cell signaling pathway identified in the present study that appears to be playing dual roles in MD cell neuronal differentiation and MD-directed tissue remodeling as well as in neurodegenerative pathology. In addition to the high level of Ngfr gene expression (Figs. 11-12), the acute administration of several p75NTR Ngfr agonists (NGF, LM11A-31, sAPPα) demonstrated functional expression of Ngfr in MD cells *in vivo* (Fig. 15C). Interestingly, NGF treatment significantly increased MD calcium in MD-NGFR KO compared to WT, which effect was likely due to enhanced NGF signaling via the TrkA/B NGF receptors that are also expressed in MD cells (Figs. 15C). Future investigation is needed regarding the complexity of MD cell NGF signaling including the identification of the receptor subtypes that are well established for other cell types (96) and the identity of the several potential agonists. Interestingly, JG renin cells, collecting duct intercalated cells and a subset of MD cells themselves appear to produce neurotrophins including NGF (61) and the related brain-derived neurotrophic factor (BDNF, Fig. 12F). This suggests bidirectional multi-cellular crosstalk between MD and other nearby cells including renin cells that are known to form a classic physiological functional unit with MD cells (13, 47, 97). The small molecule LM11A-31, a specific Ngfr modulator that is currently in human clinical trial had highly promising results in mouse models of Alzheimer's disease (96). sAPPα is another known p75NTR agonist with neuroprotective effects (98). Interestingly, Ngfr deficiency triggered MD hyperactivity at the single cell level (increased Ca^{2+} firing frequency, Fig.

15A) which may have been due to glutamatergic hyperexcitability or the loss or dysfunction of inhibitory GABAergic MD cells that are well-known key, early pathogenic events in the development of neurodegeneration (99). This, in turn, led to the loss of cell-to-cell connectivity and absence of the periodically oscillating vasomotor (TGF) signal at the whole-MD level (Fig. 15B). As a result of altered MD signaling, GFR declined, renin cell number decreased, and renal tissue fibrosis developed (Fig. 15D-E) which are classic features of CKD. The irregular chaotic oscillations in whole-MD Ca^{2+} that were observed in MD-Ngfr KO mice (Fig. 15B) were reminiscent of the previously reported chaotic oscillations in MD-mediated TGF in different models of hypertension (100, 101). These results suggest that chaotic behavior of the MD neural network is a common pathogenic feature of the dysregulated renal vascular control and blood flow in hypertension and kidney disease. Neurovascular dysfunction (Fig. 15B,D), pathological tissue remodeling (Fig. 15E), increased levels of phosphorylated tau that develop in response to altered NGF signaling in MD cells (Fig. 15E) are consistent with the pathobiology of neurodegenerative diseases (102, 103).

The structural and neuron-like functional heterogeneity between individual MD cells (Figs. 7,10,12) (36, 104) was reflected also in their regenerative gene profile established by single-cell transcriptome analysis (Figs. 12-13). The clustering of angiogenic, ECM remodeling, precursor, etc. MD cell subtypes (Fig. 13C) suggests that there may be individual MD cells dedicated to controlling endothelial, mesenchymal progenitor cells or self-renewal separately. The detailed characterization of the presently identified 5 MD cell subclusters (Fig. 13C), whether their calcium signaling activity (pacemaker, or highly connected hub cells, or lone cells as shown in Figs. 10C and 15B) corresponds to a specific tissue remodeling activity and/or 3D spatial localization in each nephron (afferent or efferent arteriole end or mesangium-facing localization) requires further study. Long-term genetic fate tracking of MD cells using inducible MD-GFP reporter mice did not find labeled cells outside the MD (data not shown), that suggests lack of MD cell differentiation to other renal cell types, at least in the mouse kidney.

The newly acquired knowledge on MD cells and their new functions suggest that these cells may play an important role in human kidney disease, and that targeting and augmenting MD mechanisms may improve CKD pathology. Therefore, additional studies were performed to translate the new MD function to the context of human kidney disease

(70) and therapeutic interventions (Fig. 16). CCN1 was specifically expressed in MD cells in the human kidney (70), and its expression was reduced in non-diabetic CKD based on both mRNA and protein levels.

The generation of the new MD cell line MD^{geo} (Fig. 5) was yet another critically important tool in this study that allowed the analysis of MD cell signaling (61), secretome (Fig. 13E) and testing of the therapeutic potential of MD-derived biologicals (Fig. 16). The use of either a specific, single (Ccn1) or a mixture of all MD factors (conditioned medium) provided initial proof-of-concept of the potent protective effects of targeting MD cell mechanisms (Fig. 16). MD-derived biologicals are readily available from the conditioned MD^{geo} culture medium (Fig. 13) that provided ease of therapeutic use in addition to recombinant proteins (Ccn1). Compared to before treatment, the dramatically improved albuminuria, GFR, and renal histopathology in response to treatment with low salt conditioned MD medium (and partially Ccn1) suggests functional and structural regression of pre-existing CKD (Figs. 16B-F). The dramatic improvements in GS and interstitial fibrosis observed in animals treated with CCN1 or low salt MD medium (Fig. 16D-F) is consistent with the known anti-fibrotic function of CCN1 (72, 76) and other MD-derived factors. It should be emphasized that the presently applied MD stimuli (LS+ACEi treatment, MD biologicals) that resulted in improved kidney structure and function were all applied temporarily. However, sustained overactivation of the MD including the presently identified endogenous tissue regenerative mechanism may become pathogenic as seen for example in early diabetes (23). To determine whether this new MD mechanism is involved in the protective effects of SGLT2 inhibitors (23), or if its stimulation or inhibition is relevant to different phases of diabetic or non-diabetic kidney disease requires further study. It is likely that the ultimate protective or pathogenic role, and therefore the potential therapeutic targeting of the new MD tissue regenerative program is context dependent.

6. CONCLUSIONS

1. The newly developed next generation MD research toolbox and its applications painted a paradigm shifting new view of the structure, molecular details, function, and multi-organ crosstalk of the macula densa (Figure 17).
2. Genetic labeling of single MD cells for the first time in MD-GFP mouse kidneys and their high resolution MPM imaging found physiologically regulated dense network of major and minor processes at the cell base, called maculapodia, projecting toward the glomerulus, extraglomerular mesangial cells, and other MD cells. These dynamic and secretory microanatomical features serve as structural basis for cell-to-cell communication within the JGA, between the MD itself and other target cells.
3. MD cells are the nephron central command. Calcium imaging of MD cells and other kidney cell types with high temporal and spatial resolution and complemented with transcriptome analysis uncovered new cell physiology features, including the autonomous rhythmic calcium firing and the coordination and clustering of single MD cell calcium transients into cumulative whole-MD calcium output to drive whole organ function.
4. Physiological activation of the nephron central command (MD) drives endogenous nephron remodeling and repair including the glomerular filtration barrier (GFB), endothelium and podocytes. Live tracking of endogenous kidney tissue remodeling complemented with transcriptome analysis and MD genetic and pharmacological manipulations identified MD cells as chief sensory and regulatory cell type in the kidney. MD cells synthetize and secrete numerous angiogenic, cell migration and patterning, growth and extracellular matrix signaling and remodeling factors that act on local progenitor cells in a paracrine fashion to orchestrate tissue remodeling.
5. The loss and conservation of body fluid and salt, the known major driver of the evolution and the function of the mammalian nephron is the strongest stimulus to activate the MD regenerative program. Hence it drives endogenous kidney tissue remodeling and has clinical implications in the long-known protective effects of low dietary salt intake and ACEi to slow down CKD progression.
6. NGF signaling via p75NTR is a novel and key MD cell signaling pathway playing dual roles in MD cell neuronal differentiation and MD directed tissue remodeling. The loss of MD neuronal differentiation via genetic manipulations of p75NTR

expression resulted in the loss of coordination and clustering of single MD cell signaling leading to a loss of hemodynamic control, increased expression and accumulation of neurodegenerative proteins, and ultimately kidney fibrosis. Hence the loss of MD cell neuronal differentiation represents a novel neurodegenerative component of CKD.

7. Therapeutic targeting of the MD specific tissue regenerative program may serve as a novel specific and mechanism-based regenerative therapy that can achieve disease regression. Human translational studies revealed that CCN1, one of the top MD specific secreted angiogenic factors in the kidney, are among the top 1% under expressed genes in CKD regardless of disease etiology. Targeting of the novel MD tissue remodeling program using MD biologicals resulted in the regression of CKD in a pre-clinical mouse model. The identification and characterization of this new MD mechanism provides key initial steps to develop a new class of drugs, MD cell mimetics, targeting the MD cell neuronal and tissue regenerative program.

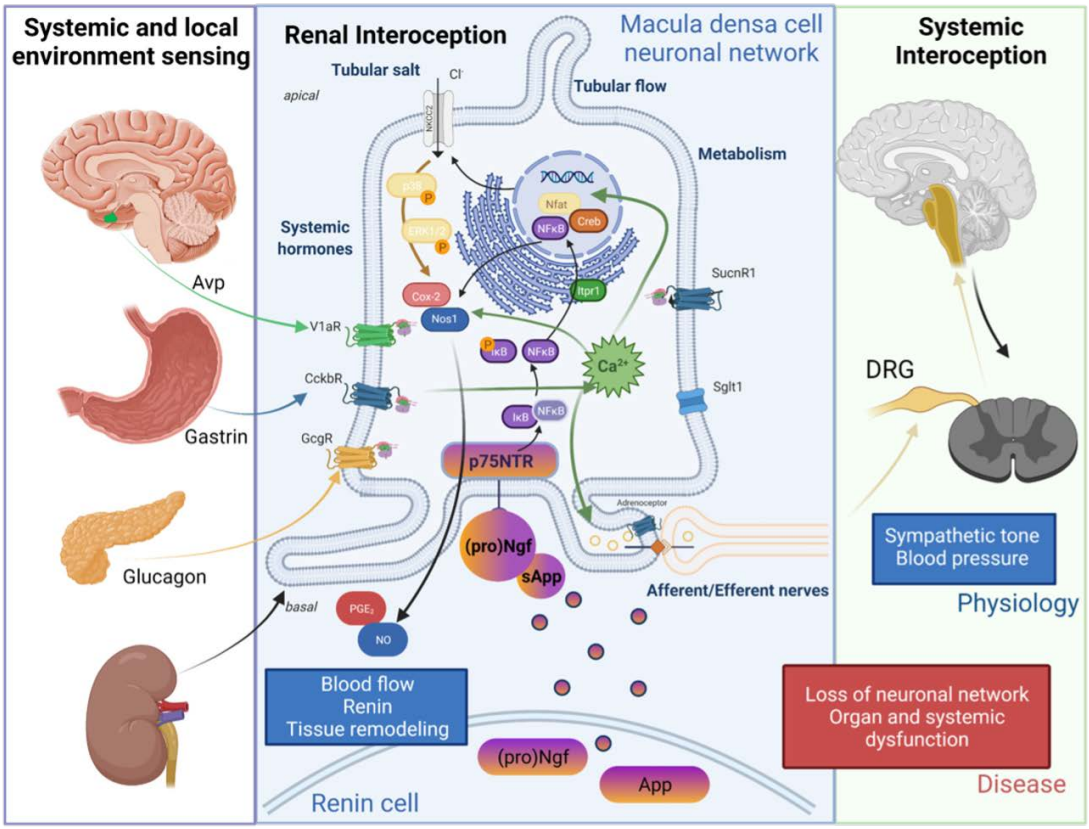

Figure 17. Schematic illustration of the novel MD cell function as sensory neuron-like chief cells in the kidney. MD cells sense and respond to local and systemic stimuli and serve as the nephron central command, as well as play a major role in whole-body homeostasis and disease development. Adapted from (61).

7. SUMMARY

In summary, the present study uncovered a novel endogenous tissue remodeling mechanism in the kidney that is activated by the physiological stimulation of MD cells that function as peripheral sensory neuron-like chief cells of the nephron. The MD program for kidney tissue remodeling and repair controls resident progenitor cells including cells of the renin lineage via secreted angiogenic, growth and extracellular matrix remodeling factors, cytokines and chemokines (Fig. 18). The physiologically regulated microanatomical features, the maculapodia of MD cells serve as the structural basis of cell-to-cell communication in the JGA between the MD itself and other target cells. *In vivo* multiphoton calcium imaging of single MD cells, and the whole macula densa as a functional unit proved that MD cells are the nephron central command and regulate organ function and organ blood flow. The MD specific enrichment of several signaling pathways (Wnt, Ngfr) and secreted angiogenic and tissue remodeling factors (CCN1) provided molecular level details for this novel MD cell function. MD cells control renal hemodynamics on a short time scale (seconds) and endogenous kidney tissue remodeling over longer time periods (days and weeks) with the same ultimate goal to maintain kidney function and whole-body homeostasis. The identification and molecular characterization of this new MD mechanism provided here the opportunity for human and preclinical therapeutic translation which represent key initial steps in further developing and targeting this pathway in the future for diagnostic and therapeutic purposes.

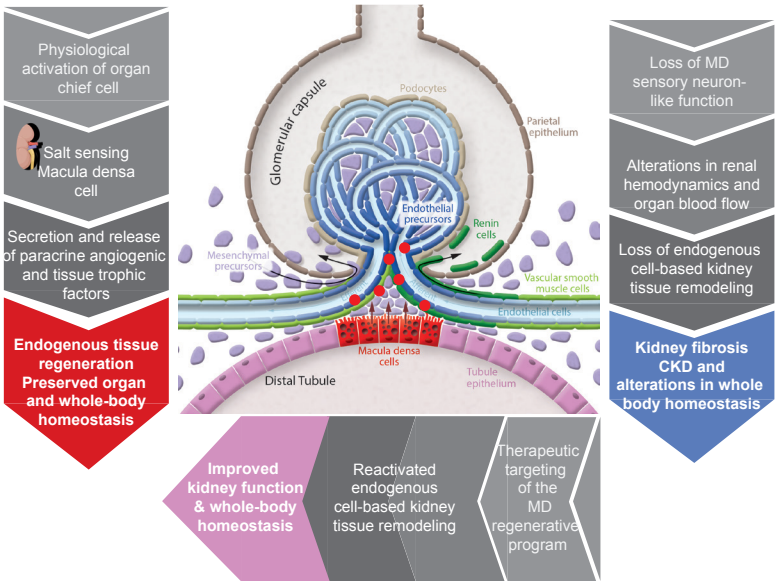

Figure 18. Summary of the novel tissue remodeling function of MD cells, activation in physiological state, loss in disease, and reactivation in therapeutic targeting. Adapted from (70).

8. REFERENCES

1. Go AS, Chertow GM, Fan D, McCulloch CE, Hsu CY. Chronic kidney disease and the risks of death, cardiovascular events, and hospitalization. N Engl J Med. 2004;351(13):1296-1305.

2. Centers for Disease Control and Prevention. Chronic Kidney Disease Surveillance System website. https://www.cdc.gov/kidneydisease/publications-resources/ckd-national-facts.html Downloaded on 08/10/2023.

3. Saran R, Robinson B, Abbott KC, Bragg-Gresham J, Chen X, Gipson D, Gu H, Hirth RA, Hutton D, Jin Y, Kapke A, Kurtz V, Li Y, McCullough K, Modi Z, Morgenstern H, Mukhopadhyay P, Pearson J, Pisoni R, Repeck K, Schaubel DE, Shamraj R, Steffick D, Turf M, Woodside KJ, Xiang J, Yin M, Zhang X, Shahinian V. US Renal Data System 2019 Annual Data Report: Epidemiology of Kidney Disease in the United States. Am J Kidney Dis. 2020;75(1 Suppl 1):A6-a7.

4. Prevention CfDCa. Chronic Kidney Disease in the United States Atlanta GA: US Department of Health and Human Services, Centers for Disease Control and Prevention; 2023 [Available from: https://www.cdc.gov/kidneydisease/publications-resources/ckd-national-facts.html. Downloaded on 08/10/2023.

5. Kovesdy CP. Epidemiology of chronic kidney disease: an update 2022. Kidney Int Suppl (2011). 2022;12(1):7-11.

6. Thurlow JS, Joshi M, Yan G, Norris KC, Agodoa LY, Yuan CM, Nee R. Global Epidemiology of End-Stage Kidney Disease and Disparities in Kidney Replacement Therapy. Am J Nephrol. 2021;52(2):98-107.

7. Heerspink HJL, Stefansson BV, Chertow GM, Correa-Rotter R, Greene T, Hou FF, Lindberg M, McMurray J, Rossing P, Toto R, Langkilde AM, Wheeler DC. Rationale and protocol of the Dapagliflozin And Prevention of Adverse outcomes in Chronic Kidney Disease (DAPA-CKD) randomized controlled trial. Nephrol Dial Transplant. 2020;35(2):274-282.

8. Iismaa SE, Kaidonis X, Nicks AM, Bogush N, Kikuchi K, Naqvi N, Harvey RP, Husain A, Graham RM. Comparative regenerative mechanisms across different mammalian tissues. NPJ Regen Med. 2018;3:6.

9. Cheng CW, Villani V, Buono R, Wei M, Kumar S, Yilmaz OH, Cohen P, Sneddon JB, Perin L, Longo VD. Fasting-Mimicking Diet Promotes Ngn3-Driven β-Cell Regeneration to Reverse Diabetes. Cell. 2017;168(5):775-788.e712.

10. Brandhorst S, Choi IY, Wei M, Cheng CW, Sedrakyan S, Navarrete G, Dubeau L, Yap LP, Park R, Vinciguerra M, Di Biase S, Mirzaei H, Mirisola MG, Childress P, Ji L, Groshen S, Penna F, Odetti P, Perin L, Conti PS, Ikeno Y, Kennedy BK, Cohen P, Morgan TE, Dorff TB, Longo VD. A Periodic Diet that Mimics Fasting Promotes Multi-System Regeneration, Enhanced Cognitive Performance, and Healthspan. Cell Metab. 2015;22(1):86-99.

11. Ransom RC, Carter AC, Salhotra A, Leavitt T, Marecic O, Murphy MP, Lopez ML, Wei Y, Marshall CD, Shen EZ, Jones RE, Sharir A, Klein OD, Chan CKF, Wan DC, Chang HY, Longaker MT. Mechanoresponsive stem cells acquire neural crest fate in jaw regeneration. Nature. 2018;563(7732):514-521.

12. Romagnani P, Lasagni L, Remuzzi G. Renal progenitors: an evolutionary conserved strategy for kidney regeneration. Nat Rev Nephrol. 2013;9(3):137-146.

13. Peti-Peterdi J, Harris RC. Macula densa sensing and signaling mechanisms of renin release. J Am Soc Nephrol. 2010;21(7):1093-1096.

14. Cangiotti AM, Lorenzi T, Zingaretti MC, Fabri M, Morroni M. Polarized Ends of Human Macula Densa Cells: Ultrastructural Investigation and Morphofunctional Correlations. Anat Rec (Hoboken). 2018;301(5):922-931.

15. Sipos A, Vargas S, Peti-Peterdi J. Direct demonstration of tubular fluid flow sensing by macula densa cells. Am J Physiol Renal Physiol. 2010;299(5):F1087-1093.

16. Brenner BM, Rector FC. The kidney: WB Saunders Company; 1976.

17. Bell PD, Lapointe JY, Peti-Peterdi J. Macula densa cell signaling. Annu Rev Physiol. 2003;65:481-500.

18. Cheng HF, Wang JL, Zhang MZ, McKanna JA, Harris RC. Role of p38 in the regulation of renal cortical cyclooxygenase-2 expression by extracellular chloride. J Clin Invest. 2000;106(5):681-688.

19. Harris RC, McKanna JA, Akai Y, Jacobson HR, Dubois RN, Breyer MD. Cyclooxygenase-2 is associated with the macula densa of rat kidney and increases with salt restriction. J Clin Invest. 1994;94(6):2504-2510.

20. Mundel P, Bachmann S, Bader M, Fischer A, Kummer W, Mayer B, Kriz W. Expression of nitric oxide synthase in kidney macula densa cells. Kidney Int. 1992;42(4):1017-1019.

21. Peti-Peterdi J, Komlosi P, Fuson AL, Guan Y, Schneider A, Qi Z, Redha R, Rosivall L, Breyer MD, Bell PD. Luminal NaCl delivery regulates basolateral PGE2 release from macula densa cells. J Clin Invest. 2003;112(1):76-82.

22. Yang T, Park JM, Arend L, Huang Y, Topaloglu R, Pasumarthy A, Praetorius H, Spring K, Briggs JP, Schnermann J. Low chloride stimulation of prostaglandin E2 release and cyclooxygenase-2 expression in a mouse macula densa cell line. J Biol Chem. 2000;275(48):37922-37929.

23. Anders HJ, Davis JM, Thurau K. Nephron Protection in Diabetic Kidney Disease. N Engl J Med. 2016;375(21):2096-2098.

24. Chen WG, Schloesser D, Arensdorf AM, Simmons JM, Cui C, Valentino R, Gnadt JW, Nielsen L, Hillaire-Clarke CS, Spruance V, Horowitz TS, Vallejo YF, Langevin HM. The Emerging Science of Interoception: Sensing, Integrating, Interpreting, and Regulating Signals within the Self. Trends Neurosci. 2021;44(1):3-16.

25. Berntson GG, Khalsa SS. Neural Circuits of Interoception. Trends Neurosci. 2021;44(1):17-28.

26. Khalsa SS, Adolphs R, Cameron OG, Critchley HD, Davenport PW, Feinstein JS, Feusner JD, Garfinkel SN, Lane RD, Mehling WE, Meuret AE, Nemeroff CB, Oppenheimer S, Petzschner FH, Pollatos O, Rhudy JL, Schramm LP, Simmons WK, Stein MB, Stephan KE, Van den Bergh O, Van Diest I, von Leupoldt A, Paulus MP. Interoception and Mental Health: A Roadmap. Biol Psychiatry Cogn Neurosci Neuroimaging. 2018;3(6):501-513.

27. Holzer P. Gut Signals and Gut Feelings: Science at the Interface of Data and Beliefs. Front Behav Neurosci. 2022;16:929332.

28. Da Silva Xavier G, Rutter GA. Metabolic and Functional Heterogeneity in Pancreatic β Cells. J Mol Biol. 2020;432(5):1395-1406.

29. Drumm BT, Hennig GW, Battersby MJ, Cunningham EK, Sung TS, Ward SM, Sanders KM, Baker SA. Clustering of Ca(2+) transients in interstitial cells of Cajal defines slow wave duration. J Gen Physiol. 2017;149(7):703-725.

30. Liang D, Xue Z, Xue J, Xie D, Xiong K, Zhou H, Zhang F, Su X, Wang G, Zou Q, Liu Y, Yang J, Ma H, Peng L, Zeng C, Li G, Wang L, Chen YH. Sinoatrial node pacemaker cells share dominant biological properties with glutamatergic neurons. Protein Cell. 2021;12(7):545-556.

31. Osborn JW, Tyshynsky R, Vulchanova L. Function of Renal Nerves in Kidney Physiology and Pathophysiology. Annu Rev Physiol. 2021;83:429-450.

32. Chen L, Chou CL, Knepper MA. Targeted Single-Cell RNA-seq Identifies Minority Cell Types of Kidney Distal Nephron. J Am Soc Nephrol. 2021;32(4):886-896.

33. Huang S, Kuri P, Aubert Y, Brewster M, Li N, Farrelly O, Rice G, Bae H, Prouty S, Dentchev T, Luo W, Capell BC, Rompolas P. Lgr6 marks epidermal stem cells with a nerve-dependent role in wound re-epithelialization. Cell Stem Cell. 2021;28(9):1582-1596.e1586.

34. Zhang B, Ma S, Rachmin I, He M, Baral P, Choi S, Gonçalves WA, Shwartz Y, Fast EM, Su Y, Zon LI, Regev A, Buenrostro JD, Cunha TM, Chiu IM, Fisher DE, Hsu YC. Hyperactivation of sympathetic nerves drives depletion of melanocyte stem cells. Nature. 2020;577(7792):676-681.

35. Shwartz Y, Gonzalez-Celeiro M, Chen CL, Pasolli HA, Sheu SH, Fan SM, Shamsi F, Assaad S, Lin ET, Zhang B, Tsai PC, He M, Tseng YH, Lin SJ, Hsu YC. Cell Types Promoting Goosebumps Form a Niche to Regulate Hair Follicle Stem Cells. Cell. 2020;182(3):578-593.e519.

36. Gyarmati G, Shroff UN, Riquier-Brison A, Kriz W, Kaissling B, Neal CR, Arkill KP, Ahmadi N, Gill IS, Moon JY, Desposito D, Peti-Peterdi J. A new view of macula densa cell microanatomy. Am J Physiol Renal Physiol. 2021;320(3):F492-f504.

37. Moeller MJ, Sanden SK, Soofi A, Wiggins RC, Holzman LB. Podocyte-specific expression of cre recombinase in transgenic mice. Genesis. 2003;35(1):39-42.

38. Sun YB, Qu X, Zhang X, Caruana G, Bertram JF, Li J. Glomerular endothelial cell injury and damage precedes that of podocytes in adriamycin-induced nephropathy. PLoS One. 2013;8(1):e55027.

39. Ritsma L, Steller EJ, Ellenbroek SI, Kranenburg O, Borel Rinkes IH, van Rheenen J. Surgical implantation of an abdominal imaging window for intravital microscopy. Nat Protoc. 2013;8(3):583-594.

40. Kaverina NV, Kadoya H, Eng DG, Rusiniak ME, Sequeira-Lopez ML, Gomez RA, Pippin JW, Gross KW, Peti-Peterdi J, Shankland SJ. Tracking the stochastic fate of cells of the renin lineage after podocyte depletion using multicolor reporters and intravital imaging. PLoS One. 2017;12(3):e0173891.

41. Hackl MJ, Burford JL, Villanueva K, Lam L, Suszták K, Schermer B, Benzing T, Peti-Peterdi J. Tracking the fate of glomerular epithelial cells in vivo using serial multiphoton imaging in new mouse models with fluorescent lineage tags. Nat Med. 2013;19(12):1661-1666.

42. Kang JJ, Toma I, Sipos A, McCulloch F, Peti-Peterdi J. Quantitative imaging of basic functions in renal (patho)physiology. Am J Physiol Renal Physiol. 2006;291(2):F495-502.

43. Desposito D, Schiessl IM, Gyarmati G, Riquier-Brison A, Izuhara AK, Kadoya H, Der B, Shroff UN, Hong YK, Peti-Peterdi J. Serial intravital imaging captures dynamic and functional endothelial remodeling with single-cell resolution. JCI Insight. 2021;6(10).

44. Shroff UN, Gyarmati G, Izuhara A, Deepak S, Peti-Peterdi J. A new view of macula densa cell protein synthesis. Am J Physiol Renal Physiol. 2021.

45. Salem V, Silva LD, Suba K, Georgiadou E, Neda Mousavy Gharavy S, Akhtar N, Martin-Alonso A, Gaboriau DCA, Rothery SM, Stylianides T, Carrat G, Pullen TJ, Singh SP, Hodson DJ, Leclerc I, Shapiro AMJ, Marchetti P, Briant LJB, Distaso W, Ninov N, Rutter GA. Leader β-cells coordinate Ca(2+) dynamics across pancreatic islets in vivo. Nat Metab. 2019;1(6):615-629.

46. Scarfe L, Schock-Kusch D, Ressel L, Friedemann J, Shulhevich Y, Murray P, Wilm B, de Caestecker M. Transdermal Measurement of Glomerular Filtration Rate in Mice. J Vis Exp. 2018(140).

47. Riquier-Brison ADM, Sipos A, Prókai Á, Vargas SL, Toma L, Meer EJ, Villanueva KG, Chen JCM, Gyarmati G, Yih C, Tang E, Nadim B, Pendekanti S, Garrelds IM, Nguyen G, Danser AHJ, Peti-Peterdi J. The macula densa prorenin receptor is essential in renin release and blood pressure control. Am J Physiol Renal Physiol. 2018;315(3):F521-f534.

48. Ranjit S, Dobrinskikh E, Montford J, Dvornikov A, Lehman A, Orlicky DJ, Nemenoff R, Gratton E, Levi M, Furgeson S. Label-free fluorescence lifetime and second

harmonic generation imaging microscopy improves quantification of experimental renal fibrosis. Kidney Int. 2016;90(5):1123-1128.

49. Uhlén M, Fagerberg L, Hallström BM, Lindskog C, Oksvold P, Mardinoglu A, Sivertsson Å, Kampf C, Sjöstedt E, Asplund A, Olsson I, Edlund K, Lundberg E, Navani S, Szigyarto CA, Odeberg J, Djureinovic D, Takanen JO, Hober S, Alm T, Edqvist PH, Berling H, Tegel H, Mulder J, Rockberg J, Nilsson P, Schwenk JM, Hamsten M, von Feilitzen K, Forsberg M, Persson L, Johansson F, Zwahlen M, von Heijne G, Nielsen J, Pontén F. Proteomics. Tissue-based map of the human proteome. Science. 2015;347(6220):1260419.

50. Lindström NO, McMahon JA, Guo J, Tran T, Guo Q, Rutledge E, Parvez RK, Saribekyan G, Schuler RE, Liao C, Kim AD, Abdelhalim A, Ruffins SW, Thornton ME, Baskin L, Grubbs B, Kesselman C, McMahon AP. Conserved and Divergent Features of Human and Mouse Kidney Organogenesis. J Am Soc Nephrol. 2018;29(3):785-805.

51. Gyarmati G, Shroff UN, Riquier-Brison A, Stocker SD, Izuhara A, Deepak S, Chen Y, Biemesderfer D, James A, Minichiello L, Zlokovic BV, Peti-Peterdi J. Neuron-like function of the nephron central command. bioRxiv. 2021:2021.2012.2006.471478.

52. Dobin A, Davis CA, Schlesinger F, Drenkow J, Zaleski C, Jha S, Batut P, Chaisson M, Gingeras TR. STAR: ultrafast universal RNA-seq aligner. Bioinformatics. 2013;29(1):15-21.

53. Mudge JM, Harrow J. Creating reference gene annotation for the mouse C57BL6/J genome assembly. Mamm Genome. 2015;26(9-10):366-378.

54. Bullard JH, Purdom E, Hansen KD, Dudoit S. Evaluation of statistical methods for normalization and differential expression in mRNA-Seq experiments. BMC Bioinformatics. 2010;11:94.

55. McInnes L, Healy J, Saul N, Großberger L. UMAP: Uniform Manifold Approximation and Projection. Journal of Open Source Software. 2018;3(29):861.

56. Kovács G, Komlósi P, Fuson A, Peti-Peterdi J, Rosivall L, Bell PD. Neuronal nitric oxide synthase: its role and regulation in macula densa cells. J Am Soc Nephrol. 2003;14(10):2475-2483.

57. McDonough AA, Veiras LC, Minas JN, Ralph DL. Considerations when quantitating protein abundance by immunoblot. Am J Physiol Cell Physiol. 2015;308(6):C426-433.

58. Rinschen MM. Single glomerular proteomics: A novel tool for translational glomerular cell biology. Methods Cell Biol. 2019;154:1-14.
59. Cox J, Mann M. MaxQuant enables high peptide identification rates, individualized p.p.b.-range mass accuracies and proteome-wide protein quantification. Nat Biotechnol. 2008;26(12):1367-1372.
60. Cox J, Hein MY, Luber CA, Paron I, Nagaraj N, Mann M. Accurate proteome-wide label-free quantification by delayed normalization and maximal peptide ratio extraction, termed MaxLFQ. Mol Cell Proteomics. 2014;13(9):2513-2526.
61. Gyarmati G, Shroff UN, Riquier-Brison A, Stocker SD, Izuhara A, Deepak S, Chen Y, Biemesderfer D, James AW, Minichiello L, Zlokovic BV, Peti-Peterdi J. Neuron-like function of the nephron central command. bioRxiv. 2021:2021.2012.2006.471478.
62. Gyarmati G, Toma I, Izuhara A, Burford JL, Shroff UN, Papadouri S, Deepak S, Peti-Peterdi J. The role of TRPC6 calcium channels and P2 purinergic receptors in podocyte mechanical and metabolic sensing. Physiol Int. 2021.
63. Shroff UN, Gyarmati G, Izuhara A, Deepak S, Peti-Peterdi J. A new view of macula densa cell protein synthesis. Am J Physiol Renal Physiol. 2021;321(6):F689-f704.
64. Gyarmati G, Shroff UN, Izuhara A, Hou X, Da Sacco S, Sedrakyan S, Lemley KV, Amann K, Perin L, Peti-Peterdi J. Intravital imaging reveals glomerular capillary distension and endothelial and immune cell activation early in Alport syndrome. JCI Insight. 2022;7(1).
65. Cowley AW, Jr., Yang C, Kumar V, Lazar J, Jacob H, Geurts AM, Liu P, Dayton A, Kurth T, Liang M. Pappa2 is linked to salt-sensitive hypertension in Dahl S rats. Physiol Genomics. 2016;48(1):62-72.
66. Lindstrom NO, De Sena Brandine G, Tran T, Ransick A, Suh G, Guo J, Kim AD, Parvez RK, Ruffins SW, Rutledge EA, Thornton ME, Grubbs B, McMahon JA, Smith AD, McMahon AP. Progressive Recruitment of Mesenchymal Progenitors Reveals a Time-Dependent Process of Cell Fate Acquisition in Mouse and Human Nephrogenesis. Dev Cell. 45. United States: 2018 Elsevier Inc; 2018. p. 651-660 e654.
67. Jain A, Tuteja G. TissueEnrich: Tissue-specific gene enrichment analysis. Bioinformatics. 2019;35(11):1966-1967.

68. Kim JI, Ganesan S, Luo SX, Wu YW, Park E, Huang EJ, Chen L, Ding JB. Aldehyde dehydrogenase 1a1 mediates a GABA synthesis pathway in midbrain dopaminergic neurons. Science. 2015;350(6256):102-106.

69. Dragunow M, Faull R. The use of c-fos as a metabolic marker in neuronal pathway tracing. J Neurosci Methods. 1989;29(3):261-265.

70. Gyarmati G, Shroff UN, Riquier-Brison A, Desposito D, Ju W, Izuhara A, Deepak S, Burford JL, Kadoya H, Chen Y, Rinschen MM, Ahmadi N, Lau L, Gill IS, Kretzler M, Peti-Peterdi J. Physiological activation of the nephron central command drives endogenous kidney tissue regeneration. bioRxiv. 2021:2021.2012.2007.471692.

71. Schiessl IM, Fremter K, Burford JL, Castrop H, Peti-Peterdi J. Long-Term Cell Fate Tracking of Individual Renal Cells Using Serial Intravital Microscopy. Methods Mol Biol. 2020;2150:25-44.

72. Kim KH, Chen CC, Alpini G, Lau LF. CCN1 induces hepatic ductular reaction through integrin αvβ5-mediated activation of NF-κB. J Clin Invest. 2015;125(5):1886-1900.

73. McMahon EJ, Bauer JD, Hawley CM, Isbel NM, Stowasser M, Johnson DW, Campbell KL. A randomized trial of dietary sodium restriction in CKD. J Am Soc Nephrol. 2013;24(12):2096-2103.

74. Ruggenenti P, Cravedi P, Remuzzi G. Mechanisms and treatment of CKD. J Am Soc Nephrol. 2012;23(12):1917-1928.

75. Clevers H. Wnt/beta-catenin signaling in development and disease. Cell. 2006;127(3):469-480.

76. Kim KH, Won JH, Cheng N, Lau LF. The matricellular protein CCN1 in tissue injury repair. J Cell Commun Signal. 2018;12(1):273-279.

77. Kaverina NV, Eng DG, Largent AD, Daehn I, Chang A, Gross KW, Pippin JW, Hohenstein P, Shankland SJ. WT1 Is Necessary for the Proliferation and Migration of Cells of Renin Lineage Following Kidney Podocyte Depletion. Stem Cell Reports. 2017;9(4):1152-1166.

78. Kreidberg JA. WT1 and kidney progenitor cells. Organogenesis. 2010;6(2):61-70.

79. Asahara T, Murohara T, Sullivan A, Silver M, van der Zee R, Li T, Witzenbichler B, Schatteman G, Isner JM. Isolation of putative progenitor endothelial cells for angiogenesis. Science. 1997;275(5302):964-967.

80. Ronconi E, Sagrinati C, Angelotti ML, Lazzeri E, Mazzinghi B, Ballerini L, Parente E, Becherucci F, Gacci M, Carini M, Maggi E, Serio M, Vannelli GB, Lasagni L, Romagnani S, Romagnani P. Regeneration of glomerular podocytes by human renal progenitors. J Am Soc Nephrol. 2009;20(2):322-332.

81. Bariety J, Mandet C, Hill GS, Bruneval P. Parietal podocytes in normal human glomeruli. J Am Soc Nephrol. 2006;17(10):2770-2780.

82. Berger K, Schulte K, Boor P, Kuppe C, van Kuppevelt TH, Floege J, Smeets B, Moeller MJ. The regenerative potential of parietal epithelial cells in adult mice. J Am Soc Nephrol. 2014;25(4):693-705.

83. Rizzo P, Perico N, Gagliardini E, Novelli R, Alison MR, Remuzzi G, Benigni A. Nature and mediators of parietal epithelial cell activation in glomerulonephritides of human and rat. Am J Pathol. 2013;183(6):1769-1778.

84. Yang Y, Gomez JA, Herrera M, Perez-Marco R, Repenning P, Zhang Z, Payne A, Pratt RE, Koller B, Beierwaltes WH, Coffman T, Mirotsou M, Dzau VJ. Salt restriction leads to activation of adult renal mesenchymal stromal cell-like cells via prostaglandin E2 and E-prostanoid receptor 4. Hypertension. 2015;65(5):1047-1054.

85. Quilley J, Santos M, Pedraza P. Renal protective effect of chronic inhibition of COX-2 with SC-58236 in streptozotocin-diabetic rats. Am J Physiol Heart Circ Physiol. 2011;300(6):H2316-2322.

86. Cheng HF, Wang CJ, Moeckel GW, Zhang MZ, McKanna JA, Harris RC. Cyclooxygenase-2 inhibitor blocks expression of mediators of renal injury in a model of diabetes and hypertension. Kidney Int. 2002;62(3):929-939.

87. Marsh DJ, Postnov DD, Sosnovtseva OV, Holstein-Rathlou NH. The nephron-arterial network and its interactions. Am J Physiol Renal Physiol. 2019;316(5):F769-f784.

88. Zhou X, Li J, Yang W. Calcium/calmodulin-dependent protein kinase II regulates cyclooxygenase-2 expression and prostaglandin E2 production by activating cAMP-response element-binding protein in rat peritoneal macrophages. Immunology. 2014;143(2):287-299.

89. Abu-Soud HM, Yoho LL, Stuehr DJ. Calmodulin controls neuronal nitric-oxide synthase by a dual mechanism. Activation of intra- and interdomain electron transfer. J Biol Chem. 1994;269(51):32047-32050.

90. Lapointe JY, Bell PD, Cardinal J. Direct evidence for apical Na+:2Cl-:K+ cotransport in macula densa cells. Am J Physiol. 1990;258(5 Pt 2):F1466-1469.

91. He B, Chen P, Zambrano S, Dabaghie D, Hu Y, Möller-Hackbarth K, Unnersjö-Jess D, Korkut GG, Charrin E, Jeansson M, Bintanel-Morcillo M, Witasp A, Wennberg L, Wernerson A, Schermer B, Benzing T, Ernfors P, Betsholtz C, Lal M, Sandberg R, Patrakka J. Single-cell RNA sequencing reveals the mesangial identity and species diversity of glomerular cell transcriptomes. Nat Commun. 2021;12(1):2141.

92. Ransick A, Lindström NO, Liu J, Zhu Q, Guo JJ, Alvarado GF, Kim AD, Black HG, Kim J, McMahon AP. Single-Cell Profiling Reveals Sex, Lineage, and Regional Diversity in the Mouse Kidney. Dev Cell. 2019;51(3):399-413.e397.

93. Wu H, Gonzalez Villalobos R, Yao X, Reilly D, Chen T, Rankin M, Myshkin E, Breyer MD, Humphreys BD. Mapping the single-cell transcriptomic response of murine diabetic kidney disease to therapies. Cell Metab. 2022;34(7):1064-1078.e1066.

94. Crosley EJ, Dunk CE, Beristain AG, Christians JK. IGFBP-4 and -5 are expressed in first-trimester villi and differentially regulate the migration of HTR-8/SVneo cells. Reprod Biol Endocrinol. 2014;12:123.

95. Masuda K, Tanabe K, Ujike H, Hinamoto N, Miyake H, Tanimura S, Sugiyama H, Sato Y, Maeshima Y, Wada J. Deletion of pro-angiogenic factor vasohibin-2 ameliorates glomerular alterations in a mouse diabetic nephropathy model. PLoS One. 2018;13(4):e0195779.

96. Simmons DA, Knowles JK, Belichenko NP, Banerjee G, Finkle C, Massa SM, Longo FM. A small molecule p75NTR ligand, LM11A-31, reverses cholinergic neurite dystrophy in Alzheimer's disease mouse models with mid- to late-stage disease progression. PLoS One. 2014;9(8):e102136.

97. Gomez RA, Sequeira-Lopez MLS. Renin cells in homeostasis, regeneration and immune defence mechanisms. Nat Rev Nephrol. 2018;14(4):231-245.

98. Harris SS, Wolf F, De Strooper B, Busche MA. Tipping the Scales: Peptide-Dependent Dysregulation of Neural Circuit Dynamics in Alzheimer's Disease. Neuron. 2020;107(3):417-435.

99. De Strooper B, Karran E. The Cellular Phase of Alzheimer's Disease. Cell. 2016;164(4):603-615.

100. Holstein-Rathlou NH, Leyssac PP. TGF-mediated oscillations in the proximal intratubular pressure: differences between spontaneously hypertensive rats and Wistar-Kyoto rats. Acta Physiol Scand. 1986;126(3):333-339.
101. Yip KP, Holstein-Rathlou NH, Marsh DJ. Chaos in blood flow control in genetic and renovascular hypertensive rats. Am J Physiol. 1991;261(3 Pt 2):F400-408.
102. Kisler K, Nelson AR, Montagne A, Zlokovic BV. Cerebral blood flow regulation and neurovascular dysfunction in Alzheimer disease. Nat Rev Neurosci. 2017;18(7):419-434.
103. Sexton C, Snyder H, Beher D, Boxer AL, Brannelly P, Brion JP, Buée L, Cacace AM, Chételat G, Citron M, DeVos SL, Diaz K, Feldman HH, Frost B, Goate AM, Gold M, Hyman B, Johnson K, Karch CM, Kerwin DR, Koroshetz WJ, Litvan I, Morris HR, Mummery CJ, Mutamba J, Patterson MC, Quiroz YT, Rabinovici GD, Rommel A, Shulman MB, Toledo-Sherman LM, Weninger S, Wildsmith KR, Worley SL, Carrillo MC. Current directions in tau research: Highlights from Tau 2020. Alzheimers Dement. 2021.
104. Lorenzi T, Graciotti L, Sagrati A, Reguzzoni M, Protasoni M, Minardi D, Milanese G, Cremona O, Fabri M, Morroni M. Normal human macula densa morphology and cell turnover: A histological, ultrastructural, and immunohistochemical investigation. Anat Rec (Hoboken). 2020;303(11):2904-2916.

9. BIBLIOGRAPHY OF THE CANDIDATE'S PUBLICATIONS

Peer reviewed publications relevant to the dissertation

1. **Gyarmati G**, Shroff UN, Riquier-Brison A, Kriz W, Kaissling B, Neal CR, Arkill KP, Ahmadi N, Gill IS, Moon JY, Desposito D, Peti-Peterdi J. A new view of macula densa cell microanatomy. Am J Physiol Renal Physiol. 2021 Mar 1;320(3):F492-F504. doi: 10.1152/ajprenal.00546.2020. Epub 2021 Jan 25. PMID: 33491562; PMCID: PMC7988809.

2. **Gyarmati G**, Toma I, Izuhara A, Burford JL, Shroff UN, Papadouri S, Deepak S, Peti-Peterdi J. The role of TRPC6 calcium channels and P2 purinergic receptors in podocyte mechanical and metabolic sensing. Physiol Int. 2021 Dec 16:2021.00205. doi: 10.1556/2060.2021.00205. Epub ahead of print. PMID: 34978536; PMCID: PMC9200898.

3. **Gyarmati G**, Shroff UN, Izuhara A, Hou X, Da Sacco S, Sedrakyan S, Lemley KV, Amann K, Perin L, Peti-Peterdi J. Intravital imaging reveals glomerular capillary distension and endothelial and immune cell activation early in Alport syndrome. JCI Insight. 2022 Jan 11;7(1):e152676. doi: 10.1172/jci.insight.152676. PMID: 34793332; PMCID: PMC8765042.

4. Shroff UN, **Gyarmati G**, Izuhara A, Deepak S, Peti-Peterdi J. A new view of macula densa cell protein synthesis. Am J Physiol Renal Physiol. 2021;321(6):F689-f704.

5. Desposito D, Schiessl IM, **Gyarmati G**, Riquier-Brison A, Izuhara AK, Kadoya H, Der B, Shroff UN, Hong YK, Peti-Peterdi J. Serial intravital imaging captures dynamic and functional endothelial remodeling with single-cell resolution. JCI Insight. 2021 May 24;6(10):e123392. doi: 10.1172/jci.insight.123392. PMID: 33848265; PMCID: PMC8262275.

Other peer reviewed publications

1. Stocker SD, Kinsman BJ, Farquhar WB, **Gyarmati G**, Peti-Peterdi J, Sved AF. Physiological Mechanisms of Dietary Salt Sensing in the Brain, Kidney, and Gastrointestinal Tract. Hypertension. 2023 Sep 6. doi: 10.1161/HYPERTENSIONAHA.123.19488. Epub ahead of print. PMID: 37671571.

2. Riquier-Brison ADM, Sipos A, Prókai Á, Vargas SL, Toma L, Meer EJ, Villanueva KG, Chen JCM, **Gyarmati G**, Yih C, Tang E, Nadim B, Pendekanti S, Garrelds IM, Nguyen G, Danser AHJ, Peti-Peterdi J. The macula densa prorenin receptor is essential in renin release and blood pressure control. Am J Physiol Renal Physiol. 2018 Sep 1;315(3):F521-F534. doi: 10.1152/ajprenal.00029.2018. Epub 2018 Apr 18. PMID: 29667908; PMCID: PMC6172576.

3. **Gyarmati G**, Kadoya H, Moon JY, Burford JL, Ahmadi N, Gill IS, Hong YK, Dér B, Peti-Peterdi J. Advances in Renal Cell Imaging. Semin Nephrol. 2018 Jan;38(1):52-62. doi: 10.1016/j.semnephrol.2017.09.004. PMID: 29291762; PMCID: PMC5773263.

4. **Gyarmati G**, Jacob CO, Peti-Peterdi J. New Endothelial Mechanisms in Glomerular (Patho)biology and Proteinuria Development Captured by Intravital Multiphoton Imaging. Front Med (Lausanne). 2021 Oct 13;8:765356. doi: 10.3389/fmed.2021.765356. PMID: 34722598; PMCID: PMC8548465.

5. Shroff UN, Schiessl IM, **Gyarmati G**, Riquier-Brison A, Peti-Peterdi J. Novel fluorescence techniques to quantitate renal cell biology. Methods Cell Biol. 2019;154:85-107. doi: 10.1016/bs.mcb.2019.04.013. Epub 2019 May 17. PMID: 31493823; PMCID: PMC6748388.

6. Kadoya H, Yu N, Schiessl IM, Riquier-Brison A, **Gyarmati G**, Desposito D, Kidokoro K, Butler MJ, Jacob CO, Peti-Peterdi J. Essential role and therapeutic

targeting of the glomerular endothelial glycocalyx in lupus nephritis. JCI Insight. 2020 Oct 2;5(19):e131252. doi: 10.1172/jci.insight.131252. PMID: 32870819; PMCID: PMC7566710.

7. Hu C, Lakshmipathi J, Stuart D, Peti-Peterdi J, **Gyarmati G**, Hao CM, Hansell P, Kohan DE. Renomedullary Interstitial Cell Endothelin A Receptors Regulate BP and Renal Function. J Am Soc Nephrol. 2020 Jul;31(7):1555-1568. doi: 10.1681/ASN.2020020232. Epub 2020 Jun 2. PMID: 32487560; PMCID: PMC7351004.

8. Burford JL, **Gyarmati G**, Shirato I, Kriz W, Lemley KV, Peti-Peterdi J. Combined use of electron microscopy and intravital imaging captures morphological and functional features of podocyte detachment. Pflugers Arch. 2017 Aug;469(7-8):965-974. doi: 10.1007/s00424-017-2020-0. Epub 2017 Jun 29. PMID: 28664407; PMCID: PMC5553195.

9. Choi D, Park E, Jung E, Seong YJ, Hong M, Lee S, Burford J, **Gyarmati G**, Peti-Peterdi J, Srikanth S, Gwack Y, Koh CJ, Boriushkin E, Hamik A, Wong AK, Hong YK. ORAI1 Activates Proliferation of Lymphatic Endothelial Cells in Response to Laminar Flow Through Krüppel-Like Factors 2 and 4. Circ Res. 2017 Apr 28;120(9):1426-1439. doi: 10.1161/CIRCRESAHA.116.309548. Epub 2017 Feb 6. PMID: 28167653; PMCID: PMC6300148.

10. **Gyarmati G**, Turner MC, Castaño-Vinyals G, Espinosa A, Papantoniou K, Alguacil J, Costas L, Pérez-Gómez B, Martin Sanchez V, Ardanaz E, Moreno V, Gómez-Acebo I, Fernández-Tardon G, Villanueva Ballester V, Capelo R, Chirlaque MD, Santibáñez M, Pollán M, Aragonés N, Kogevinas M. Night shift work and stomach cancer risk in the MCC-Spain study. Occup Environ Med. 2016 Aug;73(8):520-7. doi: 10.1136/oemed-2016-103597. Epub 2016 Jun 16. PMID: 27312400.

11. **Gyarmati G**, Simor T, Kádár K, Tóth L, Németh T, Oprea V, Hartyánszky I. Mágneses rezonancia vizsgálat a jobb es bal kamra funkciójának megítélésére nagyér-transzpozíciós gyermekek Senning-mutétje után [Quantification of right and left ventricular function with magnetic resonance imaging after Senning operation for complete transposition of the great arteries]. Orv Hetil. 2006 Jan 29;147(4):171-4. Hungarian. PMID: 16515025.

Other publications

1. **Gyarmati G**, Shroff UN, Riquier-Brison A, Stocker SD, Izuhara A, Deepak S, Chen Y, Biemesderfer D, James AW, Minichiello L, Zlokovic BV, Peti-Peterdi J. Neuron-like function of the nephron central command. bioRxiv. 2021:2021.12.06.471478.
2. **Gyarmati G**, Shroff UN, Riquier-Brison A, Desposito D, Ju W, Izuhara A, Deepak S, Burford JL, Kadoya H, Ch Rinschen M, Ahmadi N, Lau L, Gill IS, Kretzler M, Peti-Peterdi J. Physiological activation of the nephron central command drives endogenous kidney tissue regeneration. bioRxiv. 2021:2021.12.07.471692.

10. ACKNOWLEDGEMENTS

"If I have seen further, it is by standing on the shoulders of giants." – Isaac Newton

First and foremost, I would like to extend my sincere thanks to my Ph.D. Mentors Professor Laszlo Rosivall and Professor János Peti-Peterdi for their guidance, help, and support throughout my journey. Drs. Rosivall and Peti-Peterdi has been an immense source of scientific, academic, and emotional support and encouragement throughout the last several years. Importantly, I would like to emphasize the major impact and immense value of the pioneering scientific work of Professor Laszlo Harsing, Professor Laszlo Rosivall and Professor Janos Peti-Peterdi and their prescient contribution to the understanding of the role and physiological importance of the macula densa. Their work guided my research, and their commitment to developing hypotheses-driven scientific projects inspired me profoundly. I will take their teachings with me as I embark on the next stage of my professional and personal life, for which I will be always grateful.

I would like to extend my gratitude and acknowledge all my colleagues for their constructive feedback and scientific input that shaped my hypothesis and research. Specifically, I wish to thank Anne Riquier-Brison, Urvi Nikhil Shroff, Audrey Izuhara, and Yibu Chen, who were instrumental in shaping my hypotheses, research strategies, and analysis skills. I am very thankful for their support, friendship, and conversations, both scientific and otherwise.

Last but not least, I would like to thank my family, my husband and our children, my parents, and my friends for their support, for always helping me reach my goals, and always encouraging me to pursue my dreams, professional or personal. Thank you for always being on my side, for lifting me up and making me strong, for motivating me, for tolerating my crazy diets, for always making me smile, for loving me. "Being deeply loved by someone gives you strength, while loving someone deeply gives you courage." – Lao Tzu